Wang, P., Prell, W.L., Blum, P., et al., 2000
Proceedings of the Ocean Drilling Program, Initial Reports Volume 184

1. Leg 184 Summary: Exploring the Asian Monsoon through Drilling in the South China Sea[1]

Shipboard Scientific Party[2]

ABSTRACT

The Asian monsoon system is a major component of both regional and global climate. Evolution of monsoonal climates in southern Asia is linked to the growth of the Himalayan-Tibetan orogen, the opening and closing of marginal seas, and changes in global climate. The location of the South China Sea (SCS) between East Asia and the "maritime continent" is ideal to document the paleoceanographic responses to both winter and summer monsoons. The broad scientific themes of Leg 184 were (1) to document the Cenozoic history of the SCS, including its biostratigraphy, lithostratigraphy, chronology, paleoclimatology, and paleoceanography; (2) to reconstruct the evolution and variability of the East Asian monsoon during the late Cenozoic on millennial, orbital, and tectonic time scales; and (3) to identify and better understand the links between tectonic uplift, erosion and weathering, hemipelagic deposition, and climate change, including the co-evolution of the Asian monsoon and Neogene global cooling. The Leg 184 shipboard party cored 17 holes at Sites 1143–1148 in the SCS and exceeded leg objectives by recovering 5463 m of sediment that will enable the study of these themes. Core recovery averaged 83%–101%; all sites (except 1148) were triple cored with the advanced hydraulic piston corer and partially double or triple cored with the extended core barrel to construct continuous stratigraphic sections at the meters composite depth (mcd) scale. At all sites the hemipelagic deposits are rich in calcareous microfossils, enabling the application of stable isotopes and faunal analyses in addressing Leg 184 scientific goals. Similarly, all sites display excellent orbital-scale cyclicity in color reflectance, natural gamma, and

[1]Examples of how to reference the whole or part of this volume.
[2]Shipboard Scientific Party addresses.

Ms 184IR-101

magnetic susceptibility. The suite of sites yields an almost continuous record of the environmental history of the South China Sea during the last 32 m.y.

Site 1143 is located in the Nansha or Spratly Islands area of the southern SCS at a water depth of 2772 m. A 516-m-long composite section was constructed from three holes, recording the depositional history of the last ~10 m.y., with linear sedimentation rates (LSRs) of 30–70 m/m.y. and mass accumulation rates (MARs) of 3–10 g/cm^2/k.y. Sites 1144 through 1148 are located on the northeast continental slope of the SCS. Site 1144 provided a 522-m-long composite section from a sediment drift at a water depth of 2037 m, spanning the last 1 m.y. and yielding very high LSRs (300–1100 m/m.y.) and MARs (25–140 g/cm^2/k.y.). At Site 1145, a 213-m-long composite section representing the last 3 m.y. was recovered from a water depth of 3175 m, with LSRs of 40–250 m/m.y. and MARs of 4–19 g/cm^2/k.y. Site 1146, at a water depth of 2092 m, recovered a 645-m-long composite section representing a 19-m.y. record and yielding LSRs of 20–360 m/m.y. and MARs of 2–23 g/cm^2/k.y. Site 1147 is a short record (85 mcd) retrieved only 0.4 nmi from Site 1148 and designed to recover the top several meters of sediment missing at Site 1148. Site 1148 recovered a 861-m-long composite section from a water depth of 3294 m, spanning the last 32 m.y. The LSRs are 10–20 m/m.y. for the Miocene to mid-Pliocene, up to 200 m/m.y. for the late Pliocene and Pleistocene, and up to 300 m/m.y. for the Oligocene. The high accumulation rates (5–20 g/cm^2/k.y.) of Oligocene sediments on the lower continental slope near the continent crust margin probably reflect active downslope transport of terrigenous sediments during the early stage of seafloor spreading of the South China Sea basin. The seismic profiles indicate that a deep-water sequence continues below the bottom of the hole and might be a thick marine Paleogene section.

The depositional history of the late Cenozoic in the northern slope had three important stages: an Oligocene interval with extremely high sedimentation rates, a Miocene and early Pliocene interval with lower sedimentation rates and high carbonate content, and an interval of the last 3 m.y. with high clastic sediment accumulation rates. A different trend of depositional history is indicated at the southern Site 1143, where carbonate accumulation decreased from the late Miocene toward the late Pleistocene and the noncarbonate accumulation has increased over the last 3 m.y. However, the upper Miocene sediments were similar in composition between the northern and southern sites, containing more than 50% carbonate. The Oligocene/Miocene boundary in the northern SCS (Site 1148) is marked by sedimentary deformation, abrupt lithologic changes, and a stratigraphic hiatus (~24–27 Ma). These related features will help resolve the nature and timing of one of the most significant Cenozoic tectonic and climatic changes of the region. A general increase of noncarbonate sediment accumulation after 2–3 Ma was found at all drill sites, and for the northern sites the increase becomes even more significant in the latter part of the last million years.

INTRODUCTION

The Shipboard Scientific Party of Leg 184 sought to better understand the history and variability of the Asian monsoon system, which is a major component of regional and global climate. Evolution of monsoonal climates in southern Asia is linked to the growth of the Hima-

layan-Tibetan orogen, the opening and closing of marginal seas, and changes in global climate, including atmospheric CO_2 levels. The South China Sea (SCS) experiences both summer and winter monsoons, and its sediments record the erosion and weathering of tectonic orogens as well as changes in global and regional climate. Hence, Leg 184 was designed to recover sediment sections in the southern and northern SCS to provide records capable of unraveling both the regional and global climate changes on a variety of time scales ranging from centennial to tectonic.

The circulation patterns of the Asian summer and winter monsoons dominate the seasonal patterns of winds, precipitation, and runoff and determine, in part, the character of land vegetation over southern and eastern Asia (Hastenrath, 1991; Hastenrath and Greischar, 1993; Webster, 1987, 1994; Webster et al., 1998; Ding, 1998; Lau and Yang, 1997). The winter monsoon is characterized by continental cooling and development of high pressure over northern Asia, northeast winds across the South China Sea (which intensify during cold surges), and increased rainfall in the Austral-Asian equatorial zone (Fig. **F1A, F1C**). Similarly, northeast winds are found in the Indian Ocean, although they are weaker and not accompanied by cold surges. The summer monsoon circulation is characterized by continental heating, the development of low pressure over Tibet, and southerly winds across all of southern Asia. In the South China Sea, the summer monsoon is marked by moderate (5 m/s) southerly winds, weak to moderate upwelling off Vietnam, and high precipitation over southern and eastern Asia (Fig. **F1B, F1D**). In contrast, the summer monsoon of the Arabian Sea exhibits strong (10 m/s) southwesterly winds and intense upwelling. The location of the South China Sea between East Asia and the equatorial "maritime continent" is ideal to record the paleoceanographic responses to both winter and summer monsoons (Figs. **F1, F2**).

F1. Climatology of the summer and winter monsoon circulation, **p. 45.**

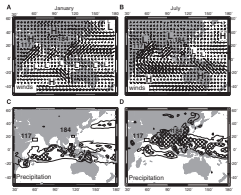

F2. Locations of Leg 184 drilling areas in the South China Sea, **p. 46.**

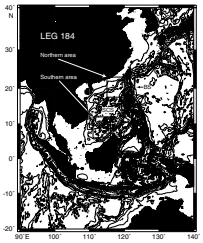

TECTONIC FRAMEWORK OF THE SOUTH CHINA SEA

Among the continents of the world, Asia has been subjected to the most significant Cenozoic deformation. The Cretaceous–Paleocene topography of China was generally tilted to the west, with the coastal areas of the Tethys in the west, a trans-Himalayan volcanic arc in the southwest, and relatively high land and endoreic basins in the east. These conditions lasted until the late Eocene when India collided with Asia, thereby bringing the maritime climate in western China to an end. Although some argue for a Cretaceous plateau with as much as 3 km elevation (Murphy et al., 1997; Harrison et al., 1998), other studies indicate that uplift of the Tibetan Plateau began ~21–20 Ma (Copeland et al., 1987; Harrison et al., 1992, 1998) and was accompanied by a general subsidence of eastern China. Molnar and others (1993) argue for a late Miocene (10–8 Ma) rapid uplift of the Tibetan Plateau from a low or intermediate level to its maximum elevation (>5 km) and subsidence to its current elevation (~4 km). Still other geologists and geomorphologists believe that the Tibetan Plateau was uplifted only 2–3 m.y. ago (e.g., Li, 1991). In any case, these surface uplift changes reversed the topographic gradient in China from west tilting to east tilting. Subsequent tectonics have maintained or increased the west-east gradient.

Coincident with the large-scale deformation of Asia, many of the marginal seas in the western Pacific were formed during the early Miocene (Tamaki and Honza, 1991). One model links the opening of the SCS basin with the Red River fault zone, which has at least 500 to 600 km of left-lateral displacement created during the Oligocene and Miocene (Schärer et al., 1990; Briais et al., 1993). Alternative models relate the opening of the SCS to subduction under Borneo (Holloway, 1982; Taylor and Hayes, 1980, 1983) and the influence of subduction beneath the Philippines, driving a backarc type of extension in the over-riding plate (Taylor and Hayes, 1980). The deep-water, rhomboid-shaped Central Basin is underlain by oceanic crust (Fig. F3A), which contains a sequence of seafloor-spreading magnetic anomalies ranging from 32 (magnetic Anomaly 11) to 16 Ma (Anomaly 5c), with a southward ridge jump at ~27 Ma (Anomaly 7/6b) (Briais et al., 1993). The present shape of the SCS is closely related to the rotation history of the Philippine Sea Plate to the east and the ongoing collision with the Australian Plate to the south (Packham, 1996). The counterclockwise rotation of the Philippine Sea Plate led to the arc-continent collision of the Luzon Arc with the underthrusting Eurasian Plate since 6.5 Ma (Huang et al., 1997), giving rise to the formation of Taiwan Island and the Bashi Strait. Both the collision processes have further isolated the SCS.

The slopes of the South China Sea contain numerous coral reef terrains, including the Nansha Terrain (Reed Bank and Dangerous Grounds) and the Xisha-Zhongsha Terrain (Macclesfield Bank and Paracel Island), which may have rifted southward during the opening of the SCS (Jin, 1992). The structure of the northern SCS margin has been extensively studied through oil exploration and geophysical studies to determine the amount of crustal extension during formation of the SCS (e.g., Nissen et al., 1995). The shelf basins on the SCS contain >4 km of Cenozoic deposits that have been drilled by petroleum companies (Ru et al., 1994).

F3. Tectonic setting of the South China Sea, p. 47.

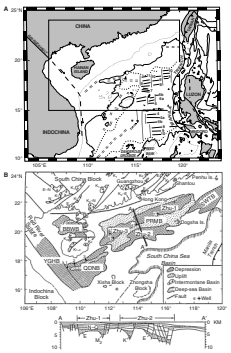

EVOLUTION OF ASIAN MONSOONAL CLIMATES

Evolution and variability of the Asian monsoon system are thought to reflect at least five types of large-scale climate forcing or boundary condition changes, including (1) the tectonic development of the Himalayan-Tibetan orography, (2) changes in the atmospheric CO_2 concentration, (3) changes in the Earth's orbit that result in periodic variations of seasonal solar radiation, (4) changes in the extent of glacial climates, and (5) internal feedbacks within the climate system. These factors act simultaneously and over different time scales to amplify or lessen the seasonal development of continental heating/cooling, land-sea pressure gradients, latent heat transport, and moisture convergence, all of which control the strength of the monsoon circulation.

The impact of elevated orography on atmospheric circulation provides an explanation for the initiation, intensification, and long-term (10^6 yr) evolution of the Asian monsoon system (Ruddiman, 1997). Before the collision of India with Asia at ~55–50 Ma, the Himalayas and Tibetan Plateau were not the dominant orographic features of Asia, and the continent was not as large. The smaller size and lower elevations of precollision Asia and the larger area of epicontinental seas would have resulted in lower land-sea heating contrasts, especially because of the reduced role of sensible heating over the plateau and the condensa-

tional heating over and on the flanks of the Himalayan-Tibetan Plateau Complex (HTC). Model studies suggest that the plateau must be at least half its present elevation to induce a strong monsoon circulation (Prell and Kutzbach, 1992). During the summer monsoon, the major orographic impact is thermal and results from the tendency of higher elevation to increase both sensible and latent heating of the midtroposphere, leading to stronger monsoon circulation. During the winter monsoon, the mechanical effects of high orography, such as blocking and directing low-level winds and the development of cold surges, are the major orographic impacts of the HTC. The thermal impacts are thought to be relatively small (Murakami, 1987). The location of the South China Sea, with active winter and summer monsoons, provides an ideal site to study the seasonal monsoon system, especially the evolution of the winter monsoon and its relationship to the development of the loess plateau in central China (Ding et al., 1998).

The coincidence of high relief, southerly and easterly sloping topography, and abundant monsoon rainfall has resulted in large river systems, which discharge enormous amounts of sediment onto the coastal plains and the continental shelves and slopes of the Southeast Asian marginal seas. Prior Deep Sea Drilling Project (DSDP) and Ocean Drilling Program (ODP) sites on the Ganges and Indus Fans have found clastic deep-sea fan sedimentation in the lower Miocene and Oligocene, which gives a minimum age for Himalayan-type erosion and transport. Although these fan sediments may be related to monsoon runoff (Cochran, 1990), they do not reflect the onset of clastic deposition from the Asian continent, which is likely to have begun with the earliest collisional arcs. In the upper Miocene, both marine and terrestrial data indicate a major intensification of the Indian monsoon around 8 Ma (Prell et al., 1992, and references within; Molnar et al., 1993; Prell and Kutzbach, 1992). However, the significance of clastic accumulation rates at this time is unclear, and various explanations invoke changes in tectonic, climatic, and sea-level conditions (Rea, 1992; Derry and France-Lanord, 1997; Prell and Kutzbach, 1997). The SCS sediments provide additional combinations of these processes and should help constrain the monsoon-related responses to tectonic forcing.

A variety of observations has suggested that CO_2 levels were higher during the Tertiary and may have been equivalent to double the present CO_2 levels at ~20 Ma (see Kump and Arthur, 1997, and other papers in Ruddiman, 1997). Higher CO_2 levels might be expected to strengthen the summer monsoon through increased land-sea contrasts and more active hydrologic budgets but might also weaken the winter monsoon through warmer continents. The Neogene decrease in CO_2 has also been linked to uplift of the Tibetan Plateau and late Cenozoic global cooling (e.g., Ruddiman and Kutzbach, 1989; Raymo et al., 1988) through long-term increased chemical erosion in rapidly uplifted areas that reduce atmospheric CO_2 (Raymo, 1994) and thereby cool the planet, enabling widespread glaciation. Other studies have linked the decreased CO_2 to uplift, erosion, and carbon burial in clastic deep-sea fans (Derry and France-Lanord, 1997). In either case, evolution of the Asian monsoon and global cooling may well be related. Lower atmospheric CO_2 is also proposed as the cause of global-scale changes from C_3- to C_4-type vegetation at ~7 Ma (Cerling, 1997) (see Fig. **F4**). This vegetation shift also has implications for monsoonal processes related to soil moisture, albedo, and carbon cycling (Cerling, 1997). Hence, the

F4. Marine and terrestrial observations and a model simulation, **p. 48.**

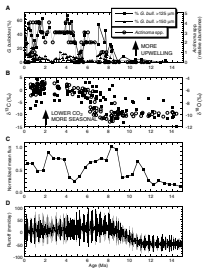

late Neogene trend toward lower CO_2 may covary with stronger winter monsoons and weaker summer monsoon hydrologic cycles.

Superposed on the tectonic and CO_2 trends are orbitally induced, periodic variations in the seasonal and meridional distribution of solar energy over the Earth's surface. The variations associated with obliquity and precessional cycles can change the seasonal radiation budget over the Tibetan Plateau by as much as +12.5% (relative to modern values of 450 W/m²) (Laskar et al., 1993; Berger and Loutre, 1991). Numerous studies of Indian Ocean and western Pacific sediments have documented that certain monsoon indicators (upwelling fauna, productivity, dust particle size, and vegetation types) vary coherently with these orbital periodicities, especially the 23 k.y. (Prell, 1984a, 1984b; Clemens and Prell, 1990, 1991a, 1991b; Clemens et al., 1991, 1996; Morley and Heusser, 1997; Schultz et al., 1998). However, the variation of monsoonal indices is not always in direct proportion or in phase with the apparent solar forcing. These phase differences indicate that other processes within the climate system are influencing the timing and amplitude of maximum monsoon responses. We expected that the phase of monsoonal responses in the SCS, especially Sites 1143,1144, and 1146, would provide high-quality records of orbital-scale variations and new constraints on the relative importance of orbital forcing and internal feedbacks to East Asian monsoonal variability.

The monsoon system is also affected by the general state of the Earth's climate, especially the extent of glacial-age surface boundary conditions, which include lowered sea levels, continental-scale terrestrial ice sheets and large areas of sea ice, lowered sea-surface temperatures, lowered CO_2, and differing vegetation and land-surface characteristics (CLIMAP, 1981; Prell and Kutzbach, 1987, 1992). In general, more extensive glacial conditions tend to weaken the summer monsoon circulation (Clemens et al., 1996), although certain glacial intervals do have strong monsoons (Clemens and Prell, 1991a, 1991b). In the SCS, studies indicate that increased upwelling during the last glacial maximum (LGM) may reflect a stronger winter monsoon circulation. Also, the emergence of the "maritime continent" during intervals of lower sea level may affect the regional dynamics of the East Asian monsoon.

A synthesis of Cenozoic terrestrial data from China (e.g., Liu and Ding, 1993; Wang, 1990) has led to the development of a four-stage model of East Asian monsoon evolution: (1) a premonsoon stage (Paleocene and early Eocene), (2) a transitional stage (middle Eocene to Oligocene), (3) a monsoon Stage I (Miocene and Pliocene), and (4) a monsoon Stage II (late Pliocene [2.4 Ma] to present) (Fig. **F5**; Wang, 1997).

The Paleocene (premonsoon stage) is characterized by a broad east-west–trending arid zone traversing all of China (Fig. **F5**). This is similar to the Late Cretaceous environmental pattern, when evaporitic endoreic basins accumulated thousands of meters of halite- and gypsum-bearing deposits in the middle and lower reaches of the Changjiang (Yangtze) River, a region that is humid today. The subsequent middle–late Eocene and Oligocene transitional stage was characterized by variable, weak summer monsoons that brought moisture to the otherwise dry areas, which created favorable conditions for nonmarine oil accumulation in China. Beginning in the Neogene, however, palynologic, paleobotanic, and lithologic data indicate that the climate pattern in China underwent a profound reorganization (Wang, 1990; X. Sun and

F5. Summary of monsoonal stages, **p. 49.**

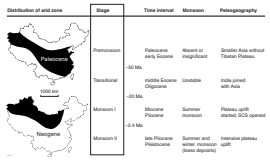

P. Wang, pers. comm., 1998). During the Miocene monsoon Stage I, the arid zone retreated to northwest China, and eastern China became more humid (Fig. F5) as the southeast summer monsoon strengthened and brought moisture from the sea. This general regime has existed from the Miocene to the Holocene. The intensification of the winter monsoon in eastern Asia is thought to have occurred much later and to be coincident with the beginning of deposition of the Chinese loess at ~2.4 Ma (monsoon Stage II; e.g., An et al., 1990). However, some recent studies suggest that the eolian component of the loess red-clay sequence may be as old as 7 Ma (e.g., Ding et al., 1998), which would have implications for the tectonic vs. glacial initiation and intensification of the winter monsoon.

A primary goal of Leg 184 was to understand the relative importance of these complex "causal" factors in the initiation, evolution, and variability of the Asian monsoon system. In short, we sought to decipher the coevolution of tectonic uplift of the HTC, the Neogene changes in global climate, and the development and variability of the Asian monsoon circulation.

SEDIMENTS OF THE SOUTH CHINA SEA

The sedimentary basins of the northern shelf show a two-layer structure, with the lower section characterized by half-grabens formed during Paleogene rifting and filled with nonmarine sequences. The upper section is typified by a wide range of terrigenous and marine sediments deposited during the Neogene subsidence of the margin (Fig. F6) (Ru et al., 1994). However, reworked Paleocene and Eocene marine microfossils in the Neogene deposits from the northern shelf indicate that marine intervals existed earlier in this area. Paleocene deltaic and Eocene marine sediments have also been found in the southern part of the SCS, such as the Liyue Bank (Reed Bank) Basin, where carbonate deposition began in the mid-Oligocene (ASCOPE, 1981; Jin, 1989). In the northern SCS, the Pearl River Mouth Basin (PRMB) has been extensively studied and is close to our core sites. More than 150 wells have been drilled on the shelf, and a detailed stratigraphy has been established for the marine sequence from the uppermost Oligocene to Pleistocene on the basis of planktonic microfossils (e.g., Huang, 1997). The composite stratigraphy of the PRMB documents a marine sequence from the upper Oligocene (NP23/24) to Holocene (NN20) (Jiang et al., 1994; Wu, 1994; Huang, 1997). In the PRMB, a number of seismic reflectors have been correlated with sequence boundaries and their associated depositional hiatuses. Unfortunately, the wells and seismic sections used to define the sequence boundaries and reflectors are in the northern part of the PRMB, which has mostly nonmarine sediments. The nonmarine intercalations decrease in volume and thin southward toward the slope, where our sites are located. Hence, the type sections for reflector identification are not well correlated with our sites. In addition, the reflector terminology differs between various industrial and academic groups (Wang, 1996; L. Huang, pers. comm., 1998; Ludmann and Wong, 1999). We have adopted the sequence/reflector scheme of Ludmann and Wong (table 1), which enumerates seven reflectors from the lower Oligocene to the Pleistocene (see **"Seismic Systems and Data,"** p. 2, in the "Seismic Stratigraphy" chapter, for discussion of the reflectors). Note that this reflector sequence and terminology is similar but not

F6. Composite stratigraphy from industrial wells, **p. 50.**

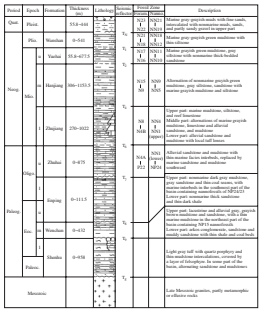

identical to the sequence of Jiang et al., 1994, which is illustrated in Figure F6.

The modern sediments in the SCS consist mainly of terrigenous material, biogenic carbonate and opal, and a small portion of volcanic material. Clastic sediments are discharged mainly from the Mekong, Red, and Pearl Rivers. However, during the past glacial intervals, the paleo–Sunda River system may have contributed large amounts of sediment to the SCS. Recent sediment trap studies in the northern SCS (Jennerjahn et al., 1992; Wiesner et al., 1996) have shown that the highest particle fluxes occurred during the winter monsoon and are correlated with high wind speed rather than riverine-transported sediments. These data indicate that suspended matter from Taiwan and outside the Bashi Strait might be major sediment sources for the northern SCS. The combination of high terrigenous input and the depth (3500 m) of the modern carbonate compensation depth (CCD) blankets the extensive continental slopes of the SCS with hemipelagic sediments, whereas the deep-sea basin is covered by abyssal clay (Su and Wang, 1994). Biogenic carbonates are found around coral reef islands, especially in the southern areas. The accumulation of carbonates in the SCS exhibits two patterns during the late Quaternary. The "Atlantic" pattern, found above the lysocline, has high carbonate during interglacials and low carbonate in glacial phases and is primarily driven by terrigenous dilution. The "Pacific" pattern, found below the lysocline, has low carbonate during interglacials and high carbonate during glacials and is driven by carbonate dissolution on the seafloor (Bian et al., 1992; Thunell et al., 1992; Zheng et al., 1993; Miao et al., 1994; Wang et al., 1995).

PALEOCEANOGRAPHY OF THE SOUTH CHINA SEA

Despite the importance and interconnections of the East Asian and Indian monsoons, few marine-based studies have compared the past monsoonal variations of the two subsystems. Previous ODP studies have focused on the Arabian Sea monsoon (Leg 117: Prell, Niitsuma, et al., 1991; Prell et al., 1992, and references within) and on the Sulu Sea (Leg 124: Rangin, Silver, von Breymann, et al., 1990) to the south of the South China Sea. Many of the East Asian and South China Sea paleomonsoon studies have used traditional and long piston cores to focus on the late Quaternary climate changes. During the last glacial maximum, a lower sea level greatly altered the configuration and area of the western Pacific marginal seas. The three major shelf areas that emerged during the LGM (East China Sea Shelf, Sunda Shelf [the Great Asian Bank], and Sahul Shelf [the Great Australian Bank]) exposed 3,900,000 km² ("maritime continent"), which is comparable in size to the Indian subcontinent. The SCS lost half of its surface area (>52%) as a result of shelf exposure, which changed its configuration into a semi-isolated basin (Wang et al., 1997). Moreover, the most extensive shelf area of the SCS is located in the modern Western Pacific Warm Pool bounded by the 28°C surface isotherm. The reduction in size must have profoundly influenced the thermodynamic role played by the Global Warm Pool.

The central portion of the SCS experienced a considerable decline in the sea-surface temperature (SST) during the LGM. Large decreases in the winter SST in the western Pacific marginal seas and especially in the SCS (Wang and Wang, 1990; Miao et al., 1994; Wang et al., 1995; Chen

and Huang, 1998; Chen et al., 1999; Pflaumann and Jian, 1999) are interpreted to indicate that the winter monsoon strengthened, the polar front shifted southward, and the Kuroshio Current migrated eastward. Together with the negligible changes in the summer SST, the South China Sea experienced a much higher seasonality SST during the LGM (Wang et al., 1999). An important consequence of the glacial conditions in the SCS region is the intensified aridity in China. The summer monsoon is the main source of water vapor for rainfall in East China (Chen et al., 1991), and changes in shelf emergence, SST decline, and land-sea heating patterns must have led to a reduction of vapor transport to southern Asia. A rough calculation suggests that the reduction in evaporation from the SCS during the LGM could correspond to one-eighth to one-fourth of the annual precipitation in all of China (Wang et al., 1997). The glacial reduction in water vapor transport helps to explain the intensification of aridity in the China hinterland as evidenced by the extensive distribution of loess deposits. Moreover, the glacial increase of seasonality in the marginal seas may help resolve the tropical paleoclimate enigma in the Pacific; that is, the discrepancy between marine and terrestrial indicators of paleotemperature during the LGM (Stuijts et al., 1988; Anderson and Webb, 1994).

Studies of the late Quaternary have demonstrated the great potential of the SCS's hemipelagic sediments to provide high-resolution paleoenvironment records. A core from the northern SCS (SONNE95-17940, 20°07′N, 117°23′E, 1727 m) reveals a highly detailed transition from glacial to Holocene conditions (Fig. **F7**; Wang et al., 1999). The LGM and isotope Stage 3 are characterized by low fluvial clay content (50%–60%) and high modal grain size (10–25 µm), whereas the Holocene is marked by high clay content (>70%) and low modal grain size (<6.3 µm). These data are interpreted to indicate a strong winter monsoon and weak summer monsoon precipitation during the glacial regime and a strong summer monsoon and weakened winter monsoon during the Holocene regime. However, with lowered sea level during glacials, a large subareal sediment source is exposed on the shelf of the East China Sea. Deflation and transport of these sediments to the South China Sea during glacials is another possible explanation for the coarser particle sizes. The $\delta^{18}O$ data from the mixed-layer planktonic foraminifer *Globigerinoides ruber* reveal numerous short-term light $\delta^{18}O$ events superimposed on the main pattern of glacial–postglacial change (Fig. **F7**). These events appear to reflect increases in summer monsoon intensity (i.e., reduced sea-surface salinity together with increased input of fluvial clay and decreased modal grain size). The increases in summer monsoon intensity can be correlated with Dansgaard-Oeschger Events 1–10 in the GISP2 ice core (Fig. **F7**). Also observed in this SCS core are four periods of relatively heavy $\delta^{18}O$ associated with low fluvial clay content and larger grain size (i.e., reduced summer monsoon rainfall and increased winter monsoon wind, which correlate with the Heinrich Events 1–4 (Fig. **F7**). The early Holocene/Preboreal summer monsoon maximum revealed by a broad $\delta^{18}O$ minimum and fluvial clay maximum has also been reported from the Arabian Sea (Prell, 1984b; Sirocko et al., 1993). The 8.2-ka cooling event recorded in the GISP2 ice core appears to coincide with a large increase in $\delta^{18}O$ and, hence, a decrease in summer monsoon precipitation in the SCS. Similar rapid events in the Bay of Bengal and Andaman Sea have been related to North Atlantic climate change (Colin et al., 1998). The Leg 184 cores, along with the recent cores from the joint German-Chinese Monitor Monsoon expedition (Sarnthein et al., 1994; Sarnthein and Wang, 1999), and the 1997

F7. East Asian monsoon climate change in the northern SCS, **p. 51.**

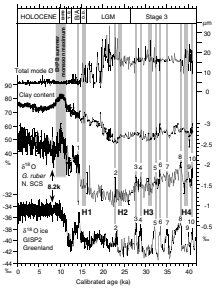

IMAGES III cruise for the first time provide systematic and high-quality material for studying the long-term evolution and variability of the monsoonal South China Sea.

SCIENTIFIC OBJECTIVES

The broad scientific themes of Leg 184 were threefold:

1. To document the Cenozoic history of the South China Sea, including its biostratigraphy, lithostratigraphy, chronology, paleoclimatology, and paleoceanography;
2. To reconstruct the evolution and variability of the East Asian monsoon during the late Cenozoic on millennial, orbital, and tectonic time scales; and
3. To identify and better understand the links between tectonic uplift, erosion and weathering, hemipelagic deposition, and climate change, including the evolution of the Asian monsoon and Neogene global cooling.

To address these broad themes, Leg 184 had a number of shipboard and shore-based scientific objectives, as discussed in the following sections.

Evolution and Variability of the Asian Summer Monsoon

The summer monsoon is responsible for most of southern Asia's annual rainfall; its evolution and variability have a great impact on the region's climate, vegetation, erosion, weathering, and transport of sediments. In the South China Sea, potential proxies of the summer monsoon include isotopic and faunal indicators of lower salinity and freshwater from monsoon rains and runoff, tropical pollen carried by southerly winds, variation of clay minerals and rare-earth elements indicating provenance, the presence of upwelling/mixing faunas due to southerly winds and upwelling along Vietnam, variations of accumulation rates, and physical properties. Pollen analysis of core SONNE95-17940 suggests that an increase in herbaceous pollen and charcoal can indicate aridity and hence weakened summer monsoons; the appearance of alpine conifer pollen may be used as a proxy of the winter monsoon (Sun, 1996; Sun and Li, 1999). Although these properties are not exclusively monsoon in origin, we expect to find both long-term trends and orbital-scale (as well as millennial scale in some cases) variability in an inter-related array of these monsoon proxies.

Coevolution of South China Sea Seasonality and the Asian Winter Monsoon

Because the winter monsoon reflects cooling over northern Asia (a function of both precession and obliquity), it may exhibit a more complex response than the summer monsoon. Potential proxies of the winter monsoon include lower winter season SSTs, increased subtropical and subpolar index species, increased accumulation of loess, and enhanced transport from the East China Sea and the Pacific. Comparison of upper Neogene sections from the northern and southern part of the SCS will enable us to construct a history of the thermal gradient within

the SCS. These paleotemperature data should provide information on when the winter monsoon began to develop large seasonality, especially in the northern SCS, and on the stability and variability of temperatures in the southern SCS, which lies within the Western Pacific Warm Pool. Although seasonality reflects a number of processes, intensification of monsoon circulation is one mechanism that could increase the seasonality of the region. The onset of glacial conditions would also increase seasonality within the SCS but would likely be related to a strengthening of the East Asian winter monsoon.

Links between Himalayan-Tibetan Uplift, Erosion, Weathering, and Climate Change

A major theme of Leg 184 was to evaluate potential relationships between the Tibetan Plateau uplift, monsoon evolution, and global cooling. A number of hypotheses have been proposed to explain various tectonic-climate relationships. These hypotheses come from a diverse set of disciplines including structural geology, micropaleontology, geophysics, geochemistry, stratigraphy of both terrestrial and marine sections, and climate modeling.

The Leg 184 drilling and logging program was designed to obtain long-term, high-resolution records of monsoonal proxies to establish the history of monsoon evolution in the SCS so that it could be compared to other marine and terrestrial records of tectonic and climatic change. Specifically, we sought to develop records of monsoon intensity, denudation/accumulation rates, and climate cooling in the SCS. However, the relationships between tectonics, erosion, and climate are complex and highly nonlinear (see papers in Ruddiman, 1997). The tectonic control of the Asian monsoons, for example, is by no means limited to the plateau uplift. Only recently has the influence of the evolution of surrounding marine basins on monsoon evolution been discussed, with only the role of the Paratethys considered (Ramstein et al., 1997). The western Pacific marginal seas, however, should have more direct impact on the evolution of the East Asian monsoon. The SCS cores should provide a new set of constraints on the pattern and timing of weathering/erosion and sediment transport related to tectonic uplift and climate.

Orbital-Scale Precessional Forcing of the Summer Monsoon

Much of the previously identified monsoonal variability in tropical oceans is precessional (23 k.y.) in scale. Shipboard construction of initial splices and age models indicate strong primary orbital periodicity in the SCS sediments. By inference, strong precessional responses are likely related to monsoonal processes. One critical objective is to use this orbital-scale variability to establish the amplitude, coherency, and phase relationships of the East Asian monsoon with orbital and glacial forcing as well as internal feedbacks of the climate system (Clemens, 1999). Initial shipboard results should resolve whether the SCS monsoonal variations are consistent with orbital models of monsoonal variability. Postcruise research will be needed to expand and refine the sedimentary time series and perform more rigorous tests.

Neogene Stationarity of the Monsoon

Stationarity is a fundamental property of a time series and defines the temporal stability of a variable's characteristics. A nonstationary property changes its mean value, amplitude (or variance), and phase over some length of time. Clemens et al. (1996) have shown that the Indian Southwest Monsoon is nonstationary over the past 3.6 m.y. Specifically, monsoon proxies change their phase relative to ice volume ($\delta^{18}O$) and dust content. Although the temporal changes are not large, they completely change the phase relationships at the precessional scale. The time series evolution of the SCS Neogene sections will provide a different monsoonal regime to test the stationarity of the monsoon response.

Millennial-Scale Variability of Monsoonal Climate

One objective of Leg 184 was to recover high-accumulation-rate sediments that would allow paleoceanographic analyses on millennial, centennial, and even decadal time scales. This objective is feasible in the northern SCS. For example, a piston core near Site 1144 (SONNE95-17940) contains a Holocene section nearly 7 m thick, which equates to a temporal resolution of 15 yr/cm. The remaining core has rates equivalent to ~40–50 yr/cm (Sarnthein et al., 1994; Wang et al., 1999). However, the *Sonne* core reaches only 40 ka. Our objective is to analyze the sediments of Site 1144 to extend this high-resolution record over the past 1 m.y.

Evolution of Tropical and Subtropical Faunas

The paleoclimatic and paleoceanographic history of the SCS is paralleled by changes in the planktonic faunas and floras. Some changes are global ocean events whereas others, especially the population characteristics of groups, reflect the evolving oceanography of the SCS. Previous studies have found remarkable changes in relative abundances of planktonic foraminifer *Pulleniatina obliquiloculata* in the Pleistocene, in the size and abundance of nannoplankton reticulafenestrids in the Miocene/Pliocene, and in species of mangrove pollen *Florschuetzia* in the Miocene—all of which are tied to environmental events. Leg 184 data will enable us to systematically compare the biological and physical processes.

Links between Terrestrial and Marine Stratigraphy

Extensive petroleum exploration and academic studies have produced much information on the Cenozoic paleoenvironmental history of mainland and offshore China (Zhou, 1984; Li et al., 1984; Ye et al., 1993). Because of the language barrier and commercial restrictions, however, few of these data have been available to the global scientific community. In addition, poor stratigraphic control of the mostly nonmarine deposits has made it difficult to correlate the sediment records with the global paleoenvironmental history. Leg 184 shipboard stratigraphy will provide the first direct calibration of open-marine stratigraphy to the local and regional land-based stratigraphies, thereby linking them with the record of global environmental changes. These correlations will provide a different perspective on the identification of the timing of changes in denudation/accumulation rates, the leads or lags

between terrestrial and marine records, tectonic events, and monsoon intensification. A correlation between the loess/paleosol sequence and the deep-sea sediments in the SCS will be most relevant to this purpose.

Eolian Transport to the South China Sea

A number of studies have suggested that the South China Sea accumulates eolian silts and clays (loess) during glacial climate phases (e.g., Wang et al., 1999). Leg 184 scientists seek to identify both the long-term evolution and orbital-scale variability of eolian sedimentation in the SCS, especially at the northern sites. This objective is difficult to address because of the terrigenous nature of the hemipelagic sediments that blanket the northern continental slope. We expect that combinations of the geochemical, mineralogical, and grain-size characteristics will help identify the eolian component of these sediments. Numerous volcanic ash layers should also provide additional indicators of paleowind directions when their sources are identified by postcruise analysis.

Histories of Indian and East Asian Summer Monsoons

Another goal of Leg 184 is to compare the evolution of the East Asian monsoon in the SCS with the evolution of the Indian monsoon in the Arabian Sea to identify common sources of causality. Given the development of reliable chronology and monsoonal indices, the SCS records will be correlated with the ODP Arabian Sea sites, which primarily record the summer monsoon. We predict that the SCS and Arabian Sea summer monsoon responses will be similar in long-term trends and in their phase relative to ice volume. The winter monsoon response is expected to be stronger in the SCS.

Paleoceanographic Proxies of the East Asian Summer and Winter Monsoons

Leg 184 scientists plan to continue to develop reliable proxies of monsoonal response in the SCS, as recorded in sediment properties, rates of sediment accumulation, chemical content, and species distribution of flora and fauna. On the basis of previous studies, we expect that numerous sediment properties along with faunal changes will exhibit variability related to monsoonal forcing (Figs. **F4, F7**). Shipboard measurements included core logging of magnetic susceptibility (MS), bulk density, color reflectance (CR), and natural gamma radiation (NGR). Postcruise work will measure and refine the time series of chemical, isotopic, and faunal variability to place additional constraints on the relationship between sediment proxies and monsoonal intensity.

Paleoceanographic Impacts of South China Sea Basin Evolution

The opening of the SCS basin together with crustal subsidence must have given rise to transgressive sequences during the late Oligocene and early Miocene. The formation of islands on the eastern and southern borders of the SCS resulted from collision with the Australian and Philippine Sea plates, reducing the water exchange between the SCS and the Pacific and Indian Oceans. The appearance of the modern Bashi Strait (sill depth ~2600 m) between Luzon and Taiwan resulted from the

Luzon Arc collision begun ~6.5 m.y. ago. Before then, a free connection existed between the South China Sea and the western Pacific, as indicated by similarities in deep-water faunas and CCD. The evolution of the shape and borders of the SCS should also have changed the source areas of terrigenous material; hence, tectonic models can be partly tested by provenance analyses of sediments from different stages of basin evolution.

Paleoclimate Significance of the South China Sea As a Marginal Basin

The formation of marginal seas in the western Pacific and their response to the glacial cycles must have played a crucial role in the global climate system. Because the connection between these marginal seas and the open Pacific is usually through narrow and/or shallow seaways, these seas are highly sensitive to any tectonic deformation or eustatic fluctuations. The SCS, the largest of the marginal seas, is a critical pathway for heat and vapor exchanges between Asia and the ocean; its geological evolution should have significant climatic impacts. The formation of its southern border was closely related to the Australia-Asia collision that caused the closure of the Indonesian Seaway and the enhancement of the Kuroshio Current ~10–12 Ma (Kennett, 1985). The rotation of the Philippine Sea plate created Luzon Island, which splits the west-flowing Equatorial Warm Current into the Kuroshio and Midanao Warm Currents essential to the supply of Western Pacific Warm Pool waters. The progressive closure of the SCS has increased its amplifying effect on glacial signals and the north-south contrast in climate (Wang, 1999).

DRILLING STRATEGY

The coring strategy for Leg 184 reflected both the scientific priorities for prospective sites and a number of operational, practical, and strategic factors. Initially, Leg 184 was planned to core six sites: one on the southern margin and five on the northern margin. Despite a delayed departure from Fremantle, Australia, and a diversion to Singapore to repair the ship's 10-cm radar, we cored 17 holes at six sites (Sites 1143–1148) (Table T1; Figs. F8, F9). SCS-3, the lowest priority proposed site, was sacrificed in favor of deepening Sites 1143, 1146, and 1148. At all sites, our drilling strategy was to triple core with the advanced hydraulic piston corer (APC) system to refusal and deepen at least one hole with the extended core barrel (XCB) system to the maximum approved depth. Site 1148 was the single site where only two holes were drilled. All sites deeper than 400 meters below seafloor (mbsf) (Sites 1143, 1144, 1146, and 1148) were wireline logged as planned.

Our drilling plan was to first core the southern Site 1143 enroute to the northern operations area. Following a brief seismic survey of proposed sites SCS-4, -5C, -5D, and -5E, as required for final safety approval, we elected to core SCS-1 (Site 1144), which had prior Pollution Prevention and Safety Panel (PPSP) approval. During the occupation of Site 1144, we received approval to core the surveyed sites with minor changes in locations. Our final site selection on the northern continental margin was aimed to maximize recovery of different stratigraphic sections at different water depths. Site 1144 (proposed site SCS-1) at a water depth of 2037 m focused on the Pleistocene section, and Sites

T1. Leg 184 operational summary, p. 76.

F8. Site location map for the southern South China Sea Site 1143, p. 52.

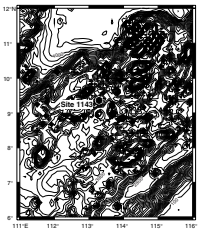

F9. Site location map for the northern South China Sea Sites 1144–1148, p. 53.

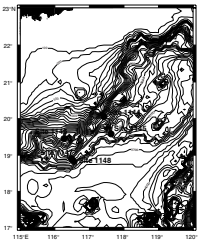

1146 (SCS-4) and 1148 (SCS-5C) centered on the Oligocene to Pliocene section at water depths of 2092 and 3294 m, respectively.

SCIENTIFIC MEASUREMENTS STRATEGY

Because the central theme of Leg 184 was the Neogene coevolution of tectonics and climate, the shipboard focus was on recovering continuous sediment sections capable of recording millennial- to orbital-scale variations. This focus is reflected in the Leg 184 shipboard measurements program as well as its sampling plan and shore-based analysis.

The shipboard measurement strategy was to acquire high-resolution (2–5 cm) core-logging records from all holes, including MS, gamma-ray attenuation (GRA) bulk density, NGR, and CR. These data were used to construct the meters composite depth (mcd) scale, which was used to evaluate the completeness of the stratigraphic section and to splice a complete, representative record for each site. Routine measurements, taken at frequencies of one per section to one per core (intervals of ~1.5–10 m), included biostratigraphy (calcareous nannofossils and foraminifers), paleomagnetism, hydrocarbon gas analysis, interstitial water chemistry, moisture and density, carbonate, X-ray diffraction, and *P*-wave velocities.

The Leg 184 downhole logging plan was designed to provide (1) complete stratigraphic coverage, especially in the incomplete XCB intervals; (2) proxy data not available from core measurements, such as resistivity and yields of K, U, and Th; and (3) in situ sonic velocity for the construction of synthetic seismograms. Sites 1143, 1144, 1146, and 1148 were logged using the following three downhole tool strings:

1. The triple combination tool string, which includes the dual induction tool to measure resistivity, the accelerator porosity sonde to measure porosity, and the hostile environment lithodensity sonde to measure bulk density and general lithology. Also included on this tool string were the hostile environment natural gamma-ray sonde (HNGS) to measure total NGR and to calculate K, U, and Th yields and the Lamont-Doherty Earth Observatory temperature logging tool to measure borehole fluid temperature.
2. The FMS-sonic tool string, which includes the Formation MicroScanner (FMS) with the general-purpose inclinometry tool to measure microresistivity at centimeter resolution and the dipole sonic imager to measure compressional and shear-wave velocity.
3. The geological high-resolution magnetic tool (GHMT), which includes the nuclear magnetic remanence sonde to measure the total magnetic field and the susceptibility measurement sonde to measure the MS from induction.

SITE SUMMARIES

Site 1143

Site 1143 (proposed site SCS-9) is located 9°21.72′N, 113°17.11′E, at a water depth of 2772 m (Table T1), within a basin on the southern continental margin of the South China Sea (Figs. F8, F10). On the Admiralty charts, the site lies within the Nansha or Dangerous Grounds area,

F10. Precruise seismic line across Site 1143, p. 54.

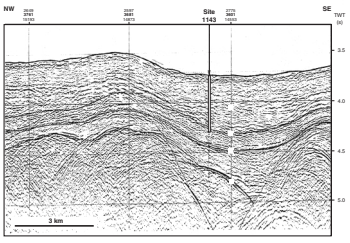

which is riddled with reefs, shoals, and small islands, some of which are within 20 to 30 miles of the site. Site 1143 was located in the southern SCS in order to provide a Neogene paleoceanographic record within the Western Pacific Warm Pool. The sediment record of high and relatively stable sea-surface temperature will allow the reconstruction of SST gradients (with the northern sites) across the SCS and should reflect the development of climatic seasonality in this region. Climate records from Site 1143 will provide the basic data to identify and interpret the evolution of summer and winter monsoon circulation in the South China Sea. Also, the southern location of Site 1143 was chosen to capture the long-term records of sediment accumulation rates and lithologic variability associated with the Mekong and Sunda River systems that might be related to uplift and denudation of Tibetan and East Asian tectonic systems.

We cored three APC/XCB holes at Site 1143. Hole 1143A reached 400 mbsf with 95% recovery, and Hole 1143B reached 258 mbsf with 95% recovery. Hole 1143C (following PPSP approval to deepen the hole) reached 500 mbsf with 96% recovery and a basal age of ~9.9 Ma (Table **T1**). We requested approval to deepen Hole 1143C beyond the originally approved 400 m penetration to extend the paleoenvironmental record in time, after the sediment age turned out to be younger than expected. We had confirmed that no significant hydrocarbon concentrations occurred in the entire interval recovered in Hole 1143A. Wireline logging was accomplished in Hole 1143A with the triple combo tool suite (86–400 mbsf) and the FMS-sonic tool combination (158–380 mbsf). Hole conditions did not allow deployment of the GHMT string.

The sediments at Site 1143 represent continuous hemipelagic sedimentation of fine-grained terrigenous material and pelagic carbonate from the late Miocene (~10 Ma) to present (Fig. **F11**). The three holes at Site 1143 were combined into a composite (spliced) stratigraphic section that is continuous in mcd scale from 0 to 190.85 mcd, the interval of APC coring. Incomplete core recovery and decreased core quality precluded splice construction below this interval, but intervals of the cored section can be correlated over the 190–400 mcd interval. Overall, most of the Pliocene/Pleistocene interval has a continuous and reliable spliced record. In general, the long-term decrease in sedimentation rates observed at Site 1143 from the upper Miocene to the Pleistocene is caused by declining accumulation rates of both carbonate and noncarbonate components. A temperature gradient of ~86°C/km was determined from five advanced hydraulic piston corer temperature tool (APCT) downhole measurements.

F11. Summary diagram of coring results at Site 1143, **p. 55.**

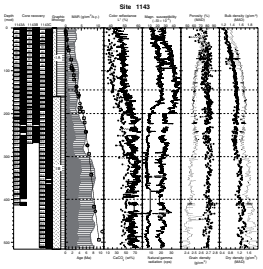

The Pleistocene-age sediments at Site 1143 consist mostly of olive, greenish, and light gray-green and greenish gray clayey nannofossil mixed sediment, clay with nannofossils, and clay. In general, bedding is not evident, and compositional changes are gradual throughout the site. Minor lithologies vary with depth and include ash layers, turbidites, and green clay layers. Carbonate content of this interval is variable but averages ~18 wt%, with both calcareous nannofossils and planktonic foraminifers abundant and well preserved. Benthic foraminifers are generally rare throughout the site. Changes in color define lithologic subunits, and these changes are mainly controlled by carbonate content. The CR measurements (lightness parameter L*) vary with the carbonate data and increase downcore. Core-logging data, especially CR, MS, and NGR, show an increasing trend downcore within the Pleistocene with superposed patterns of orbital-scale cyclicity, many of which can be correlated with glacial–interglacial cycles and marine oxy-

gen isotope stages. Magnetic susceptibility data show a number of significant spikes that correspond to observed volcanic ash layers and are particularly abundant in the intervals 20–30 and 70–100 mcd. The interstitial waters are characterized by sulfate reduction downhole to ~200 mbsf. Organic carbon content decreases from ~0.9 wt% at core top to 0.2 wt% at the base of the Pleistocene section and remains low throughout the core. Methane concentration in the sediment is <10 ppmv over the entire interval to 500 mbsf. The extended interval of sulfate reduction appears consistent with the low organic carbon and methane content in the sediments. The Brunhes/Matuyama polarity reversal was observed at ~42.5–43.8 mcd, and the Pleistocene/Pliocene boundary is located between 93.5 and 94.3 mcd. Over the Pleistocene interval, the linear sedimentation rate (LSR) averages 50 m/m.y., and the total and carbonate mass accumulation rates (MAR) (g/cm^2/k.y.) are 3.6 and 0.6, respectively.

The Pliocene-age sediments at Site 1143 are characterized by steadily increasing carbonate content, ranging from 20 to 40 wt% and averaging 28 wt% (Fig. **F11**). Calcareous nannofossils and planktonic foraminifers are abundant and generally well preserved. This interval exhibits a continued increase in the L* value and grain density, reflecting the increase in carbonate. The MS and NGR values reach a plateau in the mid-Pliocene and rapidly decrease in the lowermost Pliocene. Magnetic susceptibility spikes related to volcanic ashes occur between 120 and 190 mcd. Cyclicity of most properties continues as in the Pleistocene section but with reduced amplitude. Near the base of the Pliocene (~200 mbsf), increases in the concentrations of dissolved silica, strontium, and lithium as well as alkalinity are consistent with a lithology change observed at that depth. Change from APC to XCB coring in the lower Pliocene significantly affected the core-logging data, particularly the NGR and MS signals. Their values decreased by half across the APC/XCB coring transition, although this also partly reflects the change in lithology at that depth. NGR data from wireline logging confirm the change in lithology. The Pliocene/Miocene boundary is located between 213 and 200 mcd. Over the Pliocene interval, the average LSR is 36 m/m.y., and the total and carbonate MAR (g/cm^2/k.y.) are 3.7 and 1.0, respectively.

The Miocene-age sediments at Site 1143 are distinguished by high carbonate content (averaging 47 wt%) (Fig. **F11**), which is the primary criterion for identifying lithologic Units I and II. The green clay layers are less frequent, and turbidite layers are more frequent in the Miocene sediments. Sediments of this interval also exhibit higher CR and bulk density but lower MS and NGR. These variations probably reflect changes in clay content or abundance of foraminifer turbidite layers. Calcareous nannofossils are abundant, but their preservation deteriorates through the Miocene, whereas planktonic foraminifers are abundant and have good preservation. Over the upper Miocene interval, the average LSR is 114 m/m.y., and the total and carbonate MAR (g/cm^2/k.y.) are 14.0 and 6.6, respectively. These higher sedimentation rates are caused by frequent turbidites that were observed in the cores and clearly distinguishable both in logging data and FMS images. The sand-rich base of the turbidites is characterized by lower gamma-ray, density, and resistivity and higher porosity and *P*-wave velocity values. The opposite is true for the top clay-rich sediments.

Overall, Site 1143 provides an excellent continuous record with moderate accumulation rates, especially over the past 6 m.y. The site should enable researchers to develop high-resolution orbital-scale time

series of paleoceanographic proxies and to reconstruct the record of seasonality in the South China Sea.

Site 1144

Site 1144 (proposed site SCS-1) is located 20°3.18′N, 117°25.14′E, at a water depth of 2037 m (Table T1), on a sediment drift on the northern margin of the South China Sea (Figs. F9, F12). Site 1144 was chosen to take advantage of extremely high sedimentation rates to recover a continuous sequence of hemipelagic sediments that will yield reconstructions of paleomonsoon history on millennial, centennial, or higher resolution time scales for the mid- to late Pleistocene (~1 Ma). Site 1144 data will allow comparison of SCS records with orbital-scale and higher frequency records from ice cores, marginal seas, and terrestrial deposits. Situated along the northern margin of the SCS, Site 1144 is ideally located to reconstruct the sedimentologic, isotopic, and faunal/SST changes associated with development of the winter monsoon. This site will provide the northern constraints for reconstruction of SST gradients in the South China Sea.

F12. Precruise seismic line across Site 1144, p. 57.

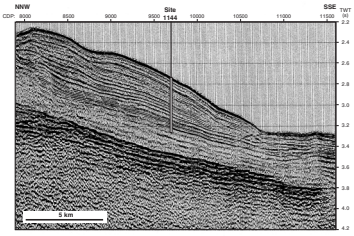

We cored three APC/XCB holes at Site 1144. Hole 1144A reached the target depth (453 mbsf) with an average recovery of 104%, Hole 1144B reached 452 mbsf with 99% recovery, and Hole 1144C was APC cored to the target depth of 204 mbsf with an average recovery of 100%. The total recovery for Site 1144 was 1113 m, representing 101% of the cored interval (Table T1). Following completion of Hole 1144A, wireline logs were successfully acquired at depths from 87 to 452 mbsf for all three tool suites (triple combo, FMS-sonic, and GHMT). The temperature gradient within the sediment column at Site 1144 is anomalously low (24°C/km), about one-third of the expected value. Reasons for this may include the rapid sedimentation rate or subsurface water circulation.

Coring at Site 1144 recovered a mid- to upper Pleistocene and Holocene sequence of rapidly accumulating, hemipelagic clays with a basal age of ~1.1 Ma (Fig. F13). The recovered sequence spans 452 mbsf (519 mcd). The continuous spliced record (mcd scale) extends from 0 to 235.41 mcd. Splice construction below this interval was precluded by incomplete core recovery and alignment of coring gaps. However, a discontinuous ("floating") mcd depth scale was constructed from 235 to 519 mcd based on correlations among cores from the three holes.

F13. Summary diagram of coring results at Site 1144, p. 58.

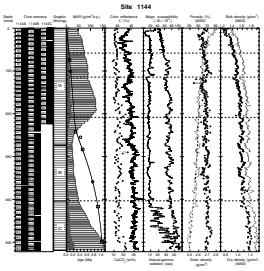

The Pleistocene-age sediments at Site 1144 are notable for their high sedimentation rates and organic carbon content, the cyclicity of their physical properties, and the variations of "iron sulfide" and pyrite. The sediments represent a rapidly accumulating drift deposit with hemipelagic sedimentation of clay with quartz silt and nannofossils, completely homogenized by bioturbation. Definitions of the lithologic subunits reflect the abundance of "iron sulfides" (which mainly occur in the uppermost interval, 0–283 mcd), siliceous biota (highest proportion in middle interval, 283–404 mcd), and pyrite (which mainly occurs in the lowermost interval, 404–518 mcd). Minor lithologies (5%–10% of the sediment) include clay with quartz silt and sponge spicules, clay with quartz silt and diatoms, clay with silt, silty clay, and clay. Ash layers and green clay layers are rare throughout, but a number of rather indistinct green clay layers and patches occur over the same intervals that contain more discrete layers at Site 1143. Downslope redeposition is suggested by thin layers of foraminifer ooze with small amounts of pyrite and a variety of macrofossils, including gastropods, scaphopods, pteropods, fragments of echinoderms, and poorly defined shell debris.

Wood debris as long as 4 cm was also observed. Bulk X-ray diffraction (XRD) analysis revealed that the mineralogy mimics the overall visual homogeneity of the sediment.

Carbonate content of this Pleistocene section is low and ranges from 10 to 20 wt%. Unlike at other sites, CR data did not correlate well with shipboard carbonate measurements taken at much lower sampling resolutions. However, the CR data do show detailed, high-resolution variations with patterns similar to recognized glacial–interglacial scale variations. Over the upper section of Site 1144 (0–100 mcd), increases in bulk density and NGR and decreases in porosity reflect rapid compaction, with superimposed fluctuations of glacial–interglacial and higher frequency compositional variation. Both core data and downhole logging show a markedly decreased rate of compaction over the next 320-m interval (100–420 mcd), and the superimposed signal variability is of larger amplitude. Magnetic susceptibility is low and rather featureless through these two upper intervals, apart from some spikes representing ash layers. However, an abrupt, threefold increase in MS takes place at ~420 mcd and is associated with a decrease in porosity from 55% to 50% as well as increased downhole sonic velocities. These changes correspond to the depth of a prominent seismic reflector. Because of the scarcity of biostratigraphic markers in this section of high sedimentation rates, we have not yet determined if a hiatus exists at that depth and/or if the section may reflect past mass wasting events in the sediment drift.

Organic carbon is relatively high at Site 1144 and decreases from ~1.5 wt% near the core top to 0.3 wt% at 519 mcd. Methane measured in headspace and void spaces ranged from 0.5% to > 60% by volume, respectively, and was biogenic in origin. No heavier hydrocarbons were observed. The interstitial waters at Site 1144 indicated sulfate reduction in the upper few meters and ammonia production throughout the remaining core. Dissolution of biogenic phases and alteration of volcanic material and clay accounted for a number of the interstitial water profiles. A few profiles indicated a change at ~420 mcd, where physical properties and seismic records also detect a boundary.

The chronostratigraphy of Site 1144 is primarily derived from the calcareous nannofossil and planktonic foraminiferal zones and events and is aided by the abundance patterns of several planktonic foraminifers, siliceous microfossils, benthic foraminifers, and pteropods. Because of the extremely high sedimentation rates at this location, only eight of the standard biostratigraphic zones and markers could be identified over the past 1.1 m.y. Unfortunately, the magnetopolarity stratigraphy was also limited by the high sedimentation rates and poor magnetization. Only the Laschamp Event (0.04 Ma) is tentatively identified at 23.5–25.5 mcd. The temporal pattern of magnetic intensity apparently correlates well with other intensity records and is consistent with the biostratigraphic age model. Sedimentation rates varied within the section but tend to decrease downhole, with the exception of the lowermost 100 m. Over the upper half of the site (0–250 mcd, 0–0.31 Ma), the linear sedimentation rates average 870 m/m.y., and the total and carbonate MARs (g/cm^2/k.y.) average 85 and 11, respectively. In the lower half of Site 1144 (250–519 mcd, 0.31–1.03 Ma), the LSR averages 370 m/m.y., and the total and carbonate MAR (g/cm^2/k.y.) average 64.0 and 9.6, respectively.

In summary, Site 1144 offers an exceptionally high sedimentation-rate section with well-defined variability of many properties for the study of climate-ocean response on the orbital, millennial, centennial,

and higher resolution time scales for the mid- to late Pleistocene (~1 Ma). The data from Site 1144 will be among the highest resolution marine records and should enable direct comparison of the South China Sea climates with records from ice cores, laminated sequences, and terrestrial deposits.

Site 1145

Site 1145 (proposed site SCS-2) is located 19°35.04′N, 117°37.86′E, at a water depth of 3175 m (Table T1), near the base of the northern continental margin of the South China Sea (Figs. F9, F14). The location of Site 1145 was selected to provide a deep-water contrast to Site 1144 (i.e., below the depth of the Bashi Strait, 2600 m) so that the water-mass depth gradients and ventilation history of the South China Sea could be reconstructed for the Quaternary. Site 1145 was also envisioned as a mid-Pliocene through Pleistocene record of the intensification of the winter monsoon.

We cored three APC/XCB holes at Site 1145. Hole 1145A reached the target depth of 200 mbsf with average recovery of 93%, Hole 1145B reached 200 mbsf with an average recovery of 90%, and Hole 1145C reached 198 mbsf with an average recovery of 96%. The total core recovered at this site was 555 m, representing 93% recovery (Table T1). Downhole and bottom-water temperature measurements revealed a thermal gradient of 90°C/km, which is consistent with the water depth of the site.

Site 1145 recovered a continuous sequence of hemipelagic clays of late Pliocene to Holocene age with a basal age of ~3.3 Ma (Fig. F15). A complete composite (spliced) section was constructed over the entire depth of 213 mcd. The site is noteworthy for its excellent paleomagnetic stratigraphy and distinct patterns of cyclicity.

The Pleistocene-age sediments at Site 1145 mainly consist of intensely bioturbated clay with distinct light carbonate-rich clay layers of ~0.5 to 4.0 m thickness. Although average carbonate content was low during the Pleistocene (averaging ~10 wt%), the light carbonate-rich layers were clearly recorded in the CR data, especially the lightness parameter (L*). Other core-logging data (GRA bulk density, NGR, and MS) are also characterized by high-amplitude cyclical fluctuations over the entire section. These cycles are best defined in the NGR data from the APC interval (above ~133 mcd), where the dominant wavelength changes at ~80 mcd from ~10–15 m in the upper interval to ~2–5 m in the lower interval. The first five major CR and NGR intervals are easily correlated with the marine oxygen isotope interglacial Stages 5, 7, 9, 11, and 13. Identification of light layers became more problematic with depth as the average sediment composition became more carbonate rich and the contrast between dark and light layers decreased. In the lower half of the Pleistocene, below ~80 mcd, the average values of GRA, MS, and NGR increase. The abrupt increase in these values is accompanied by a sudden decrease in porosity from ~70% to 55%. Porosity clearly diverges from a linear trend between 80 and 170 mcd. This porosity decrease alone cannot account for the changes observed in MS and NGR over the interval from 80 to 170 mcd, and the cause of these changes remains enigmatic. The sharp offset in GRA bulk density at ~133 mcd is caused by the change from APC to XCB coring. The XCB cores are moderately disturbed by partial remolding and incorporation of drilling slurry.

F14. Precruise seismic line across Site 1145, p. 59.

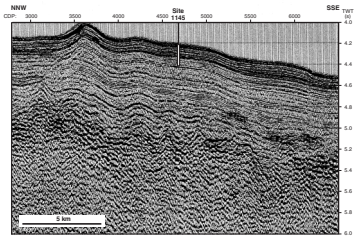

F15. Summary diagram of coring results at Site 1145, p. 60.

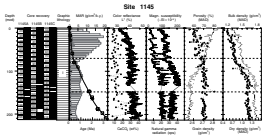

The upper part of the section (0–86 mcd) is characterized by small amounts (<10%) of biogenic silica, mainly in the form of radiolarians, diatoms, sponge spicules, and silicoflagellates. Green layers (typically 1–3 cm thick) and less distinct green mottles, as well as slightly yellowish gray patches that probably represent traces of bioturbation, appear frequently throughout the Pleistocene section. The occurrence of complete pteropod tests in the upper section (0–~70 mcd) along with abundant calcareous nannofossils and planktonic foraminifers reflects the good carbonate preservation in the upper Pleistocene. Evidence of downslope transport at Site 1145 includes several complete echinoderms, echinoderm fragments remineralized by pyrite, and several wood fragments. Although a few cores contain fresh angular volcanic glass shards within burrows and dispersed ash in low concentrations, volcanic ash represents a very minor component of the total sequence.

Total organic carbon (TOC) declined steadily from more than 1 wt% at the top of the section to much lower amounts (~0.2 wt%) at the base, consisting of mostly marine organic matter. Only trace amounts of methane (<16 ppmv) and no other hydrocarbon gases were detected in sediments at Site 1145. Interstitial water profiles are characterized by relatively constant chloride values close to those of the seawater value. In the upper part of the sedimentary column (0–~100 mcd), the sulfate, alkalinity, ammonium, and phosphate profiles show significant changes, which are caused by the diagenesis of organic matter via sulfate reduction. Sulfate reduction is incomplete, and methanogenesis is a minor process in these sediments. A large decrease in dissolved interstitial water silica occurs between ~80 and ~110 mcd (~0.5–1.0 Ma), which corresponds to a decrease in biogenic silica. This shift was also observed at ~420 mcd at Site 1144, where the shift is ~0.79 Ma.

The paleomagnetic records at Site 1145 clearly established the Brunhes/Matuyama transition at 93 mcd, the upper Jaramillo transition at 110 mcd, and the lower Jaramillo transition at ~116 mcd. Farther downcore the overprint resulting from the coring process increases, but long core measurements identify the Gauss/Matuyama boundary at 190 mcd as a jump of the inclination from ~25° to ~45° (no declination is obtained from XCB cores). Demagnetization of the discrete samples proved to be more efficient in removing the overprint, and the Olduvai Event was clearly revealed from 155 to 165 mcd. The inclinations around the Gauss/Matuyama boundary are closer to their expected values. From 190 mcd to the bottom of Hole 1145A, two samples yield unequivocal reverse inclinations. This may indicate that the upper Kaena reversal (3.04 Ma) had been reached in this hole, although this conclusion conflicts with the biostratigraphic age for the bottom of the hole and must be confirmed with shore-based analysis. Based on paleomagnetic and biostratigraphic control, the Pleistocene/Pliocene boundary can be placed at ~160 mcd. At Site 1145, the upper Pleistocene interval (0–70 mcd) had a linear sedimentation rate of 210 m/m.y. and total and carbonate MARs of 14 and 1.4 g/cm^2/k.y., respectively. The lower Pleistocene interval had lower rates, with an average LSR of 60 m/m.y. and total and carbonate MARs of 6.2 and 0.7 g/cm^2/k.y., respectively.

In the Pliocene-age section at Site 1145, average carbonate contents (17 wt%) and variability (10–30 wt%) increase (Fig. **F15**). Although planktonic foraminifers and calcareous nannofossils remain common to abundant, planktonic foraminifer preservation degraded from good to poor downsection, and the nannofossils were occasionally to commonly reworked. Benthic foraminifers are generally few. The CR and bulk data both increase in the Pliocene section and reflect the increased

carbonate content. Other properties display cyclic variability but show no longer term trends. The biostratigraphic age of the oldest sediments recovered at Site 1145 is estimated at 3.12–3.35 Ma. The Pliocene section has the lowest rates observed at Site 1145, with LSRs of 38 m/m.y. and total and carbonate MARs of 4.5 and 0.8 g/cm^2/k.y., respectively (Fig. F15).

In general, both carbonate and noncarbonate accumulations decrease downhole at Site 1145, with a small increase in the lower Pleistocene. Overall, the variations in the noncarbonate components dominate the accumulation rate pattern as at Site 1144. Site 1145 provides a high-quality section with excellent paleomagnetic stratigraphy for the resolution of orbital-scale variations of climate changes that may be compared with continental records of extensive loess deposition in China from ~2.4 Ma.

Site 1146

Site 1146 (proposed site SCS-4) is located 19°27.40′N, 116°16.37′E, at a water depth of 2092 m (Table T1), within a small rift basin on the mid-continental slope of the northern South China Sea (Figs. F9, F16). Site 1146 was intended to take advantage of the relatively shallow slope basin with moderate sedimentation rates to recover a continuous sequence of hemipelagic sediments that would yield reconstructions of East Asian monsoon history from the middle to upper Miocene (~10 Ma). Such a long-term record at orbital-scale resolution (2 k.y.) would allow comparisons of East Asian monsoon variability with orbital forcing, glacial forcing, and internal feedbacks within the climate system and provide a new set of constraints on the possible relationship between Tibetan Plateau uplift, monsoon evolution, and global cooling. Specifically, we seek to determine whether monsoonal indices intensify or weaken during the late Miocene and whether the Miocene–Pliocene pattern of accumulation rates is consistent with models of Himalayan-Tibetan uplift, monsoon intensification, and sea-level changes. Lastly, we envisioned that the Site 1146 record of the East Asian monsoon would provide an appropriate counterpart to Site 1143 in the southern SCS and Site 722 in the Arabian Sea and that their comparison could serve to identify potential sources of common causality.

We cored three APC/XCB holes at Site 1146. Hole 1146A reached the target depth of 607 mbsf with an average recovery of 100%, Hole 1146B reached 245 mbsf with an average recovery of 99%, and Hole 1146C reached 604 mbsf with an average recovery of 101% (Table T1). We requested approval to deepen Site 1146 beyond the originally approved 520 m penetration to extend the paleoenvironmental record in time, after the sediment age turned out to be younger than expected and after we had confirmed that no significant hydrocarbon concentrations occurred in the entire interval recovered. Following completion of Hole 1146A, three successful downhole logs were acquired with the triple combo (85–600 mbsf), FMS-sonic (239–600 mbsf), and GHMT (239–600 mbsf) tool strings. Downhole and bottom-water temperature measurements yielded a thermal gradient of 59°C/km at Site 1146.

Coring at Site 1146 recovered a lower Miocene through Pleistocene section of relatively carbonate-rich, hemipelagic nannofossil clays with a basal age of ~19 Ma (Fig. F17). The core-logging data enabled construction of a continuous mcd scale and a continuous spliced record from 0 to 266.7 mcd. A discontinuous ("floating") mcd scale and splice were also developed for the interval spanning 266.70–642.31 mcd,

F16. Leg 184 seismic line across Site 1146, p. 61.

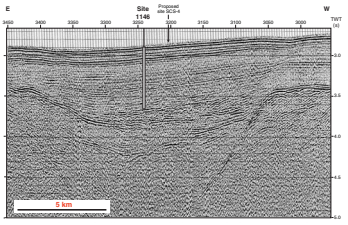

F17. Summary diagram of coring results at Site 1146, p. 62.

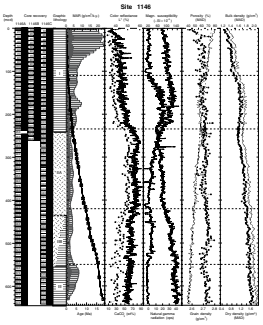

which is the bottom of the cored sequence. We expect that postcruise correlation with downhole logging data will allow construction of a complete, continuous section to 640 mcd.

The Pleistocene-age sediments are composed of greenish gray nannofossil clay that is relatively enriched with quartz, plagioclase, and chlorite relative to lower sections. This unit grades downhole into clayey nannofossil ooze within the Pliocene section. The Pleistocene sediments average ~21 wt% carbonate and are characterized by slightly lighter intervals with higher carbonate content (Fig. F17). Planktonic foraminifers are abundant and have good preservation for the site's entire interval. The upper part of the section (0–110 mcd) shows constant or slightly increasing values in CR (L* parameter), MS, and NGR, a high scatter in grain densities, and normal compaction-related increase in bulk density and *P*-wave velocity. This interval is characterized by high-amplitude variations representing orbital-scale cyclicity. Minor sediment components include large pyrite nodules that preserve organic structures (burrow-fill and Xenophyophorians) and thin, light-gray ash layers, often dispersed by bioturbation, as well as isolated pumice clasts. Diatoms, silicoflagellates, radiolarians, sponge spicules, and large (>1 cm in diameter) pteropods are common.

Total organic carbon decreases systematically from the Pleistocene sediments (1 wt% at the top of the section) to trace abundance (<0.2 wt%) below the mid-Pliocene (~225 mcd). Interstitial water profiles at Site 1146 were primarily driven by the removal and release of elements in the process of organic matter reduction, with sulfate reduction the dominant process above 68 mcd and methanogenesis dominant below. Depletion of methanogenesis products such as alkalinity, phosphate, and ammonium with depth suggests that methanogenesis is active only in the upper sediments. This agrees with the interpretation of higher methane levels and higher order hydrocarbons in headspace gas samples below 200 mcd as gases that have migrated into this site, either laterally or from depth. Dissolved silica and strontium correlate with the amount of biogenic silica and carbonate in the sediments, respectively. A major decrease in the dissolved silica concentration is observed between 109 and 140 mcd (~0.7–1.1 Ma) and accompanies a decrease in the amount of biogenic silica to near-zero values. A similar decrease was observed at Sites 1144 and 1145 at an age of ~0.8 Ma.

Paleomagnetic measurements reveal the Brunhes–Matuyama transition at 115 mcd, the upper Jaramillo transition at 133 mcd, and the lower Jaramillo transition at 138 mcd. Between 99.7 and 101.3 mcd, a swing in declination with correlative very low inclinations could document the Big Lost (geomagnetic) Event (dated at 510 to 650 ka). A transition from reverse declinations to normal occurs between 160.5 and 165.8 mcd, possibly marking the Olduvai Event. The biostratigraphy places the Pleistocene/Pliocene boundary between 185.5 and 195.1 mcd. At Site 1146, the sedimentation rates decrease downcore; the Pleistocene section has the highest rates, with an average linear sedimentation rate of 150 m/m.y. and total and carbonate MARs of 11.5 and 2.3 g/cm^2/k.y., respectively (Fig. F17).

The Pliocene-age sediments at Site 1146 (~190–310 mbsf) are distinguished by significantly higher carbonate content (an average of 47 wt% compared to 21 wt% in the Pleistocene) (Fig. F17). The transition to higher carbonate occurs in the upper Pliocene and is accompanied by an increase in the CR L* values and a decrease in the NGR and MS. This transition interval at ~235 mcd is also characterized by a very pronounced decrease in porosity and an increase in bulk density (Fig. F17).

This corresponds to a general downhole decrease in accumulation rate at that depth. The sediments grade from the overlying greenish gray nannofossil clay to homogeneous/rarely mottled, light brownish gray foraminifer and nannofossil clay mixed sediment. A small number of thin (<1–2 cm), dark ash layers, containing large volcanic glass shards as long as 1 cm, are present in the lower part of the interval. A major increase in dissolved strontium in the Pliocene/Pleistocene section between 109 and 350 mcd corresponds to the increase in the weight percent carbonate in that interval. In both cases, the availability of dissolvable biogenic sediments appears to be a strong control on dissolved concentrations of silica and strontium at Site 1146. The Pliocene/Miocene boundary at Site 1146 is between 308.42 and 317.99 mcd. The Pliocene section has an average LSR of 39 m/m.y. and total and carbonate MARs of 4.3 and 1.9 g/cm^2/k.y., respectively.

The Miocene-age sediments at Site 1146 (310–642 mbsf) grade from light brownish gray foraminifers and nannofossil clay mixed sediment of the late Miocene to the green nannofossil clay of the middle to early Miocene. This transition is marked by a progressive change in the sediment color from brownish gray to a distinct greenish gray. The late Miocene to early Pliocene-age interval is slightly more carbonate rich than the middle Miocene sediments, in which kaolinite and quartz become significant contributors to the mineral composition. In this lower interval, characteristic bluish green nannofossil clay appears, which contains large amounts of pyrite as nodular irregular layers or as finely disseminated particles. The carbonate content declines throughout the Miocene: 53 wt% in the upper Miocene, 35 wt% in the middle Miocene, and 30 wt% in the lower Miocene (Fig. **F17**). Over much of the Miocene–Pliocene interval, the CR L* value correlates well with the carbonate pattern but NGR and MS signals are depressed, which implies a carbonate dilution effect. Negative excursions in the chromaticity ratio a*/b* at 325, 355, and 418 mcd correspond to distinct green intervals associated with foraminifer turbidites observed in the cores. The interval from 420 to 550 mcd is marked at the top by a pronounced downhole increase in NGR and MS, which is most likely the result of the lower carbonate content and associated L* reflectance below that depth. The top of the interval from 550 to 642 mcd is defined by a sharp decrease in the chromaticity ratio a*/b*, corresponding to a color change in the cores. The MS values also drop at this depth, affirming that the drop in chromaticity is accompanied by a change in magnetic mineralogy. Overall, the sediment character is typical of deposition at bathyal depths on a continental slope, with oxygenated bottom water implying water depths exceeding the oxygen minimum zone (~600 m). However, the bulk mineralogy suggests that either a change in the source of the terrigenous material or a change in the weathering regime of the source region took place over time.

The concentration of methane (headspace analysis) increased downhole from <10 ppmv at the top to a maximum of 85,000 ppmv at 599 mcd. Ethane (C_2H_6) and propane (C_3H_8) initially appeared at 536 mcd and peaked at 608 mcd with concentrations of 155.0 and 7.3 ppmv, respectively. The C_1/C_2 ratio reached a minimum of 345 at the bottom of the hole. A major decrease in the interstitial water salinity and chloride content occurs below 500 mcd, corresponding to the top of the interval of highest methane values, the appearance of higher order hydrocarbons, changes in sediment color, and changes in physical properties. All of these changes appear to correlate with seismic Reflector T_4, which

can be traced back to a possible fault ~1 nmi from the site (see "Site 1146 [SCS-4]," p. 7, in the "Seismic Stratigraphy" chapter). This suggests that hydrocarbon and freshwater signals may have migrated laterally and that the other sedimentary changes are a diagenetic response to this change in environment.

At Site 1146 calcareous nannofossils are abundant and well preserved, although nannofossil preservation deteriorates below ~530 mcd. Benthic foraminifers are generally few but become more abundant in the lower part of the section. However, we found no clear evidence for reworked benthic foraminifers from the shelf and upper slope. Planktonic foraminifers are abundant and well preserved. The age at the bottom of the section is ~19 Ma. The Miocene section has relatively constant sedimentation rates. The upper Miocene has an average LSR of 28 m/m.y. and total and carbonate MARs of 3.7 and 2.0 g/cm^2/k.y., respectively; the middle Miocene has an average LSR of 28 m/m.y. and total and carbonate MARs of 4.2 and 1.4 g/cm^2/k.y., respectively; and the lower Miocene has an average LSR of 31 m/m.y. and total and carbonate MARs of 4.9 and 1.4 g/cm^2/k.y., respectively.

Overall, Site 1146 provides one of the most continuous Neogene sections ever recovered by the Ocean Drilling Program. The sediments are relatively high in carbonate and have rates of 30–150 m/m.y., which will allow construction of an orbital-scale stratigraphy back to the middle Miocene. This site will also allow the reconstruction of monsoon proxies that can be used to test hypotheses about the late Miocene intensification of the Asian summer monsoon and its relationship to tectonic events.

Sites 1147 and 1148

Sites 1147 and 1148 (proposed site SCS-5C) are located on the lowermost continental slope off southern China, near the continent/ocean crust boundary, and are the most offshore sites drilled during Leg 184 (Figs. F9, F18). Site 1147 (18°50.11′N, 116°33.28′E, at a water depth of 3246 m) recovered the uppermost section that appeared to be missing on seismic profiles from Site 1148 (18°50.17′N, 116°33.94′E, at a water depth of 3294 m) (see "Sites 1147 and 1148 [SCS-5C]," p. 8, in the "Seismic Stratigraphy" chapter) (Table T1). The greater water depth and distance from terrigenous sources common to these sites combine to produce lower sedimentation rates at this location, at least within the late Neogene. Site 1148 was located on the lower continental slope to take advantage of the thinner sediment thickness in order to recover the Oligocene and Miocene hemipelagic sediments that record the evolution and early paleoclimate history of the South China Sea. Elsewhere on the Chinese margin, the Oligocene sediments are too deep or are hydrocarbon bearing and thus cannot be cored to establish onset of monsoonal climates and variability in the SCS. We hoped that the combination of Sites 1148 and 1146 would provide a continuous history of accumulation rates that could be used to evaluate models of the SCS continental margin evolution, sea-level influence on deposition, and the impact of Himalayan-Tibetan uplift on monsoon onset and intensification. Site 1147 is located upslope ~0.45 nmi west of Site 1148 and was proposed during Leg 184 when Site 1148 was moved to a location within a surface slump scar (see "Sites 1147 and 1148 [SCS-5C]," p. 8, in the "Seismic Stratigraphy" chapter). Hence, Site 1147 was designed to recover the continuous sequence of the uppermost hemipe-

F18. Leg 184 seismic line across Sites 1147 and 1148, p. 63.

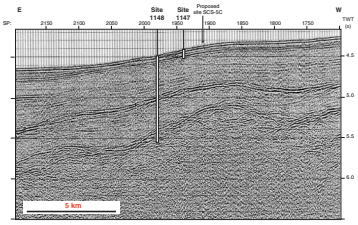

lagic sediments thought to be lost to slumping or channeling at Site 1148.

We cored three APC holes at Site 1147. Holes 1147A, 1147B, and 1147C were cored to depths of 81, 86, and 79 mbsf, respectively, with an average recovery of 99% (Table T1). At Site 1148, we cored two APC/XCB holes. Hole 1148A was continuously cored to 704 mbsf and then wireline logged with the full complement of logging tools: triple combo (111–711 mbsf), FMS-sonic (201–711 mbsf), and GHMT (201–711 mbsf). During logging operations, after we had confirmed that no significant hydrocarbons occurred over the entire interval recovered in Hole 1148A, we requested approval to deepen Hole 1148B beyond the originally approved 700 m penetration to extend the paleoenvironmental and tectonic record. Hole 1148B was APC cored to 145 mbsf; then, due to time constraints, drilled down from 145 to 440 mbsf, XCB cored to 646 mbsf, drilled down from 646 to 700 mbsf, and cored to 853 mbsf. The drilled-down intervals had excellent recovery in Hole 1148A. Downhole and bottom-water temperature measurements at Site 1148 yielded a thermal gradient of 83°C/km, which is consistent with the location and water depth.

The sediments at Sites 1147 and 1148 reflect a complex sequence of hemipelagic deposition, the beginning of which is coeval with the initiation of seafloor spreading in the South China Sea at ~32 Ma (Figs. F19, F20). The dominant lithologies are grayish green clay with quartz and nannofossils, olive-gray and reddish brown clay with nannofossils, light grayish green clayey nannofossil ooze, brown nannofossil clay, and greenish gray nannofossil clay mixed sediment. Lower sections have the same composition but contain slumped and faulted intervals. The mcd scale and splice at Sites 1147 and 1148 are based on the stratigraphic correlation of whole-core multisensor track and split-core CR data (lightness, L*) collected at 5- and 4-cm intervals, respectively. Magnetic susceptibility data were the most useful stratigraphic tool for correlation at these sites. Natural gamma radiation and CR data were helpful in intervals where structure in the MS profile was ambiguous. At Site 1147, a composite spliced section was constructed from the three holes that spans the entire interval from 0 to 91.7 mcd. At Site 1148, an mcd scale was constructed over the entire cored sequence, 0 to 860 mcd. However, because of core recovery gaps throughout the sequence, the scale is discontinuous ("floating") rather than linked to the sediment/water interface. A floating splice that extends from 46.57 to 155.34 mcd can be combined with data from nearby Site 1147 to construct a continuous mcd and splice, extending from 0 to 155.34 mcd.

Sediments of Pliocene–Pleistocene age at Sites 1147 and 1148 (0 to ~190 mcd) are composed of intensely bioturbated clay with quartz and nannofossils; the upper part is more clay rich and the lower part more nannofossil rich. Green clay layers and irregular green clay mottles decrease downsection, whereas lighter intervals with increased nannofossil content increase slightly downhole as do L* value, MS, and bulk density. Siliceous microfossils are abundant in the upper Pleistocene and decrease rapidly to zero in the Pliocene. The core and wireline logging data show that the Pleistocene part of the section (to ~160 mcd) is characterized by a downhole increase in MS, which decreases during the Pliocene interval. A number of properties, including bulk density, porosity, and *P*-wave velocity, show typical downhole patterns related to compaction and dewatering. Natural gamma radiation and CR display more complex patterns related in part to the carbonate content. Almost all properties show the cyclic fluctuations that are associated

F19. Summary diagram of coring results at Site 1147, p. 64.

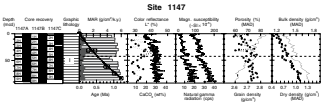

F20. Summary diagram of coring results at Site 1148, p. 65.

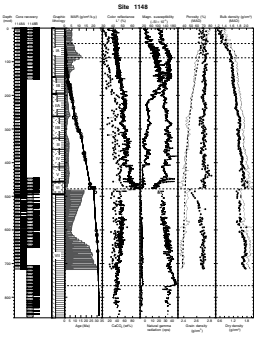

with orbital-scale climate changes. The Miocene/Pliocene boundary is marked by an increase in the light carbonate-rich nannofossil clay layers and the disappearance of pyrite concretions. Total organic carbon decreases systematically from a maximum of 0.8 wt% at the top of the hole to <0.2 wt% by 130 mcd and remains at this level throughout the Miocene (to ~485 mcd). Based on C/N values, a purely marine organic source for organic matter is suggested for the upper 130 m of Site 1148. The variation in sulfur abundance follows that of TOC in the top 130 m of the hole, decreasing slowly with depth but exhibiting a normal marine S/C ratio (0.4). Interstitial water profiles at Site 1148 are dominated by sediment/water exchanges driven by sulfate reduction in the upper 110 mcd. Sulfate values never reach zero, indicating that sulfate reduction is incomplete and methanogenesis is limited. The upper Pleistocene interval has high dissolved silica, which correlates with the higher number of siliceous organisms in the sediment.

Calcareous nannofossils and planktonic foraminifers are abundant and well preserved in Pliocene/Pleistocene sediments. At Site 1148 (1147), the Brunhes/Matuyama boundary can be tentatively placed at 55.2 (58) mcd, the upper Jaramillo Subchron at 69.1 (71) mcd, the lower Jaramillo at 73 (76) mcd, the upper Olduvai Event at 111.4 mcd, and the lower Olduvai (tentatively) at 118.5 mcd. The age of the oldest sediments recovered at Site 1147 is estimated at 1.22–1.47 Ma. The combined biostratigraphy placed the Pleistocene/Pliocene boundary between 125.8 and 135.5 mcd and the Pliocene/Miocene boundary between 184.5 and 193.8 mcd.

The Miocene-age sediments at Site 1148 (~190–475 mcd) are a mixture of olive-gray and reddish brown clay with nannofossils, light grayish green clayey nannofossil ooze, brown nannofossil clay with intervals and patches of reduced green ooze, and greenish gray nannofossil clay mixed sediment and nannofossil clay. The wireline logs of this interval reveal downhole increases in bulk density, electric resistivity, *P*-wave velocity, and photoelectric effect (PEF) but decreases in neutron porosity (Fig. **F20**). Similar to the core-log data, MS has several local maxima but decreases downhole. Natural gamma radiation is variable but has no long-term trend until the lowermost Miocene, when it rapidly decreases at the slumped section. None of the units above the slumped section shows any evidence of sediment redeposition; they are representative of continuous hemipelagic sedimentation. These lithologic changes are reflected in the carbonate content and especially the CR a* and L* variations. The lowermost sediments have relatively high concentrations of diagenetically precipitated "iron sulfide," seen as black, fine-grained material. Trace fossils are common, most notably *Zoophycos* and *Chondrites,* both characteristic deep-water (bathyal) forms. Evidence for redeposition in the lower Miocene sediments is sparse, although a few thin carbonate sand turbidites do occur.

Interstitial water profiles in the Miocene and Oligocene interval are dominated by sediment/water exchanges driven by volcanic alteration, clay mineral diagenesis, and calcite recrystallization at depth. Sulfate values never reach zero, indicating that sulfate reduction is incomplete and methanogenesis is not an important process in these sediments. As a result, the higher methane values at depth are related to thermogenic production of hydrocarbons.

The Oligocene-age sediments at Site 1148 (475–852 [mcd]) represent a major change in deposition. The uppermost Oligocene sediments are light tan in color, which reflects a distinct increase in carbonate content and the associated CR a* and L* values (Fig. **F20**). This interval is also

marked by a sharp increase in *P*-wave velocity, PEF, bulk density, and low porosity. These properties most likely reflect the increased carbonate content in this interval (50–75 wt%) and are probably responsible for prominent double reflectors seen in seismic reflection profiles. The sonic *P*-wave velocity of this interval is 2.3 km/s, which is substantially greater than the value of 2.1 and 1.9 km/s at the top and bottom of this interval, respectively. Although similar in composition to overlying sediments (i.e., dominantly clay nannofossil mixed sediments and nannofossil clays), this layer represents gravitational redeposition by mass flows and slumping as evidenced by convolute bedding, soft-sediment plastic deformation, and the presence of light-colored carbonate mud clasts within a massive bed of light gray to grayish brown nannofossil clay. These sediments also show clear evidence of brittle faulting in the form of small normal microfaults and thus are likely related to tectonic activity in the formation of the South China Margin. However, the matrix sediments often contain a deep-water trace fossil assemblage of *Zoophycos* and *Chondrites* and provide no evidence that water depths differed significantly from the overlying Miocene sediments. "Iron sulfides," pyrite concretions, and green clay layers are rarely observed. A sudden increase in TOC is noted below 485 mcd (>0.4 wt%), and the concentration of TOC remains in this range downhole (0.2–0.5 wt%). The higher C/N values in the lower section may indicate significant terrestrial input. Just below the slumped interval, salinity and chlorinity values become more variable, and ammonium and silica values increase. Changes in ammonium (as well as chloride and salinity) below 470 mcd may also be related to the dehydration reaction of clay minerals. In this interval, XRD data show that below 470 mcd, smectite, illite, and kaolinite are absent and an unidentified mixed-layer clay appears. The slump and the underlying chalk layer may act as a barrier to diffusion of gas and possibly to some elements dissolved in interstitial waters. The microenvironments within fractures may also lead to variable interstitial water concentrations in this lower interval.

The bulk of the Oligocene sediment is an intensely bioturbated sequence of quartz-rich, grayish olive-green nannofossil clay. The whole sequence is extremely monotonous, with little lithologic variation, and is characterized by low values of MS, bulk density (although disturbed by the XCB coring), NGR, and PEF and by decreased L* but increasing a*/b* parameter of CR. These trends generally reflect the decreased carbonate and increased clay content in the rapidly accumulating Oligocene section. The abundant bioturbation traces are strongly compacted and give the sediment a laminated appearance. A higher interstitial water dissolved silica concentration in the mid-Oligocene interval is associated with intervals of higher biogenic silica content. Toward the base of the section, evidence of current activity is found in the form of occasional flaser sandstone laminae that are dominated by quartz and lithic fragments as well as mica, glauconite, and foraminifer fragments. As with younger sediments, little evidence suggests that these early Oligocene sediments were deposited in substantially shallower water.

In the Oligocene sediments, total sulfur concentration increases, following TOC. However, the S/C ratio is anomalously high for normal marine sediments (>1), suggesting the addition of sulfur from another source. An increase in methane to the bottom of the hole (711 mcd) is accompanied by the presence of ethane and propane as well as heavier hydrocarbons downhole. Maximum methane and ethane concentrations were detected at 593 mcd (569 and 25 ppmv, respectively). From the first detection of ethane at 480 mcd, the C_1/C_2 ratio declined rap-

idly from 99 to approach a minimum of 15 at the bottom of Hole 1148A. Between 715 and 851 mcd, methane concentrations remained low (<200 ppmv) and decreased with depth downhole. The C_1/C_2 ratio decreased to as low as 4; this was expected, however, because of the small amounts of organic matter in these poor source rocks as they entered the zone of petroleum maturation. As much as 50 ppmv of C_5 and lesser amounts of other light hydrocarbons were detected.

Thirty-nine nannofossil and 29 planktonic foraminifer biostratigraphic datums were recognized from the lower Oligocene to Pleistocene sediments at Site 1148. A gap in the nannofossil and foraminifer datums indicates that sediments between the lowermost part of Zone NP25/Zone P22 to Zone NN2/Zone N4 are missing and that the base of Hole 1148B is still within Zone NP23/P19 (<32.3 Ma). Site 1148 yields few to abundant deep-sea benthic foraminifers, and the ratio of benthic to planktonic foraminifers is high in the Oligocene. The benthic foraminifers (e.g., *Heterolepa, Gavelinopsis, Globocassidulina, Martinottiela, Sigmoilopsis, Textularia,* and *Uvigerina*) in the lower part of Hole 1148A (>~510 mcd) are comparable to those observed at 1000–2000 m in the modern South China Sea. An increase in the abundance of *Globobulimina* and *Chilostomella* (indicative of high productivity) was observed in the upper (above ~50 mcd) and lower (below ~500 mcd) sections of Hole 1148A. This corresponds to the higher organic carbon content and abundant siliceous fossil content (radiolarians and diatoms) found in the two intervals. Down to the middle Miocene, nannofossils are moderately to well preserved, and planktonic foraminifers are poorly to moderately preserved; in the lower section (Oligocene), foraminiferal tests are recrystallized, and some nannofossils show postburial overgrowth.

The stratigraphy at Site 1148 spans most of the postrift history of the South China Sea, including the entire duration of active seafloor spreading (Briais et al., 1993). Despite this, apart from a series of sharp color changes and associated differences in physical properties and carbonate content, very little lithologic variation has occurred since the early Oligocene. Lithologically, we found no apparent deepening or shallowing of the water depth of sedimentation, remaining hemipelagic and probably bathyal throughout. The most noteworthy sedimentary feature at Site 1148 is the mass-flow sequence, which is also responsible for the prominent reflector at the base of the Miocene section. Ironically, the strong basement reflector at ~800 mbsf is within the gray-green Oligocene clays and does not show any distinct lithologic change (although recovery in this section was poor).

ENVIRONMENTAL HISTORY OF THE SOUTH CHINA SEA

Leg 184, the first major Ocean Drilling Program campaign in the South China Sea, recovered a continuous sequence of deep-sea sediments that spans the past 32 m.y. The geographic distribution of drill sites allows a comparison for the last 10 m.y. between the northern and southern parts of the South China Sea. The water-depth distribution of sites on the northern continental slope will allow comparisons between records from above and below the modern Bashi Strait sill depth (~2600 m), which connects the Pacific Ocean with the South China Sea. On the

upper slope, we also recovered a section with extremely high sedimentation rates of >800 m/m.y. for the late Pleistocene.

Sedimentary Context

Lithology

The South China Sea sediments recovered during Leg 184 represent the mixing of nannofossil ooze and detrital clays derived from the Asian continent on the northern and western margins and the island arcs on the southern and eastern margin. These fine-grained, hemipelagic sediments appear to represent deep-water deposition throughout the Neogene and back into the early Oligocene. The apparently monotonous lithology, however, does show significant changes in percentage of biogenic $CaCO_3$ (from a few percent to nearly 80%), with cyclic fluctuations in the Pliocene–Pleistocene sections. Bioturbation is ubiquitous throughout the sequences, whereas slumping and sediment plastic and brittle deformation occur only at certain sections (such as the bottom of Site 1143, the Oligocene/Miocene boundary, and the bottom of Site 1148), indicating periods of tectonic activity.

All cores are rich in calcareous microfossils, dominantly nannoplankton and planktonic foraminifers (Fig. F21). The microfossils are well preserved in most of the cores. Dissolution effects are significant only for certain sections of deeper sites such as Sites 1145 and 1148, and the Oligocene section contains recrystallized foraminiferal tests. Despite the variations in preservation and the frequent reworking of nannofossils, the two microfossil groups yielded some 70 datum levels from the early Oligocene onward for the stratigraphic framework of the leg. All fossil assemblages are deep water in nature, and benthic foraminifers are rare aside from the Oligocene. Siliceous fossils (diatoms and radiolarians) are frequent in the uppermost part of the holes and in some lower sections at certain sites. Ostracods, bryozoans, pteropods, and other macrofossils have been encountered only in some parts of the sequences. The presence of small pieces of fossil wood, although rare, implies transport of plant debris from land. The high diversity and abundance of microfossils offer an ideal opportunity for paleoenvironmental reconstructions.

The volume of volcanic ash found in Leg 184 sediments is not large. All recovered ashes are thin, generally <5 cm, and are light colored in the Pleistocene, reflecting the dominant dacitic-rhyolitic composition of the arc's explosive fraction. Most of the ashes were deposited since 1 Ma on the northern margin and since 2 Ma in the south. The uphole increase in volcanic ash may reflect either more volcanic eruptions during the Pleistocene or the diagenetic alteration (loss) of chemically unstable volcanic glass in the older, deeper parts of the section. This latter explanation may account for much of the pattern on the northern margin because older ashes in this area tend to be devoid of glass and are simply composed of angular quartz, mica, and other accessory mineral grains. However, fresh glass is found in Miocene-age ash beds at several sites.

Green clay layers are a common, yet volumetrically small, part of the sequence at most of the Leg 184 core sites. They occur as discrete layers as thick as 3 cm and even more commonly as disrupted layers, patches, or mottles. The XRD analyses show that they are not composed of glauconite. No clear relationship is observed between green clay layers and depth of burial, although most of the layers are confined to the

F21. Coring penetration and lithologic units as a function of age, p. 66.

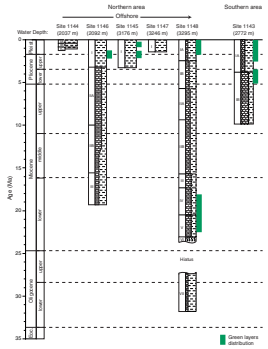

Pliocene–Pleistocene (Fig. F21) except for a lower Miocene set recovered at Site 1148. Their common association with burrows and patches caused by burrowing suggests that they may be linked to the former presence of organic matter. Certainly their green color is suggestive of reducing conditions, which are linked to organic matter alteration. They do not seem to be equivalent to green layers found by Lind et al. (1993) on the Ontong Java Plateau and by Gardner et al. (1986) from the Lord Howe Rise, which were interpreted as altered volcanic ash. In the case of the South China Sea, the green clay layers are interbedded with clear tephra-bearing unaltered volcanic glass. No appreciable change in the background sediment is noted over these intervals; thus, the diagenetic environment seems uniform between beds. Other diagenetic minerals noted in the Leg 184 sediments are "iron sulfide" minerals (well-crystallized golden-colored pyrite often present as nodules, concretions, and replacement burrows) and fine-grained black sulfide dispersed in the sediment. The latter style is described as "FeS" in the cores, but this is chemically unstable; therefore, this material must also be pyrite in mineralogy. The lack of a clear regional pattern either in depth or age in the distribution of pyrite or "FeS" suggests that the minerals' development reflects only local variations in sediment composition and burial.

Interstitial Waters: Silica and Sulfate

The interstitial water profiles measured during Leg 184 reflected sulfate reduction and methanogenesis in the upper sediments. Below the zone of organic matter reduction, interstitial water profiles reflected alteration of volcanic ashes, diagenesis of clays, dissolution of silica, and dissolution/recrystallization of calcite at depth. These data revealed two clear trends in the SCS sediments:

1. The extent and depth of sulfate reduction reflects both the supply of organic matter and the large range of sedimentation rates.
2. Dissolved silica increases across the SCS at ~1 Ma.

We found that the sulfate gradient (i.e., the decrease in sulfate values from oceanic values, 28.9 mM, to the value of the sulfate plateau) increased linearly with sedimentation rate but not with the TOC concentration. The sulfate gradient is controlled both by the supply of organic matter to be consumed by sulfate reduction and by the extent to which seawater sulfate can continue to diffuse into interstitial water and replenish the sulfate removed by sulfate reduction. Hence, the linear relationship between sulfate gradient and sedimentation rate is established both by the correlation between high LSR and higher TOC flux to the seafloor and by the length of time that near-surface sediments continue to receive new sulfate from seawater. The extreme sulfate gradient observed at Site 1144 appears to be more a function of high sedimentation rates than the supply of organic matter because the LSR is so high (250–1000 m/m.y. in the Pleistocene) that sediments move out of the diffusional contact with seawater faster than organic matter can be depleted. This rapid removal of organic matter from the zone of sulfate reduction is consistent with the good preservation of organic matter with depth at this site. All other sites follow a more linear relationship between sulfate gradient and both LSR and TOC. Site 1143 has the lowest values observed and is the most distant from continental sources.

All the dissolved silica profiles showed an increase of similar magnitude between ~1 and 0.5 Ma, which corresponds to an increase in the abundance of biogenic silica in the sediments (Fig. F22). This increase in dissolved silica occurs at very different depths at different sites, suggesting that it is not related to diagenetic changes in silica. Instead, the increase in dissolved silica indicates that the higher biogenic silica observed in the sediments is a real change in silica flux to the sediments. These changes are coincident with increasing sedimentation and organic carbon accumulation rates, which could indicate increased preservation related to a higher LSR and higher overall productivity. In either case, the increase in silica appears to be a regional change, suggesting that it is caused by climatic or tectonic changes.

F22. Summary of silica concentration trends in interstitial water, p. 67.

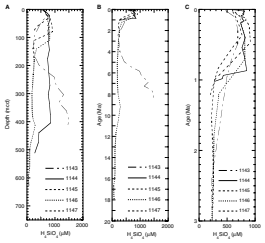

Geothermal Gradients: Tectonics and Hydrocarbon

The downhole temperature measurements at Leg 184 sites revealed two distinct temperature gradients as a function of the water depth (Fig. F23). At Sites 1143 (2772 m), 1145 (3175 m), and 1148 (3294 m), the gradients were relatively high (83° to 90°C/km) and were quite similar between the sites. These sites are all deep and relatively close to the boundary between continental and ocean crust. Preliminary calculations suggest that temperature gradients at these sites are close to predictions based on the pure shear stretching model of continental lithosphere, the corresponding water depth of the drill sites, and the assumed age of initial rifting (32 Ma). The two sites on the mid-continental slope (Sites 1144, 2037 m; and 1146, 2092 m) have smaller gradients (24° and 59°C/km, respectively) and differ from the deeper sites and from each other. The gradient at Site 1144 is substantially smaller than the predicted value based on water depth and spreading age, and a local process must be inferred to explain the low temperatures at this high sedimentation rate site.

F23. Downhole temperature gradients from Leg 184 sites, p. 68.

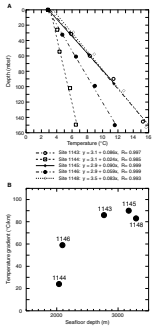

Significant hydrocarbon concentrations were detected at three sites during Leg 184 (Fig. F24). Abundant methane of biogenic origin was inferred only from Site 1144. High TOC abundance and complete sulfate reduction in the upper few meters of this site (and the absence of significantly heavier hydrocarbons downhole) are characteristic of methanogenesis in immature sediments. In contrast, the downhole increase in hydrocarbon abundance at Sites 1146 and 1148 is characteristic of thermogenic generation with age and increasing temperatures with depth. These two deeper penetration sites on the continental margin have predicted bottom-hole temperatures of only 35°C at Site 1146 (607 mbsf) but 71°C at Site 1148 (853 mbsf). The temperatures in the lower interval of Site 1148 are thought to be high enough to begin the process of thermal generation of hydrocarbons from the low amounts of organic carbon (0.3 to 0.5 wt%) and may well explain the observation of sparse, heavy hydrocarbons (C_{2+}) at the site. The Leg 184 sites did not reveal conditions for source rock production (except Site 1148, where low TOC produced small amounts of C_1–C_5), and no gas hydrates were directly observed.

F24. Summary of methane concentrations at Leg 184 sites, p. 69.

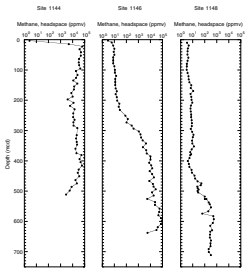

Synthesis of Environmental History

In summary, the sequence of hemipelagic sediments over 32 m.y. is rich in calcareous microfossils and yields almost continuous records of the environmental history of the South China Sea. The depositional history of the northern slope had three important stages: the Oli-

gocene, with extremely high sedimentation rates; the Miocene and early Pliocene, with a low sedimentation rate and high carbonate content; and the last 3 m.y., with high clastic sediment accumulation rates. A different trend of depositional history is indicated at the southern Site 1143: the carbonate accumulation rate decreases from the late Miocene toward the late Pleistocene, and the noncarbonate rate rises again after 3 Ma. However, the upper Miocene sediments were similar in composition between the northern and southern sites, containing more than 50 wt% carbonate.

Oligocene: the Seafloor-Spreading Phase (Site 1148)

The lower and mid-Oligocene sediments (Site 1148; 32–27 Ma, 850–480 mcd) are composed of laminated claystone with brownish gray and greenish gray stringers (Figs. **F20, F21**) and have high LSRs comparable to those in the Pleistocene (Figs. **F25, F26**). The carbonate MAR from 480 to 700 mcd (23.7–31.0 Ma) averages 3.45 g/cm²/k.y. (Fig. **F26**), which is by far the highest observed over the past 32 m.y. at Site 1148. At the same time, the relatively high noncarbonate MAR implies a significant supply of terrigenous fine-grained clasts (Fig. **F26**). Because the ratio of carbonate to noncarbonate MAR is relatively constant, the high carbonate accumulation rate may reflect sediment focusing of upslope sediments as well as a higher surface productivity. The relatively high organic carbon content, the presence of siliceous microfossils, and the composition of benthic foraminiferal fauna also suggest higher productivity.

On the basis of magnetic anomaly (C11–C5c) patterns, the seafloor-spreading phase of the SCS took place between 32 and 16 Ma (Briais et al., 1993; Taylor and Hayes, 1983). Before 27 Ma, the newly opened deep-sea basin was oriented east to west and connected with the Pacific in the East. At that time, the South China Sea was a narrow basin between the Asian continent and a number of terranes that were eventually rifted to the southern part of the SCS (North Palawan and Reed Bank, among others). The high sedimentation and accumulation rates recorded at Site 1148 may be related to the incipient spreading phase, which might focus sediment input into the newly opened basin. Judging from the absence of marine sediments of this age on the northern shelf and upper slope, the ocean waters were restricted in the area. The proximity of continental runoff and sediment transport may be one of factors responsible for the higher rates of deposition in this interval. The poor core recovery in the upper part of this sequence (473–562 mcd) suggests some lithologic changes in the latter part of the time interval. The scarcity of core samples, however, precludes any conclusion about the nature of the possible events.

Lower Oligocene coal-bearing swamp and littoral plain sediments are known to occur in wells of this age farther north within the Pearl River Mouth Basin (e.g., Su et al., 1989). The lack of similar coarse clastic material suggests that the Pearl River Mouth Basin and shallower slope basins were acting as efficient sediment traps. In addition, the presence of a deep-water, bathyal facies during the initial seafloor spreading period does not readily fit with simple rift models of the South China Margin. These facies may indicate that the margin extension proceeded very rapidly during the initial rifting phase in the middle Eocene (e.g., Taylor and Hayes, 1980; P. Clift and J. Lin, pers. comm., 1999).

A distinct and regionally consistent seismic reflector was observed in the lower section of Site 1148. The *JOIDES Resolution* seismic reflection

F25. Age-depth relationships for Leg 184 sites, p. 70.

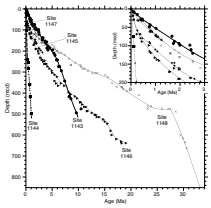

F26. Summary of total and carbonate MARs vs. age, and LSRs, p. 71.

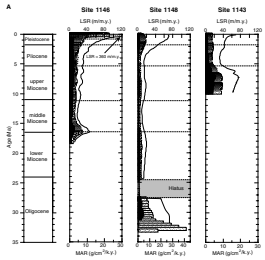

data indicated that the reflector was ~0.86 s below seafloor; the *P*-wave velocity data from downhole logging in Hole 1148A suggested that the reflector was ~800 mbsf. Although the drillers reported a distinct decrease in penetration rate at 800 mbsf, we did not recover any material that was obviously indicative of a strong reflector. All cores in this interval were greenish gray claystone. The lack of coarse sediments, a weathering zone, or other features indicative of erosion or shallower water signify that this site was relatively deep throughout the deposition of the Oligocene sequence. The true nature of the reflector is unclear.

Oligocene/Miocene Boundary: a Turning Point (Site 1148)

The latest stage of the late Oligocene produced drastic changes in sediment deposition at Site 1148. Above a section of poor core recovery but with clear late Oligocene index species (P21b and NP24) below 477 mcd, carbonate content abruptly increased (~50–70 wt%) as chalk replaced clay over the depth interval of 454–477 mcd (Fig. **F27**). Almost all physical parameters reflect this rapid change, including sharp increases in bulk density, *P*-wave velocity, photoelectric effect, and CR parameters and decreases in porosity, NGR, and MS values (Figs. **F20, F28**). The microfossil assemblages at 454 m indicate an early Miocene age (N4, NN2). The chalk section is overlain by slump deposits of chalk and clay with a mixed nannofossil assemblage. The absence of nannofossil Zone NP25 indicates a deposition hiatus of ~1–3 m.y. at the end of the Oligocene (Figs. **F20, F25, F26**), and planktonic foraminifer markers between the lowermost Zone N4 and lowermost Zone P22 indicate a hiatus spanning from ~24 Ma to ~27.0–27.5 Ma.

The Oligocene–Miocene transition represents one of the most significant Cenozoic changes in the tectonic and environmental history of the South China Sea (Wang, 1990). Although this period is within the drift phase of SCS evolution, the sedimentary basins of the northern SCS shelf are thought to have experienced a transition from the rifting stage to one of broad subsidence (Ru et al., 1994). According to the age model for Site 1148 (Fig. **F25**), the Oligocene/Miocene boundary events started ~27 Ma, at the same time that the spreading ridge of the SCS basin is thought to have jumped southward (Briais et al., 1993). Because of its position close to the boundary between continental and ocean crust, Site 1148 should have been sensitive to any tectonic episode associated with changes in the spreading of the SCS basin. Postcruise research will show whether the drastic changes in deposition regime at the site is related to the spreading event.

Early Miocene: Carbonate Deposition and Transgression (Sites 1146 and 1148)

The early Miocene (16.5–23.7 Ma) at Sites 1146 and 1148 is represented by a calcareous clay with an average carbonate content of ~35 wt% (Fig. **F27**). The total MARs for this interval average 1.13 g/cm²/k.y. at both Sites 1146 and 1148, or about three times lower than in the Oligocene (Fig. **F26**). These lower rates are more representative of pelagic sedimentation and may also imply that the previously high rates were affected by sediment focusing on the margin. During the second stage of seafloor spreading (27–16 Ma), the South China Sea basin became much broader than in the Oligocene (Briais et al., 1993; Lee and Lawver, 1994). This early Miocene interval was distinguished by an expansion of reef facies in the shallow waters of the western Pacific in-

F27. Summary of carbonate concentration vs. age, **p. 73.**

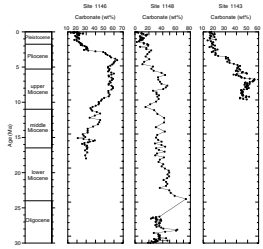

F28. Downhole logs as a function of depth, **p. 74.**

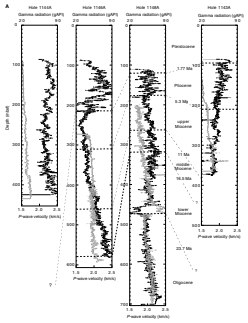

cluding the Pearl River Mouth Basin (Fulthorpe and Schlanger, 1989). The relatively low carbonate accumulation rate but high carbonate content may be attributed to the more pelagic environment of the larger SCS basin, the lack of sediment focusing, and the wide distribution of reef facies on the shelves.

On the northern shelf, the early Miocene was a time of marine transgression. The marine intercalations in nearshore facies are first observed in the upper Oligocene (NP25) on the upper slope and shelf break in industrial wells (BY7-1-1, at a water depth of 499 m; and PY33-1-1, at a water depth of 188 m; Huang, 1997), and in the lower Miocene on the shelf (Wang, 1990). Further studies are needed to determine whether the local rise in sea level resulted from global eustatic changes or from tectonic subsidence of the basins as well as how this shelf transgression phase affected sedimentation at the deeper water Sites 1146 and 1148.

Middle Miocene: after the Spreading (Sites 1146 and 1148)

The seafloor-spreading phase of the SCS basin stopped at magnetic Anomaly C5c, or ~16 Ma, which is close to the boundary between the early and middle Miocene (also close to the T_4 reflector). The middle Miocene section (~16–11 Ma) from the northern continental margin (Sites 1146 and 1148) has relatively high carbonate content (>30 wt%), only slightly lower than the early Miocene but much higher than the modern values (Fig. **F26**). Carbonate increases at the shallower Site 1146 and remains high at Site 1148 despite its greater water depth, which is below the modern lysocline (~3000 m). Total accumulation rates during the early Miocene were 1.91 g/cm²/k.y. at Site 1148, slightly lower than in the early Miocene and much lower than at Site 1146 (~4.34 g/cm²/k.y.) (Fig. **F27**). Additional postcruise biostratigraphic control will be needed to establish whether the slower accumulation rates are related to a change in tectonics or to depositional hiatuses observed on the northern shelf.

Late Miocene: High Carbonate Supply (Sites 1143, 1146, and 1148)

Upper Miocene sediments were recovered in the northern SCS at Sites 1146 and 1148 and in the southern SCS at Site 1143. About half of the mass of sediments from both northern and southern sites above the modern lysocline (Sites 1146 and 1143) is composed of carbonate (Figs. **F26A, F27**). At Site 1143, the carbonate and noncarbonate accumulation remains high (Fig. **F26A**); Site 1146 shows a drastic increase in carbonate percentage (from ~40 wt% in the middle Miocene to ~55 wt% in the late Miocene), but the increase in carbonate accumulation rate was not significant (from 1.46 g/cm²/k.y. in the middle Miocene to 1.55 g/cm²/k.y. in the late Miocene) (Figs. **F26A, F27**). At Site 1148, the average carbonate percentage still exceeds 30 wt% (Fig. **F27**), but the poor preservation of planktonic foraminifers shows enhanced carbonate dissolution. During this late Miocene interval, differences begin to develop between the shallower Site 1146 and the deeper Site 1148. In the shallow site, NGR values are lower and decreasing whereas PEF values are increasing; in the deeper site, the NGR values are higher and much more variable, as are the PEF values. These changes suggest more clay carbonate contrasts in the deeper Site 1148 and are generally consistent with the higher carbonate in Site 1146.

Despite the similar carbonate concentrations in upper Miocene sediments, the accumulation rate at Site 1143 is about two times higher (~3 g/cm²/k.y.) than at Site 1146 (~1.5 g/cm²/k.y.) (Figs. F26, F27). The high carbonate accumulation at tropical Site 1143 might be related to the late Miocene to early Pliocene "biogenic bloom" in the equatorial Pacific (Berger et al., 1993; Farrell et al., 1995) but also seems partly related to redeposition of adjacent sediments as evidenced by the frequent turbidites and slumped sediments in the lower section. The preservation of siliceous microfossils in the lower section may indicate higher productivity at that time. The high carbonate percentages in the Miocene deposits from the northern sites imply a low supply of terrigenous material from the land that may be related to rising sea levels during this interval (Prell and Kutzbach, 1997). In general, the high carbonate sediments throughout the Miocene and the similarity between the northern and southern sites suggest a much more stable environment than during the Pliocene–Pleistocene.

Pliocene and Pleistocene: Increase of Terrigenous Input (Sites 1143, 1144, 1145, 1146, 1147, and 1148)

Leg 184 recovered Pliocene deposits at four sites (1143, 1145, 1146, and 1148) and Pleistocene sediments at all six sites, although with substantially different accumulation rates (Fig. F26B). Despite the different LSRs, all sites exhibit a significant increase in silica at ~1 Ma (Fig. F22), which can be ascribed to increased productivity and/or increased preservation. Differences between the southern and northern SCS also begin to emerge during this interval.

At the southern Site 1143, both carbonate and noncarbonate accumulation rates decreased from the late Miocene to Pliocene (Fig. F26B): carbonate from 2 to 4 g/cm²/k.y. to ~1 g/cm²/k.y., and noncarbonate from 3 to 4 g/cm²/k.y. to ~2 g/cm²/k.y. The decreasing trend continues to the Pleistocene for carbonate, whereas the noncarbonate rate increases again after ~3 Ma, indicating some increased supply of terrigenous material. However, unlike the northern sites, the MAR at Site 1143 decreases toward the present despite the increase in LSR, a result of decreased bulk density within that most recent interval.

On the northern continental margin, Pliocene accumulation rates remain at the late Miocene level at Sites 1146 and 1148 but with slightly lower rates in the deeper Site 1148. Both sites exhibit the rapid increase in LSR and noncarbonate deposition that started at ~3 Ma. Site 1145 records only the past 3 m.y., but the noncarbonate accumulation increases after ~ 2.5 Ma. This apparently regional increase in noncarbonate accumulation may be evidence for an intensification of erosion that is related to climatic/sea-level and/or tectonic events. For example, Chinese geologists report evidence for significant uplift of the Tibetan Plateau at ~3 Ma (e.g., Li et al., 1996), and the widespread accumulation of loess in central China started at ~2.4 Ma. However, sea-level changes associated with increased global glaciation may have also contributed to transporting sediments to these continental margin sites.

In contrast to the southern site, all the northern sites show an increase in MAR in the late Pleistocene, especially the last ~0.25 m.y. (Fig. F26B). The higher MAR is mainly the result of increased supply of terrigenous material, as the carbonate contribution is insignificant for that time interval. The trend is most prominent for Sites 1144, 1145, and 1146. The cause of this most recent increase is not yet clear. The rela-

tively high content of biogenic silica and organic carbon indicate enhanced productivity for the latter part of the Pleistocene.

The general decrease in carbonate concentration upsection, particularly since the mid-Pliocene (Figs. F21, F26, F27), could also reflect decreasing carbonate productivity as well as increasing clastic input, both of which might be expected from an intensification of glaciation at that time. Glaciation is known to have produced arid conditions in Asia and reduced runoff into the South China Sea, although windblown material such as loess may be more important at these times. However, glaciation in the Himalayas (and possibly Tibet) would be expected to produce more clastic debris that would then be available for redeposition when rainfall increased again at the start of deglaciation. The increasing strength of glacial cycles, especially since ~2.6 Ma, correlates well with the general increase in the detrital component since that time. The variation from darker to lighter sediment intervals noted at a number of the northern margin sites—more precisely represented as cyclic variations in core-logging data such as CR, NGR, and MS—most likely reflects such glacial–interglacial variation in clay and carbonate accumulation.

CONCLUSIONS

Leg 184 recovered a sequence of hemipelagic sediments that records the past 32 m.y. of environmental history of the South China Sea. For the first time in the lower latitude western Pacific, these cores provide a high-resolution continuous record of relatively carbonate-rich fine-grained sediments and a possibility of sea-land correlation of the upper Cenozoic stratigraphy for the region.

The lithologies, microfossils, and physical properties of the hemipelagic sequence reveal significant trends, clear cyclicities, and abrupt changes that provide detailed records of environmental transformations, including provenance and volcanism. The most prominent are variations in CR, MS, and NGR, which exhibit obvious orbital-scale and finer fluctuations in monsoonal climate.

The discovery of high-accumulation-rate (5–20 g/cm^2/k.y.) Oligocene hemipelagic sediments on the lower continental slope near the continental crust margin probably reflects active downslope transport of terrigenous sediment during the early stage of seafloor spreading of the South China Sea basin. This “deep-water” sequence continues below the “acoustic basement,” which might be a thick marine Paleogene section.

The Oligocene/Miocene boundary in the northern SCS is marked by sedimentary deformation, abrupt lithologic changes, and a stratigraphic hiatus. These related features will help resolve the nature and timing of one of the most significant Cenozoic tectonic and climate changes of the region.

Cores from all drill sites show a high carbonate content for the Miocene and lower Pliocene in both the northern and southern South China Sea. The low terrigenous input and partly high carbonate production resulted in a sedimentary environment on the northern slope similar to that near the reef areas in the southern part of the sea in the Miocene; accumulation rates, however, are significantly different in the northern and southern SCS after the Miocene.

A general increase of noncarbonate sediment accumulation after 2–3 Ma was found at all drill sites; for the northern sites, the increase has become even more significant in the latter part of the last million years.

A site with exceptionally high rates of hemipelagic fine-grained sedimentation (Site 1144, ~500 m of sediment in the last 1 m.y.) offers a unique opportunity for fine-resolution paleoenvironmental studies at decadal scale.

REFERENCES

An, Z., Liu, T.S., and Liu,Y.C., et al., 1990. The long-term paleomonsoon variation recorded by the loess-paleosol sequence in central China. *Quat. Int.,* 7/8:91–95.

Anderson, D., and Webb, R.S., 1994. Ice-age tropics revisited. *Nature,* 367:23–24.

ASCOPE, 1981. *Tertiary Sedimentary Basins of the Gulf of Thailand and South China Sea: Stratigraphy, Structure and Hydrocarbon Occurrences:* Jakarta (ASCOPE).

Berger, A., and Loutre, M.F., 1991. Insolation values for the climate of the last 10 million years. *Quat. Sci. Rev.,* 10:297–317.

Berger, W.H., Leckie, R.M., Janecek, T.R., Stax, R., and Takayama, T., 1993. Neogene carbonate sedimentation on Ontong Java Plateau: highlights and open questions. *In* Berger, W.H., Kroenke, L.W., Mayer, L.A., et al., *Proc. ODP, Sci. Results,* 130: College Station, TX (Ocean Drilling Program), 711–744.

Bian, Y., Wang, P., and Zheng, L., 1992. Deep-water dissolution cycles of late Quaternary planktonic foraminifera in the South China Sea. *In* Ye, Z., and Wang, P. (Eds.), *Contributions to Late Quaternary Paleoceanography of the South China Sea:* Qingdao (Ocean Univ. Press), 261–273. (in Chinese, with English abstract)

Briais, A., Patriat, P., and Tapponnier, P., 1993. Updated interpretation of magnetic anomalies and seafloor spreading stages in the South China Sea: implications for the Tertiary tectonics of Southeast Asia. *J. Geophys. Res.,* 98:6299–6328.

Cerling, T., 1997. Late Cenozoic vegetation change, atmospheric CO_2, and tectonics. *In* Ruddiman, W.F. (Ed.), *Tectonic Uplift and Climate Change:* New York (Plenum), 313–327.

Chen, L., Zhu, G., Luo, H., He, J., Dong, M., and Feng, Z., 1991. *The East Asian Monsoons:* Beijing (China Meteorological Press). (in Chinese)

Chen, M.T., and Huang, C.-Y., 1998. Ice-volume forcing of winter monsoon climate in the South China Sea. *Paleoceanography,* 13:622–633.

Chen, M.T., Wang, C.-H., Huang, C.-Y., Wang, P., Wang, L., and Sarnthein, M., 1999. A late Quaternary planktonic foraminifer faunal record of rapid climatic changes from the South China Sea. *Mar. Geol.,* 156:85–108.

Clemens, S., 1999. An astronomical tuning strategy for Pliocene sections: implications for global-scale correlation and phase relationships. *Philos. Trans. R. Soc. London A, Math. Phys. Sci.,* 357:1949–1973.

Clemens, S.C., Murray, D.W., and Prell, W.L., 1996. Nonstationary phase of the Plio-Pleistocene Asian monsoon. *Science,* 274:943–948.

Clemens, S.C., and Prell, W.L., 1990. Late Pleistocene variability of Arabian Sea summer monsoon winds and continental aridity: eolian records from the lithogenic component of deep-sea sediments. *Paleoceanography,* 5:109–145.

————, 1991a. Late Quaternary forcing of Indian Ocean summer-monsoon winds: a comparison of Fourier model and general circulation model results. *J. Geophys. Res.,* 96:22683–22700.

————, 1991b. One million year record of summer monsoon winds and continental aridity from the Owen Ridge (Site 722), northwest Arabian Sea. *In* Prell, W.L., Niitsuma, N., et al., *Proc. ODP, Sci. Results,* 117: College Station, TX (Ocean Drilling Program), 365–388.

Clemens, S.C., Prell, W.L., Murray, D., Shimmield, G., and Weedon, G., 1991. Forcing mechanisms of the Indian Ocean monsoon. *Nature,* 353:720–725.

CLIMAP Project Members, 1981. Seasonal reconstructions of the Earth's surface at the last glacial maximum. *Geol. Soc. Am., Map and Chart Ser.,* MC36.

Cochran, J.R., 1990. Himalayan uplift, sea level, and the record of Bengal Fan sedimentation at the ODP Leg 116 Sites. *In* Cochran, J.R., Stow, D.A.V., et al., *Proc. ODP, Sci. Results,* 116: College Station, TX (Ocean Drilling Program), 397–414.

Colin, C., Kissel, C., Blamart, D., and Turpin, L., 1998. Magnetic properties of sediments in the Bay of Bengal and the Andaman Sea: impact of rapid North Atlantic

Ocean climatic events on the strength of the Indian monsoon. *Earth Planet. Sci. Lett.,* 160:623–635.

Copeland, P., Harrison, T.M., Kidd, W.S.F., Xu, R., and Zhang, Y., 1987. Rapid early Miocene acceleration of uplift in the Gangdese Belt, Xizung (southern Tibet) and its bearing on accommodation mechanisms of the India-Asia collision. *Earth Planet. Sci. Lett.,* 86:240–252.

Derry, L., and France-Lanord, C., 1997. Himalayan weathering and erosion fluxes: climate and tectonic controls. *In* Ruddiman, W.F. (Ed.), *Tectonic Uplift and Climate Change:* New York (Plenum), 289–312.

Ding, Y., 1994. *Monsoon Over China:* Dordrecht (Kluwer Academic Publ.).

Ding, Z.L., Sun, J.M., Yang, S.L., and Liu, T.S., 1998. Preliminary magnetostratigraphy of a thick eolian red-clay loess sequence at Lingtai, the Chinese Loess Plateau. *Geophys. Res. Lett.,* 25:1225–1228.

Farrell, J.W., Raffi, I., Janecek, T.R., Murray, D.W., Levitan, M., Dadey, K.A., Emeis, K.-C., Lyle, M., Flores, J.-A., and Hovan, S., 1995. Late Neogene sedimentation patterns in the eastern equatorial Pacific. *In* Pisias, N.G., Mayer, L.A., Janecek, T.R., Palmer-Julson, A., and van Andel, T.H. (Eds.), *Proc. ODP, Sci. Results,* 138: College Station, TX (Ocean Drilling Program), 717–756.

Fulthorpe, C.S., and Schlanger, S.O., 1989. Paleo-oceanographic and tectonic settings of early Miocene reefs and associated carbonates offshore Southeast Asia. *AAPG Bull.,* 73:729–756.

Gardner, J.V., Nelson, C.S., and Baker, P.A., 1986. Distribution and character of pale green laminae in sediment from Lord Howe Rise: a probable late Neogene and Quaternary tephrostratigraphic record. *In* Kennett, J.P., von der Borch, C.C., et al., *Init. Repts. DSDP,* 90 (Pt. 2): Washington (U.S. Govt. Printing Office), 1145–1159.

Harrison, T.M., Copeland, P., Kidd, W.S.F., and Yin, A., 1992. Raising Tibet. *Science,* 255:1663–1670.

Harrison, T.M, Yin, A., and Ryrson, F., 1998. Orographic evolution of the Himalaya and Tibetan Plateau. *In* Crowley, T.J., and Burke, K.C. (Eds.), *Tectonic Boundary Conditions for Climate Reconstructions.* Oxford Monogr. Geol. Geophys., 39:39–72.

Hastenrath, S., 1991. *Climate Dynamics of the Tropics:* Boston (Kluwer Academic Publ.).

Hastenrath, S., and Greischar, L., 1993. The monsoonal heat budget of the hydrosphere atmosphere system in the Indian Ocean sector. *J. Geophys. Res.,* 98:6869–6881.

Hayes, D.E., Nissen, S.S., Buhl, P., Diebold, J., Yao, B., Zeng, W., and Chen, Y., 1995. Throughgoing crustal faults along the northern margin of the South China Sea and their role in crustal extension. *J. Geophys. Res.,* 100:22435–22446.

Holloway, N.H., 1982. North Palawan Block, Philippines—its relation to the Asian mainland and role in evolution of South China Sea. *AAPG Bull.,* 66:1357–1383.

Huang, C.-Y., Wu, W.-Y., Chang, C.-P., Tsao, S., Yuan, P.B., Lin, C.-W., and Xia, K.-Y., 1997. Tectonic evolution of accretionary prism in the arc-continent collision terrane of Taiwan. *Tectonophysics,* 281:31–51.

Huang, L., 1997. Calcareous nannofossil biostratigraphy in the Pearl River Mouth Basin, South China Sea, and Neogene reticulofenestrid coccoliths size distribution pattern. *Mar. Micropaleontol.,* 32:31–57.

Jennerjahn, T.C., Liebezeit, G., Kempe, S., Xu, L.Q., Chen, W.B., and Wang, H.K., 1992.Particle flux in the northern South China Sea. *In* Jin, X., Hudrass, H.R., Pautot, G. (Eds.), *Marine Geology and Geophysics of the South China Sea:* Beijing (China Ocean Press), 228–235.

Jiang, Z., Lin, Z., Li, M., et al., 1994. *Tertiary in Petroliferous Regions of China, VIII. The North Continental Shelf Region of South China Sea:* Beijing (Petroleum Industry Press). (in Chinese)

Jin, Q. (Ed.), 1989. *Geology and Oil-gas Resources of the South China Sea:* Beijing (Geological Publishing House). (in Chinese)

Jin, X., 1992. Tectogenesis and origin of northern South China Sea. *In* Jin, X., Hudrass, H.R., and Pautot, G. (Eds.), *Marine Geology and Geophysics of the South China Sea:* Beijing (China Ocean Press), 1–9.

Kalnay, E., Kanamitsu, M., Kistler, R., Collins, W., Deaven, D., Gandin, L., Iredell, M., Saha, S., White, G., Woollen, J., Zhu, Y., Chelliah, M., Ebisuzaki, W., Higgins, W., Janowiak, J., Mo, K.C., Ropelewski, C., Wang, J., Leetmaa, A., Reynolds, R., Jenne, R., and Joseph, D., 1996. The NCEP/NCAR 40-year reanalysis project. *Bull. Am. Meteorol. Soc.,* 77:437–471.

Kennett, J.P. (Ed.), 1985. *The Miocene Ocean: Paleoceanography and Biogeography.* Mem.—Geol. Soc. Am., 163.

Kump, L., and Arthur, M., 1997. Global chemical erosion during the Cenozoic: weatherability balances the budgets. *In* Ruddiman, W.F. (Ed.), *Tectonic Uplift and Climate Change:* New York (Plenum), 172–203.

Laskar, J., Joutel, F., and Boudin, F., 1993. Orbital, precessional, and insolation quantities for the Earth from –20 Myr to +10 Myr. *Astron. Astrophys.,* 270:522–533.

Lau, K.-M., and Yang., S., 1997. Climatology and interannual variability of the Southeast Asian summer monsoon. *Adv. Atmospheric Sci.,* 14:141–162.

Lee, T.-Y., and Lawver, L.A., 1994. Cenozoic plate reconstruction of the South China Sea region. *Tectonophysics,* 235:149–180.

Li, J., 1991. The environmental effects of the uplift of the Qinghai Xizang Plateau. *Quat. Sci. Rev.,* 10:479–483.

Li, J., Fan, X., Ma, H., Zhu, Z., Pan, B., and Chen, H., 1996. Late Cenozoic geomorphological evolution of upper reach of Yellow River and uplift of Tibetan Plateau. *Sci. China,* D26:316–322. (in Chinese)

Li, Y., Sun, X., and Wang, D., 1984. *The Tertiary of China:* Beijing (Geological Publ. House). (in Chinese)

Lind, I.L., Janecek, T.R., Krissek, L.A., Prentice, M.L., and Stax, R., 1993. Color bands in Ontong Java Plateau carbonate oozes and chalks. *In* Berger, W.H., Kroenke, L.W., Mayer, L.A., et al., *Proc. ODP, Sci. Results,* 130: College Station, TX (Ocean Drilling Program), 453–470.

Liu, T., and Ding, M., 1982. Pleistocene stratigraphy and Plio/Pleistocene boundary in China. *In Quaternary Geology and Environment of China:* Beijing (China Ocean Press).

Liu, T., and Ding, Z., 1993. Stepwise coupling of monsoon circulations to global ice volume variations during the late Cenozoic. *Global Planet. Change,* 7:119–130.

Ludmann, T., and Wong, H.K., 1999. Neotectonic regime on the passive continental margin of the northern South China Sea. *Tectonophysics,* 311:113–138.

Miao, Q., Thunell, R.C., and Anderson, D.M., 1994. Glacial-Holocene carbonate dissolution and sea surface temperatures in the South China and Sulu seas. *Paleoceanography,* 9:269–290.

Molnar, P., England, P., and Martinod, J., 1993. Mantle dynamics, uplift of the Tibetan Plateau, and the Indian monsoon. *Rev. Geophys.,* 31:357–396.

Morley, J.J., and Heusser, L.E., 1997. Role of orbital forcing in East Asian monsoon climates during the last 350 kyr: evidence from terrestrial and marine climate proxies from core RC14-99. *Paleoceanography,* 12:483–494.

Murakami, T., 1987. Orography and monsoons. *In* Fien, J., and Stephens, P. (Eds.), *Monsoons:* New York (Wiley), 331–364.

Murphy, M.A., Yin, A., Harrison, T.M., Durr, S.B., Kidd, W.S.F., Chen, Z., Ryerson, F.J., Wang, X., and Zhou, X., 1997. Significant crustal shortening in south-central Tibet prior to the Indo-Asian collision. *Geology,* 25:713–722.

Ninkovich, D., and Donn, W.L., 1976. Explosive Cenozoic volcanism and climatic interpretations. *Science,* 194:899–906.

Nissen, S.S., Hayes, D.E., Buhl, P., Diebold, J., Yao, B., Zeng, W., and Chen, Y., 1995. Deep penetration seismic soundings across the northern margin of the South China Sea. *J. Geophys. Res.,* 100:22407–22433.

Packham, G., 1996. Cenozoic SE Asia: reconstructing its aggregation and reorganization. *In* Hall, R., and Blundell, D. (Eds.), *Tectonic Evolution of Southeast Asia*. Geol. Soc. Spec. Publ. London, 106:123–152.

Pflaumann, U., and Jian, Z., 1999. Modern distribution patterns of planktonic foraminifera in the South China Sea and western Pacific: a new transfer technique to estimate regional sea-surface temperatures. *Mar. Geol.,* 156:41–83.

Prell, W.L., 1984a. Monsoonal climate of the Arabian Sea during the late Quaternary: a response to changing solar radiation. *In* Berger, A.L., Imbrie, J., Hays, J., Kukla, G., and Saltzman, B. (Eds.). *Milankovitch and Climate* (Pt. 1): Dordrecht (D. Reidel), 349–366.

————, 1984b. Variation of monsoonal upwelling: a response to changing solar radiation. *In* Hansen, J.E., and Takahashi, T. (Eds.), *Climatic Processes and Climate Sensitivity.* Geophys. Monogr., Am. Geophys. Union, Maurice Ewing Ser., 29:48–57.

Prell, W.L., and Kutzbach, J.E., 1987. Monsoon variability over the past 150,000 years. *J. Geophys. Res.,* 92:8411–8425.

————, 1992. Sensitivity of the Indian monsoon to forcing parameters and implications for its evolution. *Nature,* 360:647–652.

————, 1997. The impact of Tibet-Himalayan elevation on the sensitivity of the monsoon climate system to changes in solar radiation. *In* Ruddiman, W.F. (Ed.), *Tectonic Uplift and Climate Change:* New York (Plenum), 172–203.

Prell, W.L., Murray, D.W., Clemens, S.C., and Anderson, D.M., 1992. Evolution and variability of the Indian Ocean summer monsoon: evidence from the western Arabian Sea drilling program. *In* Duncan, R.A. (Ed.), *The Indian Ocean: A Synthesis of Results from the Ocean Drilling Program*. Am. Geophys. Union, 70:447–469.

Prell, W.L., Niitsuma, N., et al., 1991. *Proc. ODP, Sci. Results,* 117: College Station, TX (Ocean Drilling Program).

Quade, J., Cerling, T.E., and Bowman, J.R., 1989. Development of Asian monsoon revealed by marked ecological shift during the latest Miocene in northern Pakistan. *Nature,* 342:163–166.

Ramstein, G., Fluteau, F., Besse, J., and Joussaume, S., 1997. Effect of orogeny, plate motion and land-sea distribution on Euroasian climate change over the past 30 million years. *Nature,* 386:788–795.

Rangin, C., Silver, E.A., von Breymann, M.T., et al., 1990. *Proc. ODP, Init. Repts.,* 124: College Station, TX (Ocean Drilling Program).

Raymo, M.E., 1994. The Himalayas, organic carbon burial, and climate in the Miocene. *Paleoceanography,* 9:399–404.

Raymo, M.E., Ruddiman, W.F., and Froelich, P.N., 1988. Influence of late Cenozoic mountain building on ocean geochemical cycles. *Geology,* 16:649–653.

Rea, D.K., 1992. Delivery of Himalayan sediment to the northern Indian Ocean and its relation to global climate, sea level, uplift, and seawater strontium. *In* Duncan, R.A., Rea, D.K., Kidd, R.B., von Rad, U., and Weissel, J.K. (Eds.), *Synthesis of Results from Scientific Drilling in the Indian Ocean*. Geophys. Monogr., Am. Geophys. Union, 70:387–402.

Ru, K., Zhou, D., and Chen, H., 1994. Basin evolution and hydrocarbon potential of the northern South China Sea. *In* Zhou, D., Liang, Y., and Zeng, C. (Eds.), *Oceanology of China Seas:* New York (Kluwer Press), 2:361–372.

Ruddiman, W.F. (Ed.), 1997. *Tectonic Uplift and Climate Change:* New York (Plenum).

Ruddiman, W.F., and Kutzbach, J.E., 1989. Forcing of late Cenozoic northern hemisphere climate by plateau uplift in southern Asia and the American West. *J. Geophys. Res.,* 94:18409–18427.

Sarnthein, M., Pflaumann, U., Wang, P.X., and Wong, H.K. (Eds.), 1994. Preliminary Report on Sonne-95 Cruise "Monitor Monsoon" to the South China Sea. *Rep. Geol.-Palaontol. Inst. Univ. Kiel.,* 68.

Sarnthein, M., and Wang, P.X., 1999. Response of West Pacific marginal seas to global climatic change. *Mar. Geol.,* 156:1–3.

Schärer, U., Tapponnier, P., Lacassin, R., Leloup, P.H., Zhong, D., and Ji, S., 1990. Intraplate tectonics in Asia: a precise age for large-scale Miocene movement along the Ailao Shan-Red River shear zone, China. *Earth Planet. Sci. Lett.,* 97:65–77.

Schultz, H., Van Rad, U., and Erlenkeuser, H., 1998. Correlation between Arabian Sea and Greenland climate oscillations of the past 110,000 years. *Nature,* 393:54–57.

Sirocko, F., Sarnthein, M., Erlenkeuser, H., Lange, H., Arnold, M., and Duplessy, J.C., 1993. Century-scale events in monsoonal climate over the past 24,000 years. *Nature,* 364:322–324.

Stuijts, I., Newsome, J.C., and Flenley, J.R., 1988. Evidence for late Quaternary vegetational change in the Sumatran and Javan highlands. *Rev. Palaeobot. Palynol.,* 55:207–216.

Su, D., White, N., and McKenzie, D., 1989. Extension and subsidence of the Pearl River Mouth Basin, northern South China Sea. *Basin Res.,* 2:205–222.

Su, G., and Wang, T., 1994. Basic characteristics of modern sedimentation in South China Sea. *In* Zhou, D., Liang, Y.-B., and Zeng, C.-K. (Eds.), *Oceanology of China Seas:* New York (Kluwer), 2:407–418.

Sun, X., 1996. Environmental changes of the northern South China Sea since the last 30 k.y. based on pollen data of deep sea Core 17940-2. *IGC-30,* 2:254. (Abstract)

Sun, X., and Li, X., 1999. A pollen record of the last 37 ka in deep sea core 17940 from the northern slope of the South China Sea. *Mar. Geol.,* 156:227–242.

Tamaki, K., and Honza, E., 1991. Global tectonics and formation of marginal basins: role of the western Pacific. *Episodes,* 14:224–230.

Taylor, B., and Hayes, D.E., 1980. The tectonic evolution of the South China Basin. *In* Hayes, D.E. (Ed.), *Tectonic and Geologic Evolution of Southeast Asian Seas and Islands*. Geophys. Monogr., Am. Geophys. Union, 23:89–104.

————, 1983. Origin and history of the South China Sea Basin. *In* Hayes, D.E. (Ed.), *Tectonic and Geologic Evolution of Southeast Asian Seas and Islands* (Pt. 2). Geophys. Monogr., Am. Geophys. Union, 27:23–56.

Thunell, R.C., Miao, Q., Calvert, S.E., and Pedersen, T.F., 1992. Glacial-Holocene biogenic sedimentation patterns in the South China Sea: productivity variations and surface water CO_2. *Paleoceanography,* 7:143–162.

Wang, C., 1996. Sequence stratigraphic analysis of marine Miocene formations in the Pearl River Mouth Basin and its significance. *China Offshore Oil and Gas (Geology),* 10:279–288. (in Chinese, with English abstract)

Wang, L., Sarnthein, M., Erlenkeuser, H., Grimalt, J., Grootes, P., Heilig, S., Ivanova, E., Kienast, M., Pelejero, C., and Pflaumann, U., 1999. East Asian monsoon climate during the late Pleistocene: high-resolution sediment records from the South China Sea. *Mar. Geol.,* 156:245–284.

Wang, L., and Wang, P., 1990. Late Quaternary paleoceanography of the South China Sea: glacial interglacial contrasts in an enclosed basin. *Paleoceanography,* 5:77–90.

Wang, P., 1990. Neogene stratigraphy and paleoenvironments of China. *Palaeogeogr., Palaeoclimatol., Palaeoecol.,* 77:315–334.

————, 1997. Late Cenozoic environment evolution in China: marine factors and records. *Proc. 4th Int. Conf. Evolution of the East Asian Environment,* 264–274.

————, 1999. Response of Western Pacific marginal seas to glacial cycles: paleoceanographic and sedimentological features. *Mar. Geol.,* 156:5–39.

Wang, P., Bradshaw, M., Ganzei, S.S., Tsukawaki, S., Hanssan, K.B., Hantoro, W.S., Poobrasert, S., Burne, R., Zhao, Q., and Kagami, H., 1997. West Pacific marginal seas during last glacial maximum: amplification of environmental signals and its impact on monsoon climate. *Proc. 30th Int. Geol. Congr.,* 13:65–85.

Wang, P., Wang, L., Bian, Y., and Jian, Z., 1995. Late Quaternary paleoceanography of the South China Sea: surface circulation and carbonate cycles. *Mar. Geol.,* 127:145–165.

Webster, P.J., 1987. The elementary monsoon. *In* Fein, J.S., and Stephens, P.L. (Eds.), *Monsoons:* New York (Wiley), 3–32.

————, 1994. The role of hydrological processes in ocean-atmosphere interactions. *Rev. Geophys.,* 32:427–476.

Webster, P.J., Magana, V.O., Palmer, T.N., Shukla, J., Tomas, R.A., Yanai, M., and Yasunari, T., 1998. Monsoons: processes, predictability, and the prospects for prediction, in the TOGA decade. *J. Geophys. Res.,* 103:14451–14510.

Wiesner, M.G., Zheng, L., Wong, H.K., Wang, Y., and Chen, W., 1996. Flux of particulate matter in the South China Sea. *In* Ittikot, V., Schäfer, P., Honjo, S., and Depetris, P.J. (Eds.), *Particle Flux in the Ocean:* New York (Wiley), 293–312.

Wu, J., 1994. Evaluation and models of Cenozoic sedimentation in the South China Sea. *Tectonophysics,* 235:77–98.

Ye, D., Zhong, X., and Yao, Y., 1993. *Tertiary in Petroliferous Regions of China* (Vol. I): *Introduction:* Beijing (Petroleum Industry Press). (in Chinese)

Zheng, L., Ke, J., Winn, K., and Stoffers, P., 1993. Carbonate sedimentation cycles in the northern South China Sea during the late Quaternary. *In* Zheng, L., and Chen, W. (Eds.), *Contributions to Sedimentation Process and Geochemistry of the South China Sea:* Beijing (China Ocean Press), 109–123. (in Chinese, with English abstract)

Zhou, T., 1984. *Cenozoic Paleogeography* (Vol. I): Beijing (Science Press). (in Chinese)

Figure F1. Climatology of the July and January monsoon circulation. **A, B.** Locations of ODP Legs 184 (northern and southern South China Sea) and 117 (Arabian Sea) are shown as open rectangles. Sea-level pressure and surface winds are shown by arrows; longer arrows indicate stronger winds. The strongest winds (B; northern Arabian Sea) are ~15 m/s. **C, D.** Precipitation is indicated by contours (6 mm/day) and hatching (>9 mm/day). The pressure gradients and resulting winds and precipitation patterns reflect land-sea heating contrasts, which are functions of solar radiation, elevation, and land-surface boundary conditions. Monthly data for 1990–1997 from the National Oceanic and Atmospheric Administration, National Centers for Environmental Prediction/National Center for Atmospheric Research, Climate Data Assimilation System-1 (NOAA NCEP-NCAR CDAS-1) (Kalnay et al., 1996).

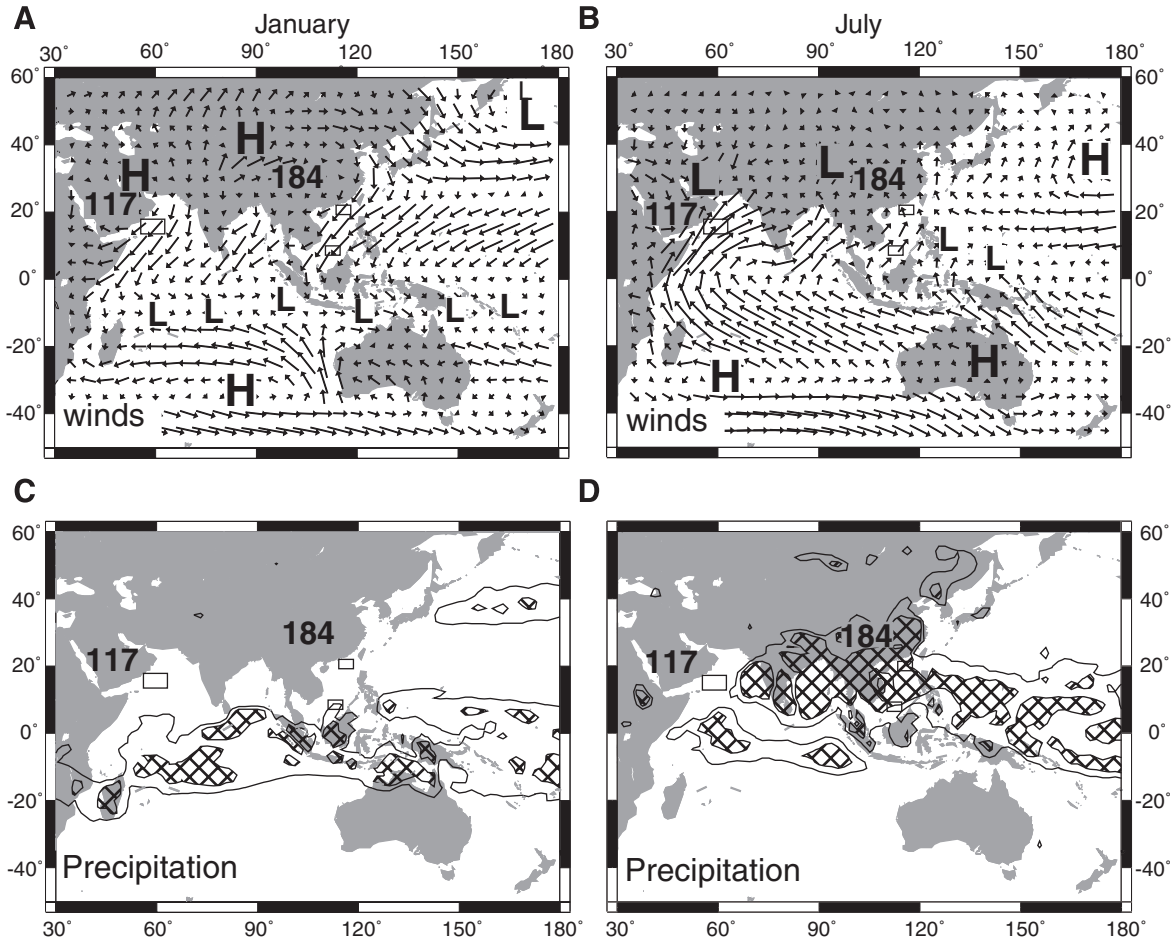

Figure F2. Map of the South China Sea showing locations of Leg 184 drilling areas. BS = Bashi Strait, SCS = South China Sea.

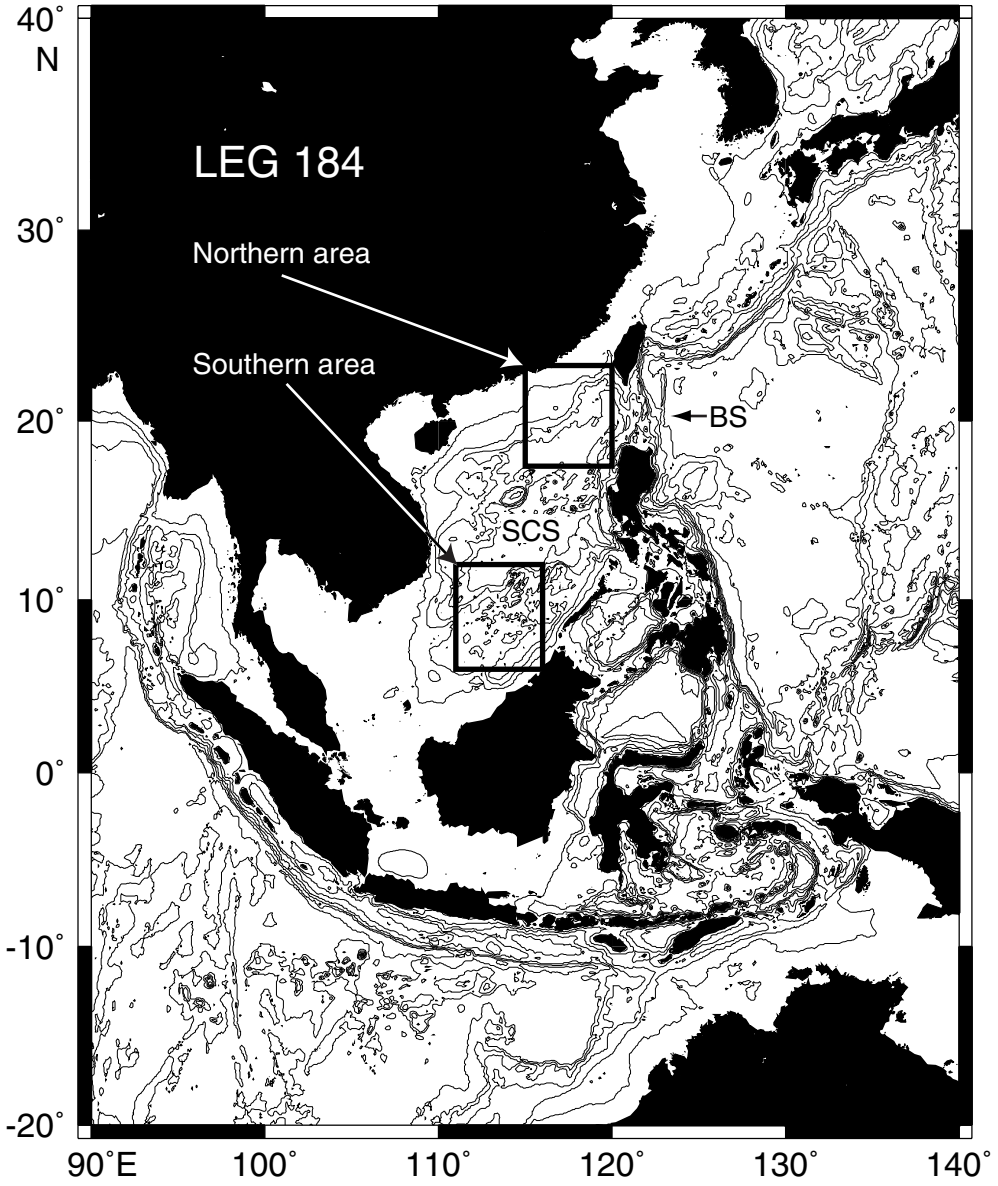

Figure F3. Tectonic setting of the South China Sea. **A.** Major tectonic elements of the northern and central parts of the South China Sea. Thick dotted line outlines the Central Basin with selected magnetic anomaly lineaments. Thin dotted and solid lines are isobaths of 200 and 2000 m (Hayes et al., 1995). Large box corresponds to this figure. **B.** Geological framework of the northern margin of the South China Sea (Ru et al., 1994). YGHB = Yinggehai Basin, QDNB = Qiongdongnan Basin, BBWB = Baibiwan Basin, PRMB = Pearl River Mouth Basin, SWTB = Southwest Taiwan Basin. Leg 184 sites are located south of Dongsha Island on the continental margin between the Pearl River Mouth Basin and the South China Sea Basin.

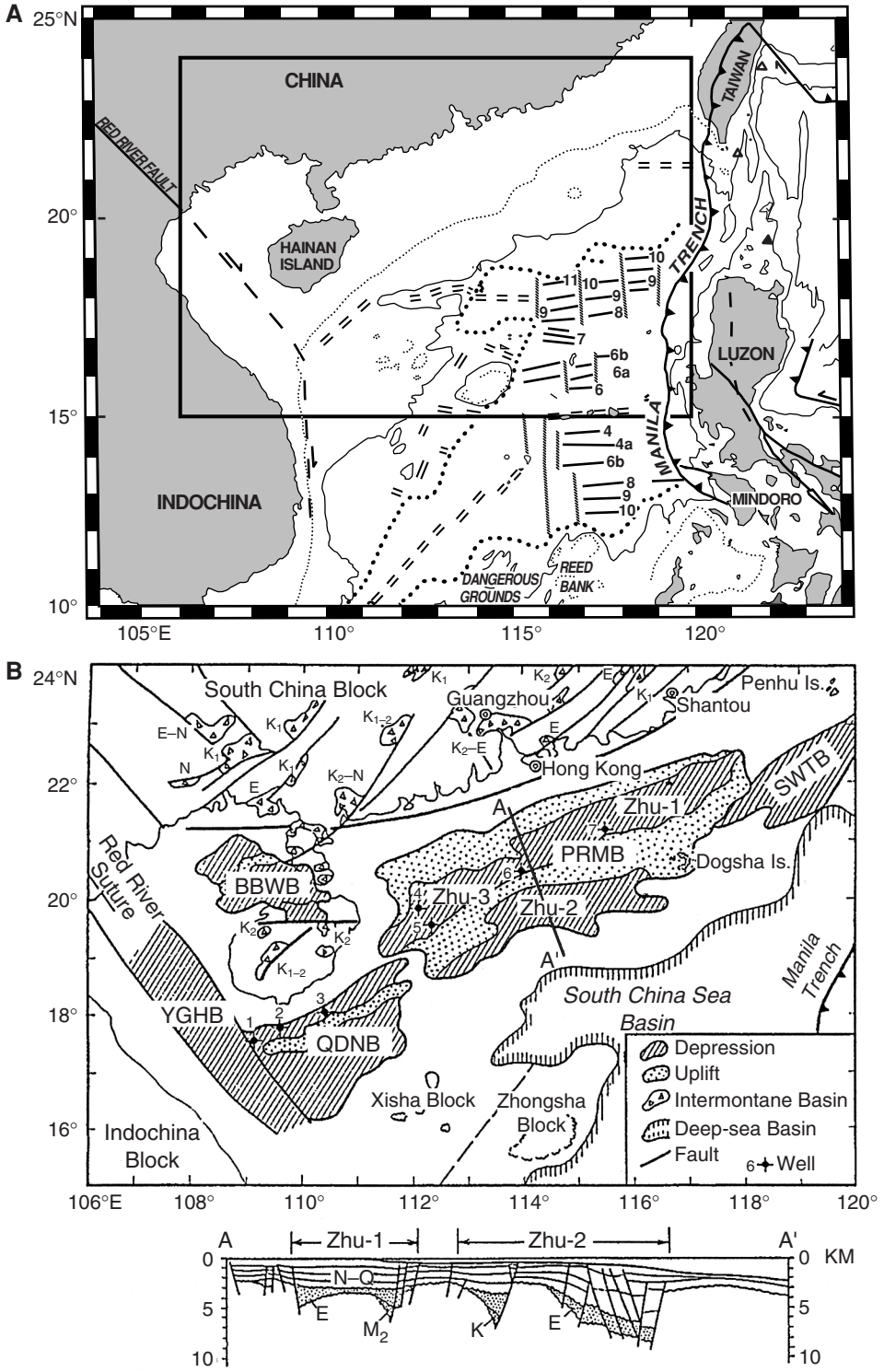

Figure F4. Marine and terrestrial observations indicating an intensification of the monsoon in the late Miocene (10–8 Ma) and a model simulation of a possible evolution of monsoon runoff. **A.** Abundance of planktonic foraminifer *Globigerina bulloides* and radiolarian *Actinoma* spp. that indicate active upwelling induced by southwest monsoonal winds (from ODP Site 722, Arabian Sea). **B.** Oxygen and carbon isotopes measured in pedogenic carbonates from Pakistan indicating more seasonal climates and a decrease in atmospheric CO_2, possibly from monsoon-related weathering (data from Quade et al., 1989). Open circles = $\delta^{13}C$ (‰), solid squares = $\delta^{18}O$ (‰). **C.** Normalized, mean terrigenous sediment flux to the northern Indian Ocean that suggests active uplift and fluvial deposition in the late Miocene (from Rea, 1992). **D.** A model simulation of monsoon runoff, relative to control simulation, using the Molnar model for uplift history (11–8 Ma) and the coupled effects of elevation change and orbitally induced solar radiation changes.

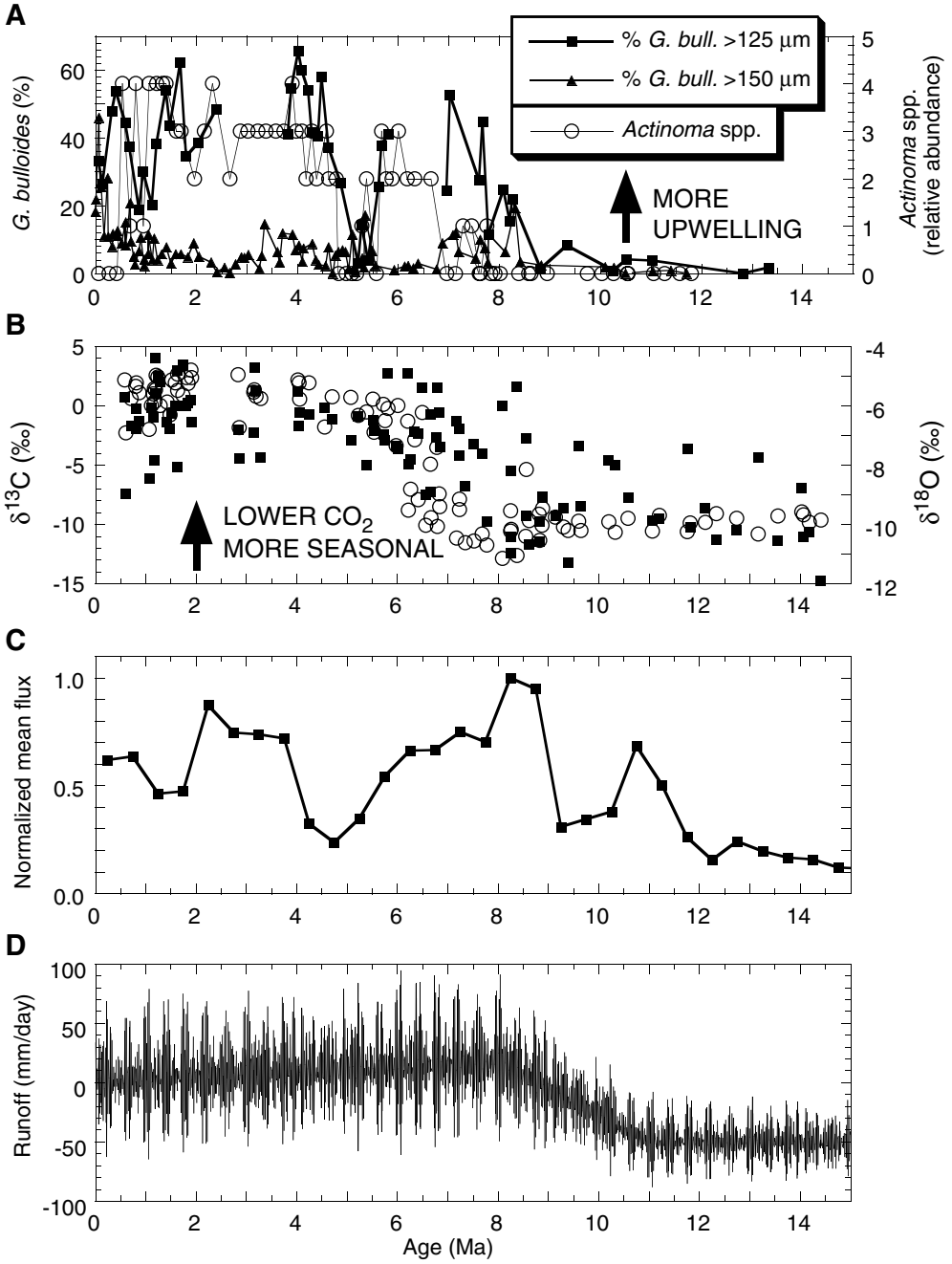

Figure F5. Summary of monsoonal stages defined from land-based studies in China, after Wang (1997), Wang (1990), and Liu and Ding (1982). SCS = South China Sea.

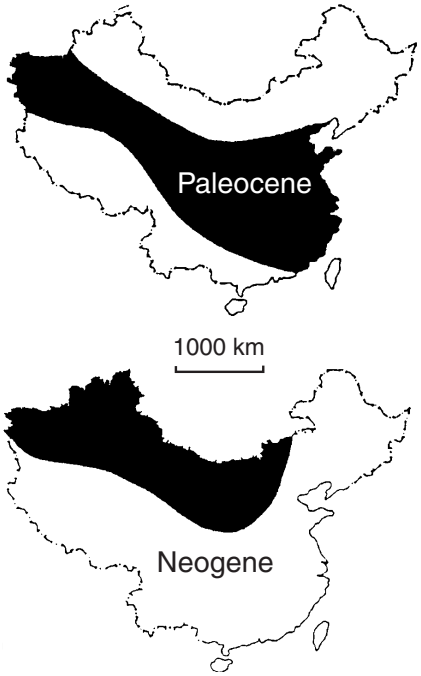

Stage		Time interval	Monsoon	Paleogeography
Premonsoon		Paleocene early Eocene	Absent or insignificant	Smaller Asia without Tibetan Plateau
	~50 Ma			
Transitional		middle Eocene Oligocene	Unstable	India joined with Asia
	~20 Ma			
Monsoon I		Miocene Pliocene	Summer monsoon	Plateau uplift started; SCS opened
	~2.4 Ma			
Monsoon II		late Pliocene Pleistocene	Summer and winter monsoon (loess deposits)	Intensive plateau uplift

Figure F6. A composite stratigraphy from industrial wells in the eastern part of the Pearl River Mouth Basin, which lies on the shelf and uppermost continental slope northwest of the northern sites (see PRMB in Fig. F3, p. 47, for bathymetry). These wells provide the seismic reflector sequence and general age structure to be correlated with the more marine ODP sites on the slope. Note the nonmarine sequence beginning from the upper Oligocene (modified from Jiang et al., 1994).

Period	Epoch		Formation	Thickness (m)	Lithology	Seismic reflector	Fossil Zone: Foram.	Fossil Zone: Nanno.	Description
Quat.	Pleist.			55.8~444			N23 | N22	NN21 | NN19	Marine gray-grayish muds with fine sands, intercalated with nonmarine muds, sands, and partly sandy gravel in upper part
						T_N			
Neog.	Plio.		Wanshan	0~541			N21 | N18	NN18 | NN12	Marine gray-grayish green mudstone with thin siltsone
						T_1			
	Mio.	u	Yuehai	55.8~677.5			N17 | N16	NN11 | NN10	Marine grayish green mudstone, gray siltstone with nonmarine thick-bedded sandstone
						T_2			
		m	Hanjiang	306~1153.5			N15 | N9	NN9 | NN5	Alternation of nonmarine grayish green mudstone, gray siltstone, sandstone with marine grayish mudstone and siltstone
						T_4			
		1	Zhujiang	270~1022			N8 | N4B	NN4 | NN1 (upper)	Upper part: marine mudstone, siltstone, and reef limestone Middle part: alternations of marine grayish mudstone, limestone and alluvial sandstone, and mudstone Lower part: alluvial sandstone and mudstone with local tuff lenses
						T_6			
Paleog.	Oligo.	u	Zhuhai	0~875			N4A | P22	NN1 (lower) | NP24	Alluvial sandstone and mudstone with thin marine facies interbeds, replaced by marine sandstone and mudstone southward
						T_7			
		1	Enping	0~111.5					Upper part: nonmarine dark gray mudstone, gray sandstone and thin coal seams, with marine interbeds in the southmost part of the basin containing nannofossils of NP24/23 Lower part: nonmarine thick sandstone and thin dark shale
	Eoc.	u							Upper part: lacustrine and alluvial gray, grayish brown mudstone and sandstone, with a thin marine mudstone in the northeast part of the basin containing NP15 nannofossils Lower part: arkos conglomerate, sandstone and muddy sandstone with thin shale and coal beds
		m	Wenchan	0~432					
						T_8			
		1	Shenhu	0~958		T_9			Light gray tuff with quartz porphyry and thin mudstone intercalations, covered by a layer of felsophyre. In some part of the basin, alternating sandstone and mudstones
	Paleoc.								
						T_g			
Mesozoic									Late Mesozoic granites, partly metamorphic or effusive rocks

Figure F7. East Asian monsoon climate change in the northern SCS during the last glacial cycle from a core recovered during the SONNE95-17940 cruise. The plots shown are, from top to bottom: total grain-size mode, clay content, stable oxygen isotope values from *Globigerinoides ruber,* and, for reference, the oxygen isotope record from the GISP2 ice core. EHPB = early Holocene/Preboreal, Y.D. = Younger Dryas, B/A = Boelling/Alleroed, H1–H4 = Heinrich Events 1–4, O.D. = Oldest Dryas, LGM = last glacial maximum. Data from Wang et al. (1999).

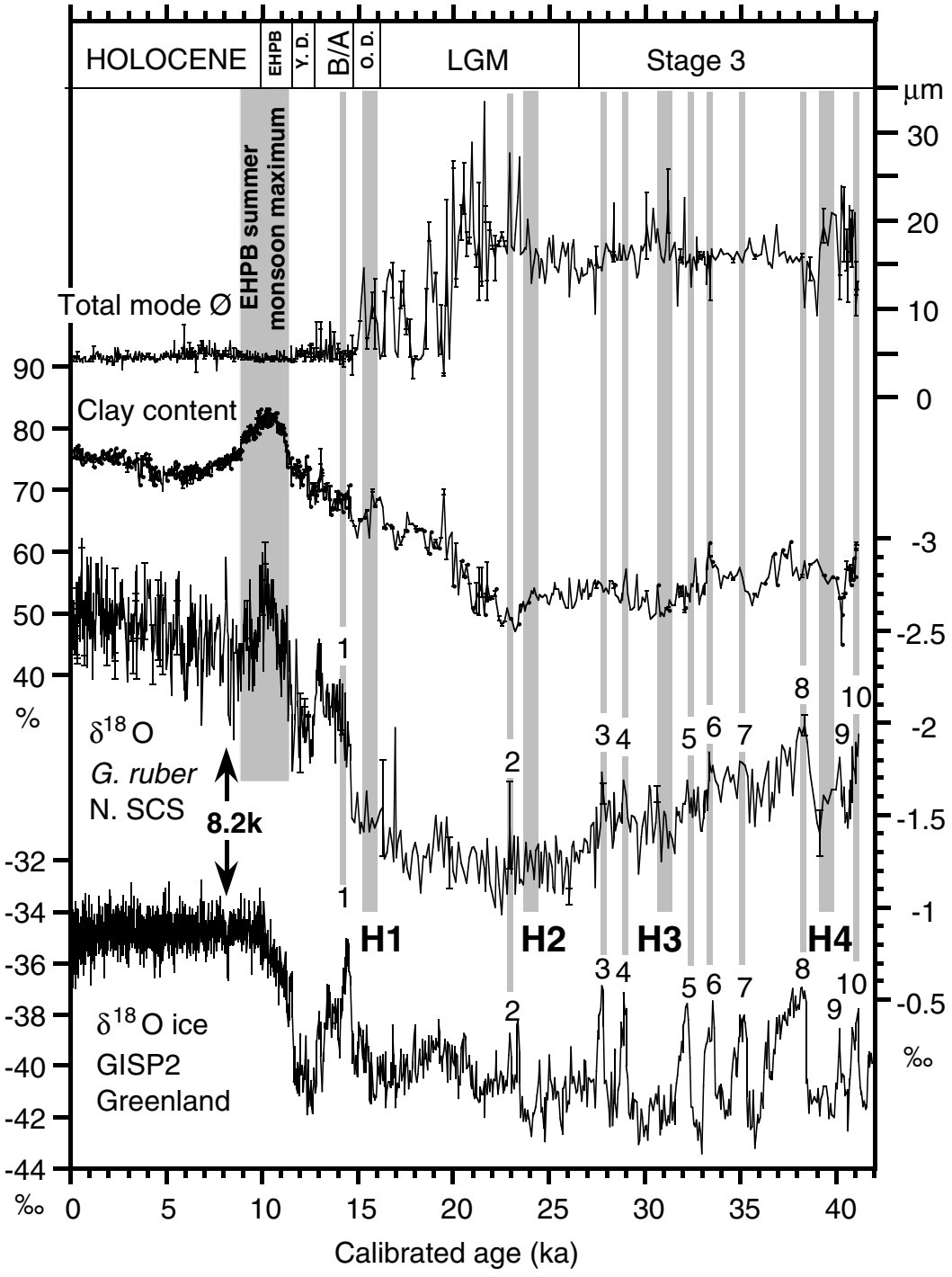

Figure F8. Site location map for the southern South China Sea Site 1143. The irregular seafloor bathymetry reflects both the highly irregular bathymetry and the low abundance of survey data in the Spratly Islands or Nansha Islands (Dangerous Grounds) area.

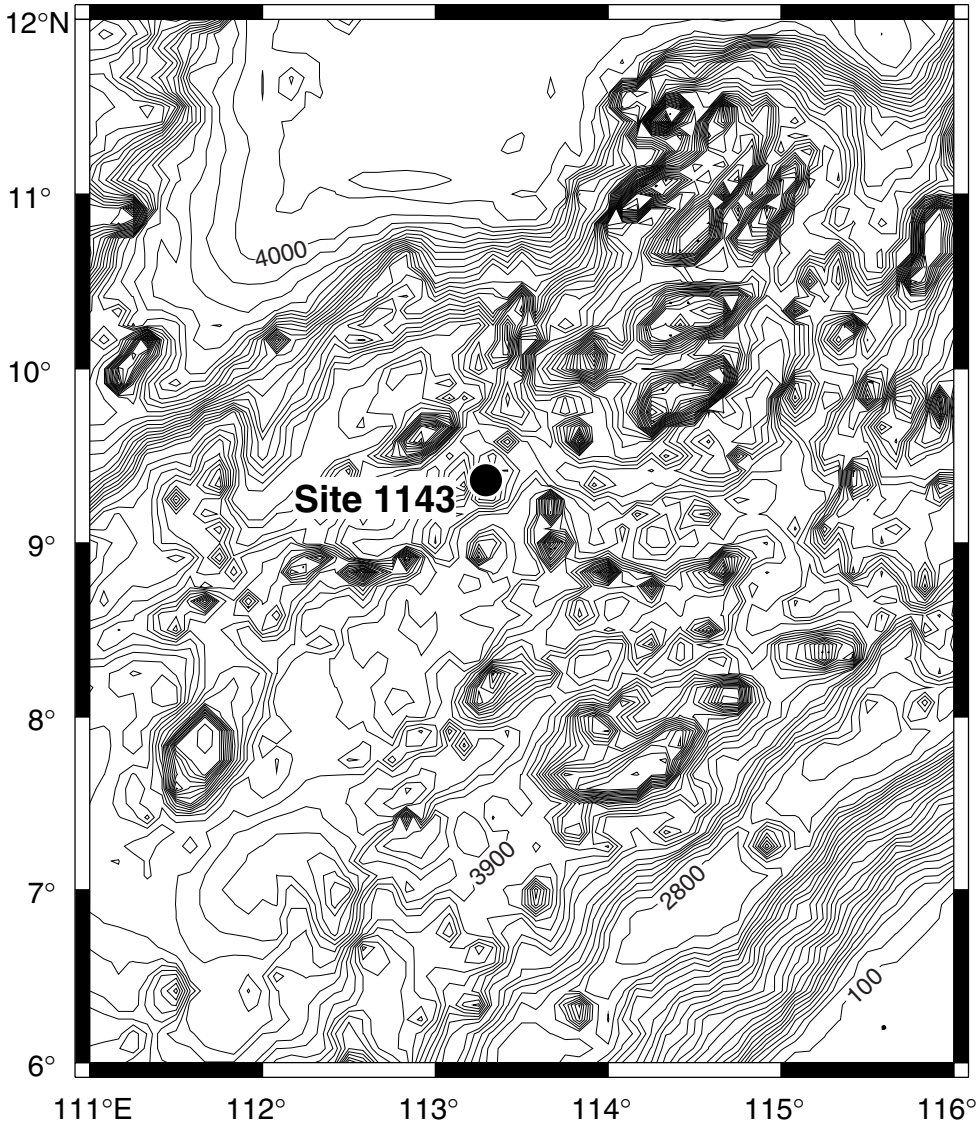

Figure F9. Site location map for the northern South China Sea Sites 1144–1148.

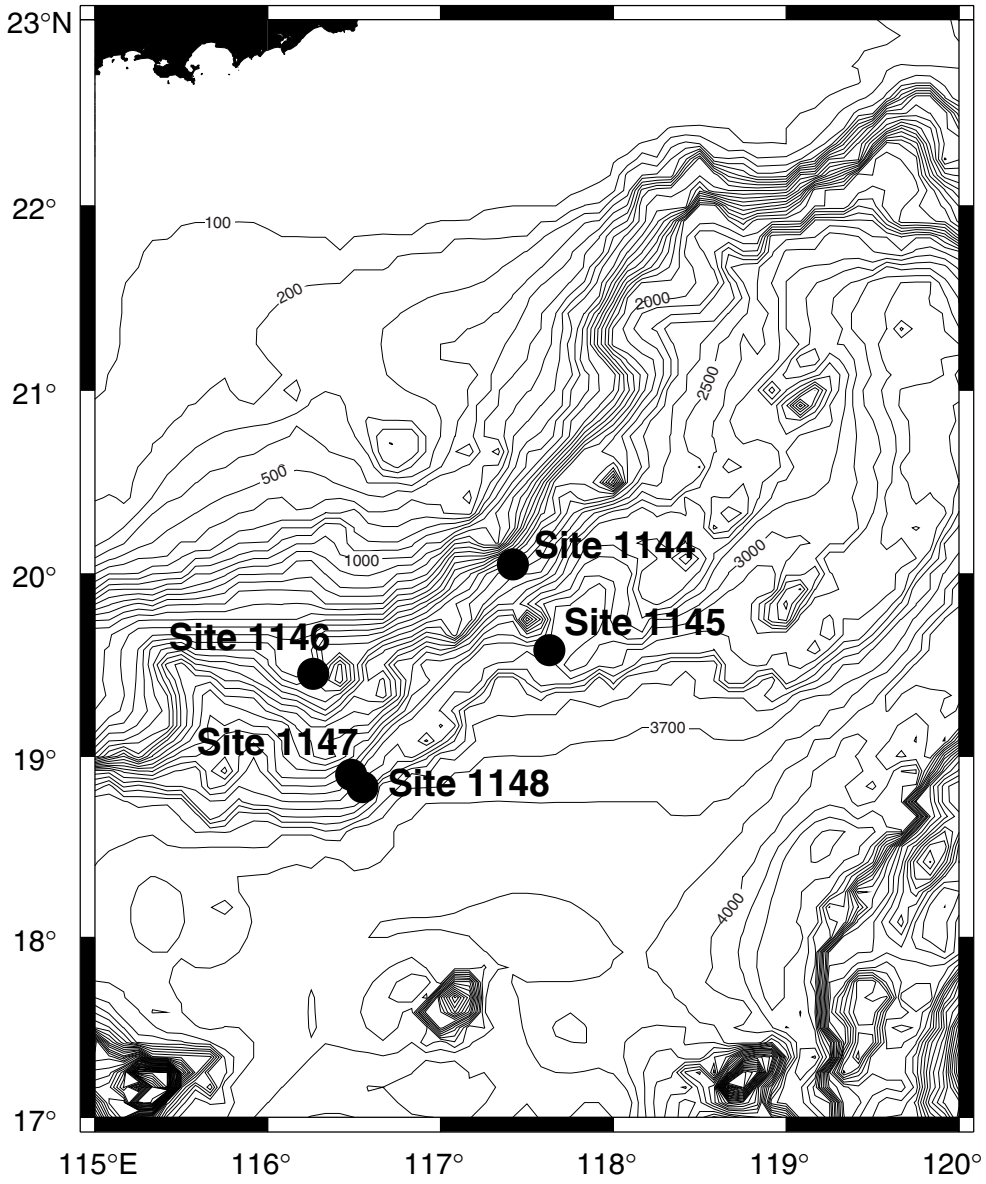

Figure F10. Precruise seismic line across Site 1143. Line NS95-240, common depth point (CDP) 3617. Water depth = 2772 m. Penetration depth = 500 mbsf (graphic presentation is approximate). TWT = two-way traveltime.

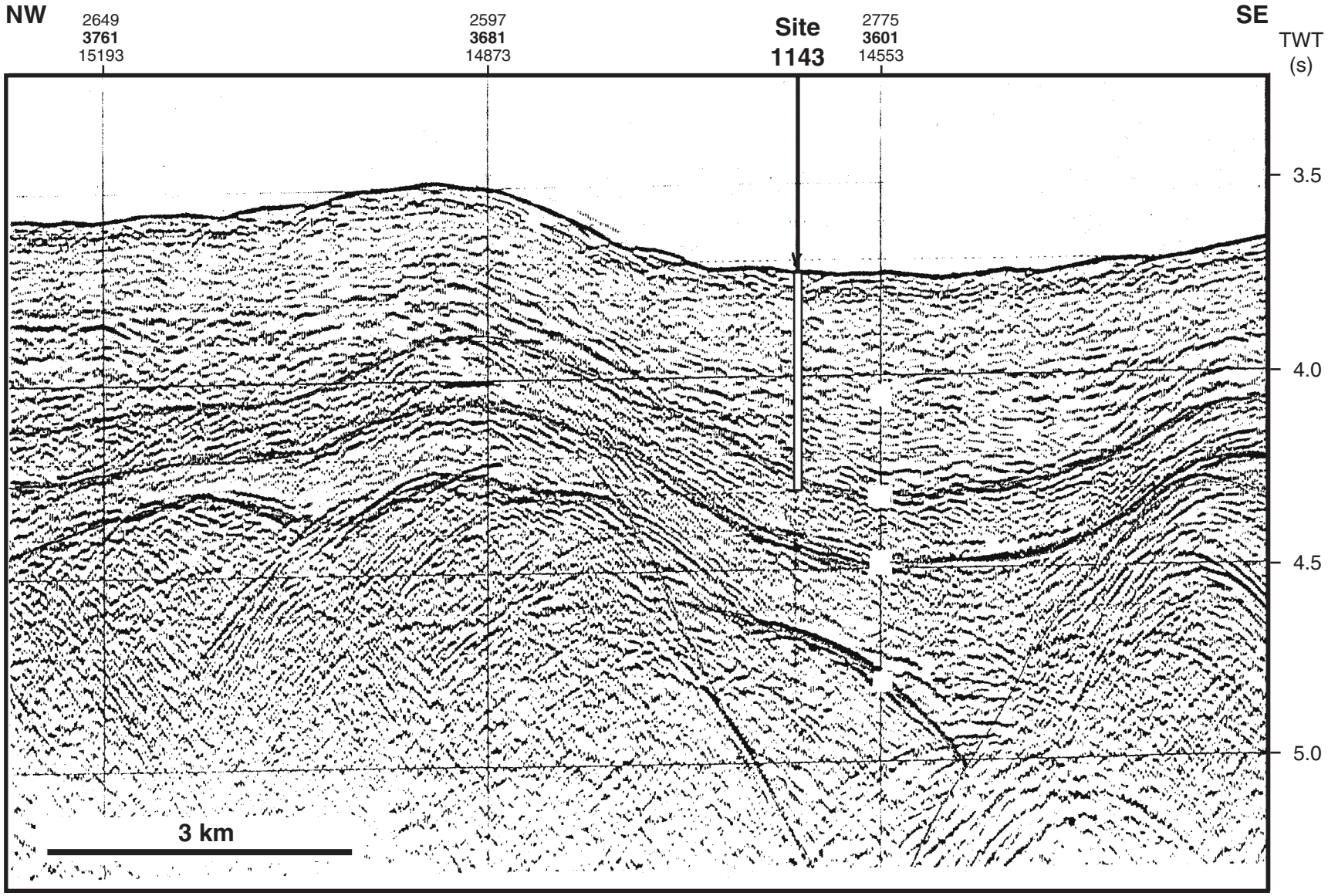

Figure F11. Summary diagram of coring results at Site 1143 on the mcd scale. Maximum penetration measured with the drill pipe is 500 mbsf. The core recovery column is a graphic presentation of the cored and recovered intervals for each hole. Larger gaps are the result of coring problems (<100% nominal recovery); smaller gaps (typically 0.5–2.0 m), revealed by hole-to-hole correlation, occur even when nominal core recovery is 100% or more. The graphic lithology column presents the major sediment types: horizontal line patterns are clay; diagonal dashed patterns are nannofossil ooze with foraminifers. Lithologic units are also shown. Mass accumulation rates (MARs) were calculated for total sediment (light gray histograms) and carbonate only (darker gray, solid histograms) from 5-m interval sampling of the smoothed depth-age model, dry density, and carbonate concentration. LSR and MAR estimates are also displayed in Fig. **F26,** p. 71, and the data are available as Microsoft Excel data files in the **"Supplementary Materials"** contents list. The smoothed depth-age curve (line) is overlain with control points from nannofossil (squares) and foraminifer (circles) biostratigraphy and magnetostratigraphy (crosses [shown for other sites]). The color reflectance lightness (L*) parameter (solid line) was measured every 2–4 cm and smoothed with a 20-point moving average for this figure. Carbonate concentration, expressed as percent calcite (dots with dashed line), was measured every ~3.5 m. Magnetic susceptibility (thicker line) and natural gamma radiation (thinner line) were measured every 2–5 cm, and the records presented here are smoothed with a 20-point moving average. Porosity (solid line) and grain density (dots with dashed line) were calculated from moisture and density (MAD) measurements on samples taken every 1.5–3.0 m. Bulk density (solid line) and dry density (dots with dashed line) were calculated from MAD measurements on samples taken every 1.5–3.0 m. (**Figure shown on next page.**)

Figure F11. (Caption on previous page.)

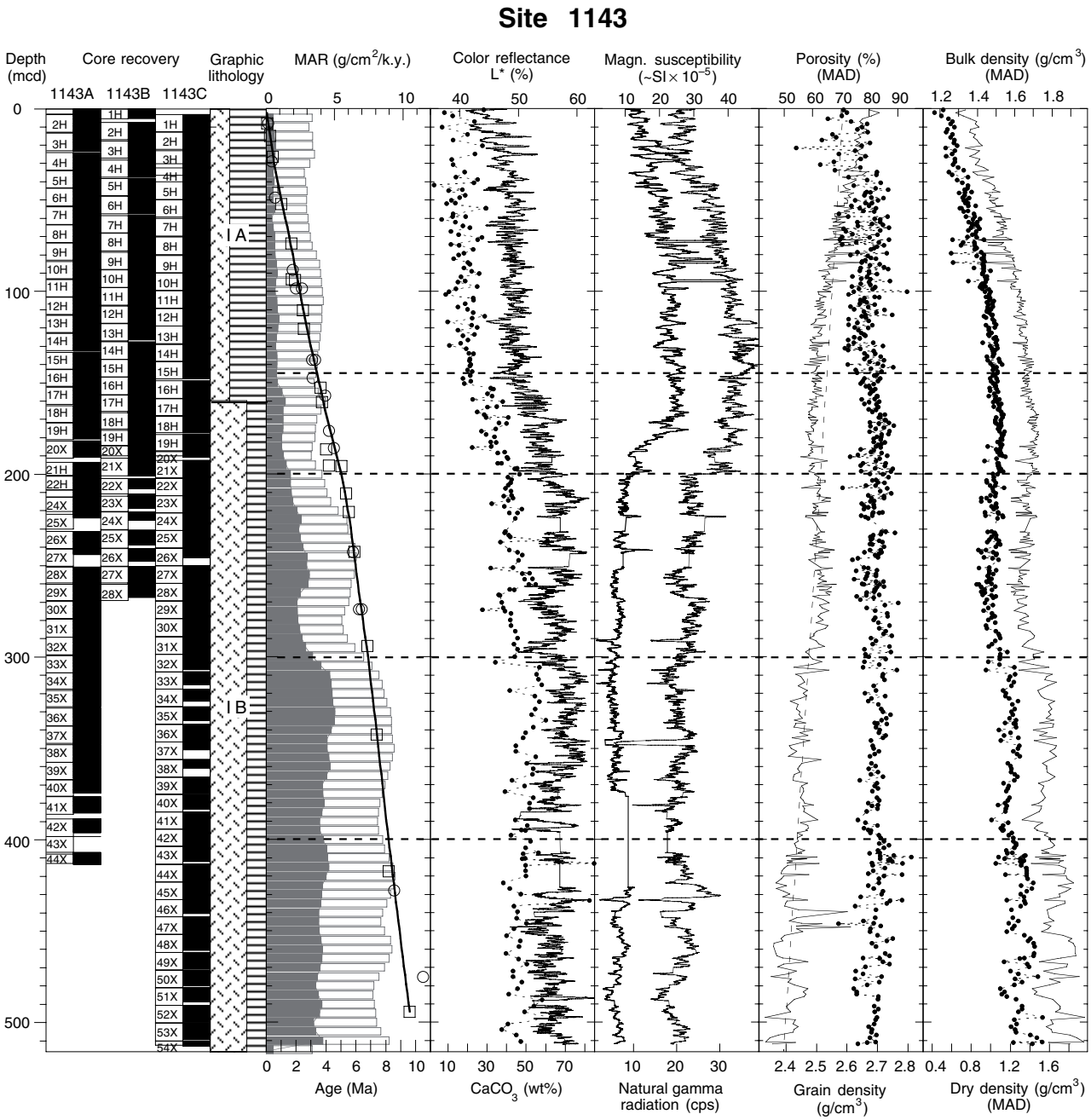

Figure F12. Precruise seismic line across Site 1144. Line SO95-10, CDP 9700 (4:20). Water depth = 2037 m. Penetration depth = 453 mbsf (graphic presentation is approximate). TWT = two-way traveltime.

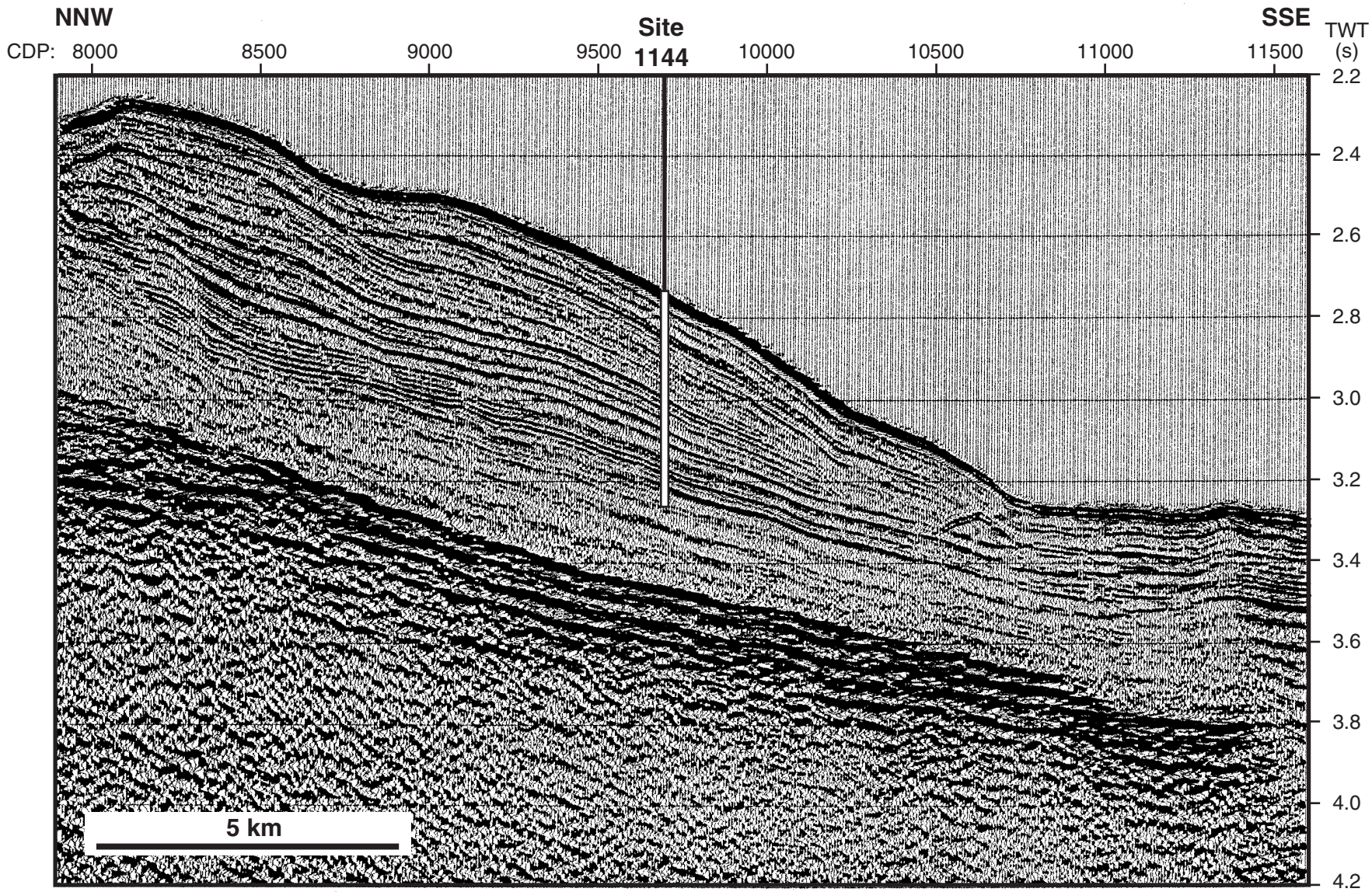

Figure F13. Summary diagram of coring results at Site 1144 on the mcd scale. Maximum penetration measured with the drill pipe is 453 mbsf. See Figure F11, p. 55, for further explanation.

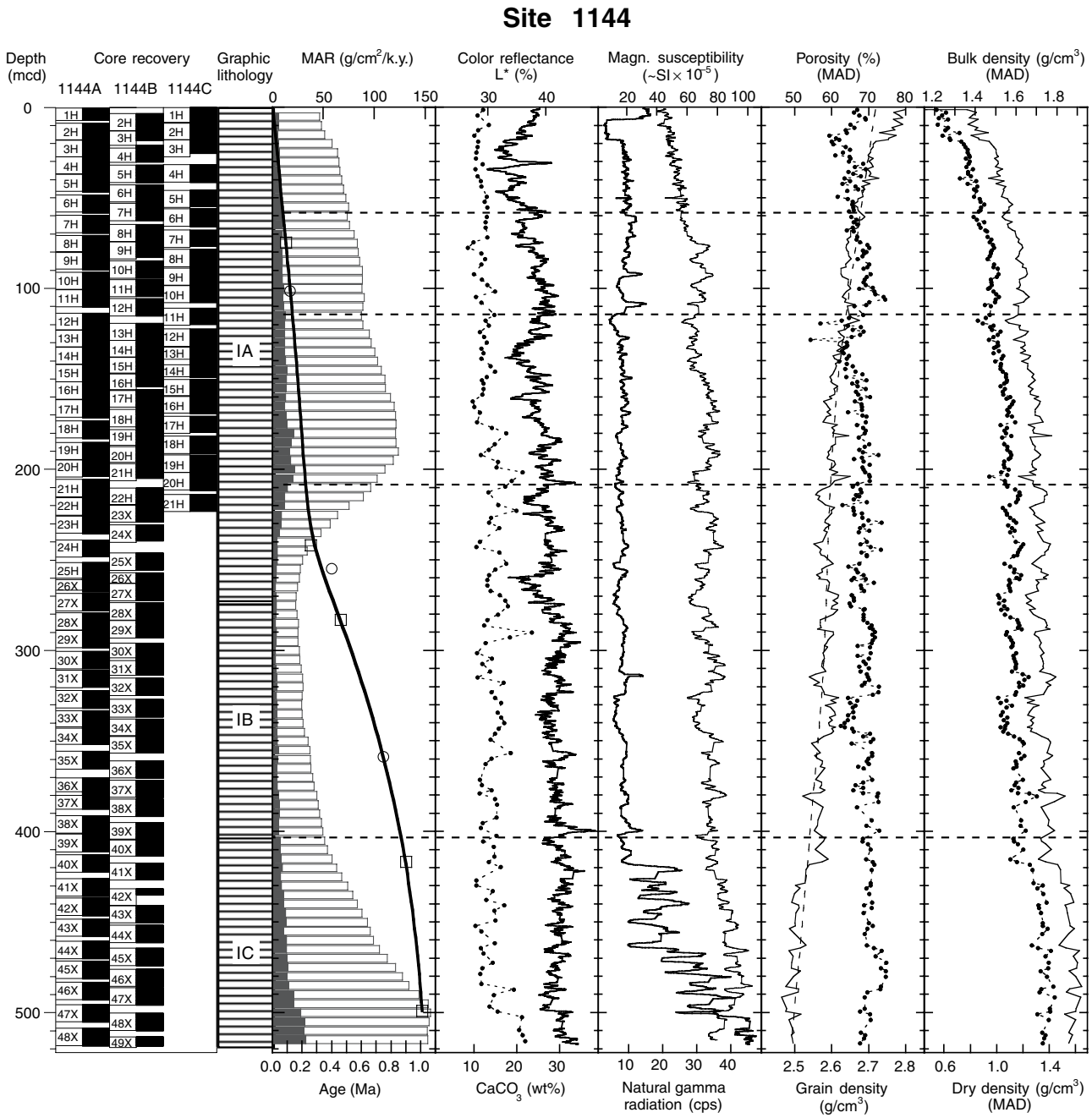

Figure F14. Precruise seismic line across Site 1145. Line SO95-10, CDP 4680 (11:10). Water depth = 3175 m. Penetration depth = 200 mbsf (graphic presentation is approximate). TWT = two-way traveltime.

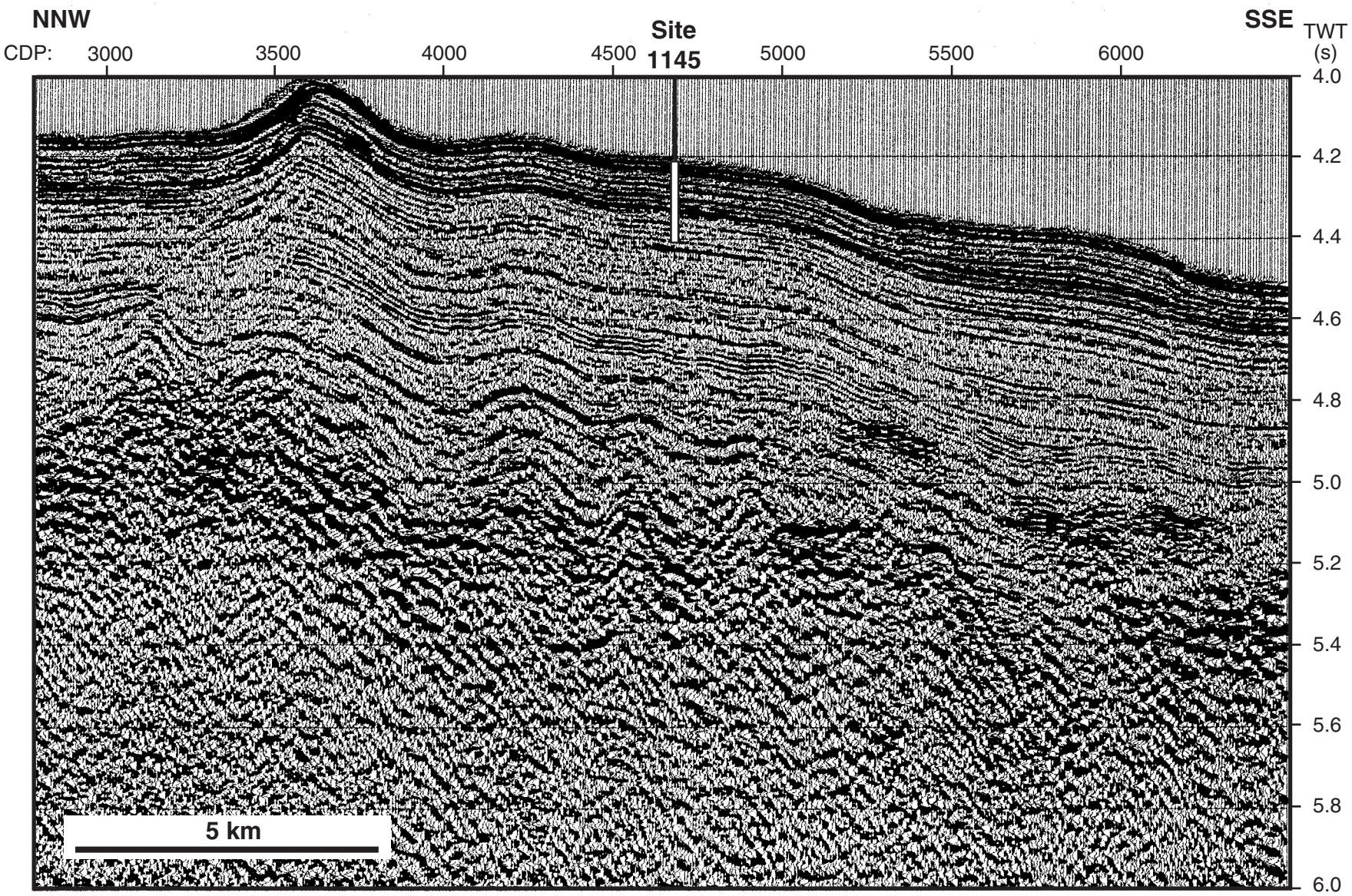

Figure F15. Summary diagram of coring results at Site 1145 on the mcd scale. Maximum penetration measured with the drill pipe is 200 mbsf. See Figure **F11,** p. 55, for further explanation.

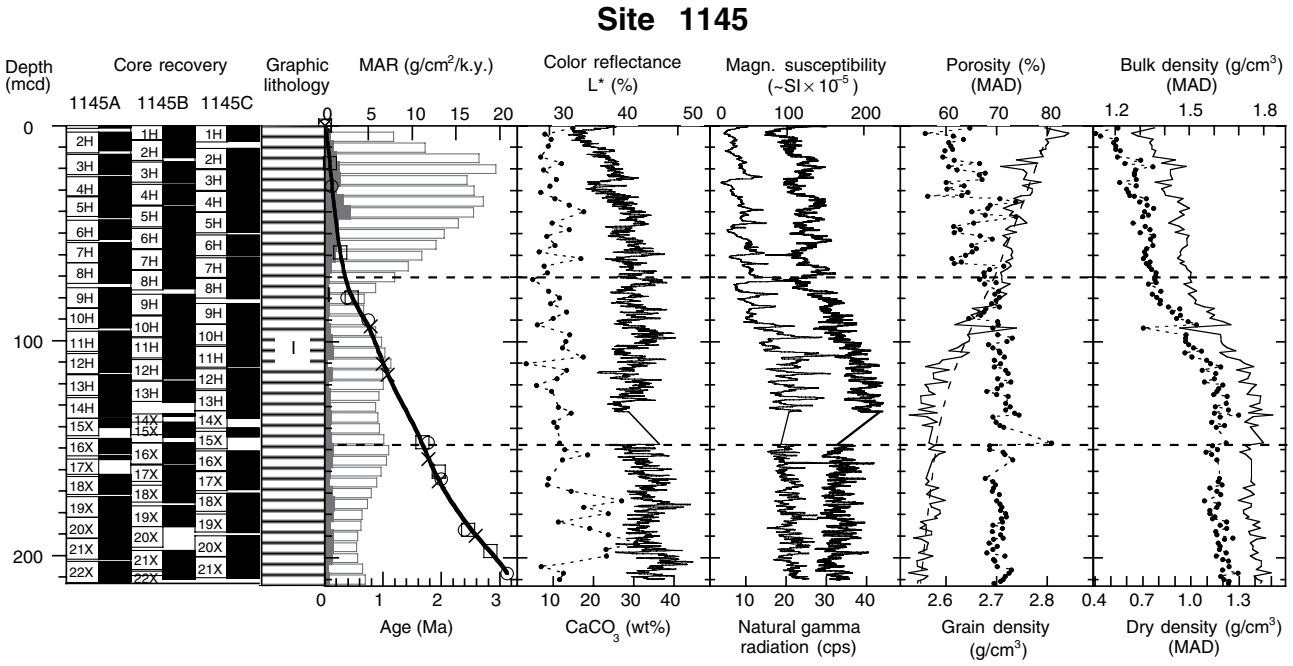

Figure F16. Leg 184 seismic line across Site 1146. Line JR184-3, shotpoint (SP) 3240. Water depth = 2092 m. Penetration depth = 607 mbsf (graphic presentation is approximate). TWT = two-way traveltime.

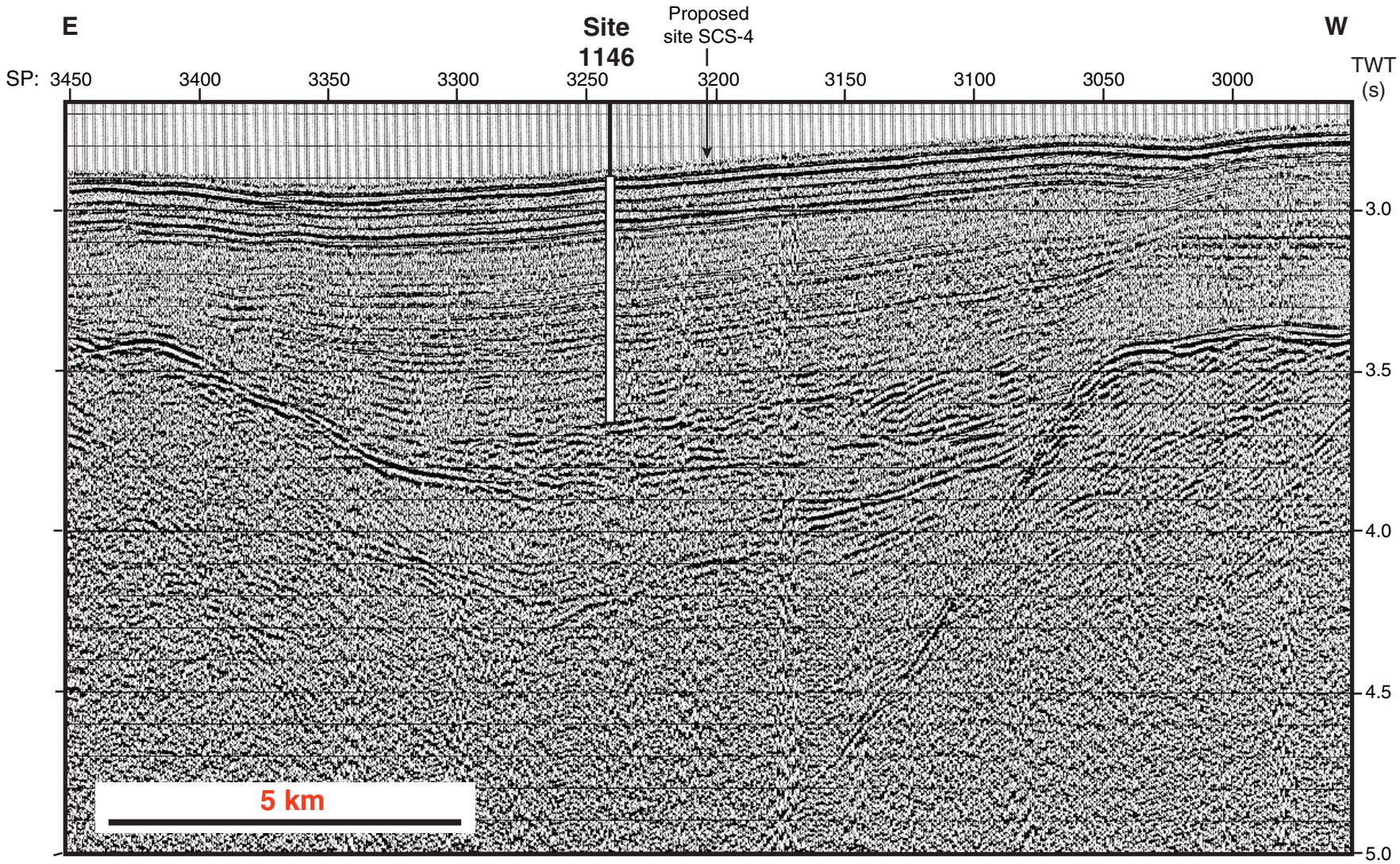

Figure F17. Summary diagram of coring results at Site 1146 on the mcd scale. Maximum penetration measured with the drill pipe is 607 mbsf. See Figure F11, p. 55, for further explanation.

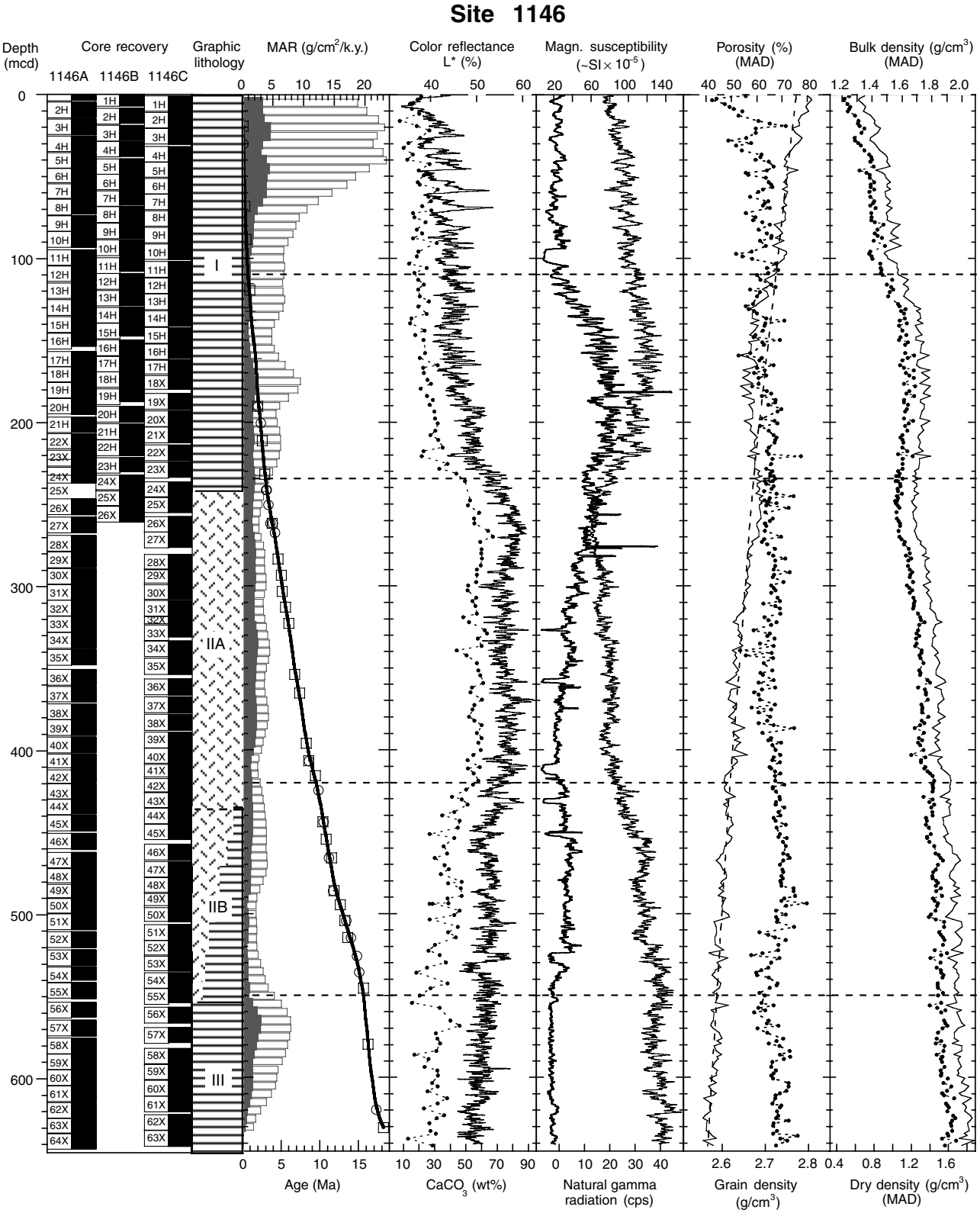

Figure F18. Leg 184 seismic line across Sites 1147 and 1148. Site 1147: Line JR184-1, shotpoint (SP) 1940. Water depth = 3246 m. Penetration depth = 86 mbsf. Site 1148: Line JR184-1, SP 1980. Water depth = 3295 m. Penetration depth = 853 mbsf (graphic presentation is approximate).

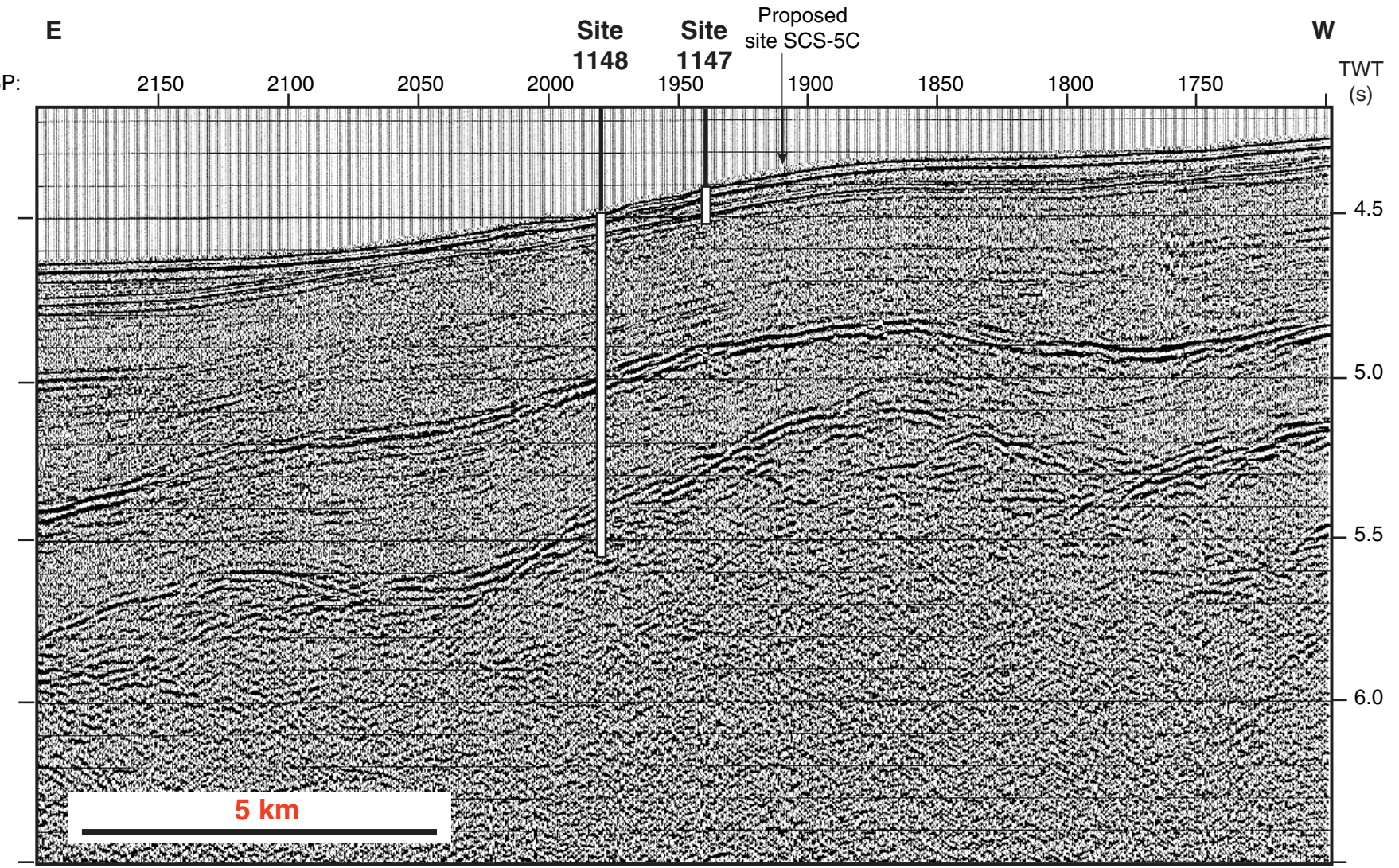

Figure F19. Summary diagram of coring results at Site 1147 on the mcd scale. Maximum penetration measured with the drill pipe is 86 mbsf. See Figure **F11,** p. 55, for further explanation.

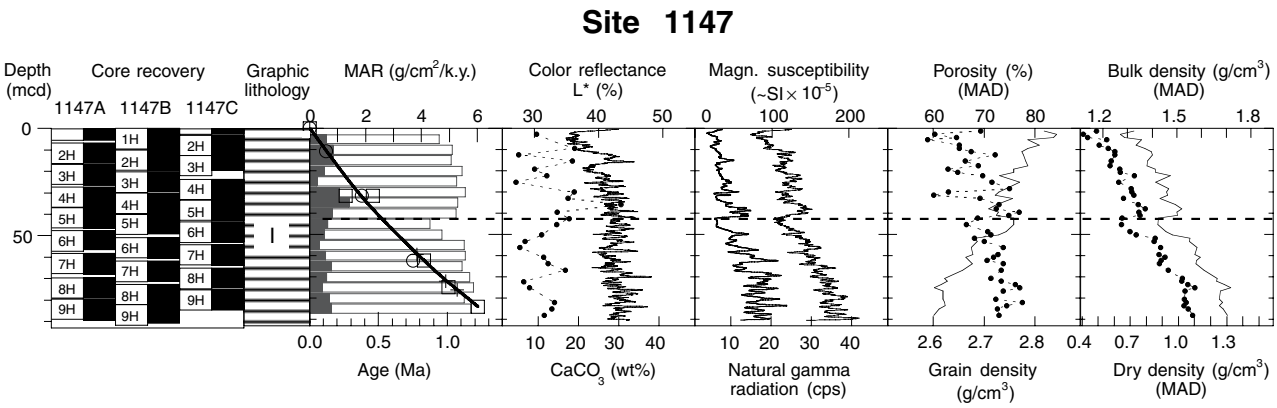

Figure F20. Summary diagram of coring results at Site 1148 on the mcd scale. Maximum penetration measured with the drill pipe is 853 mbsf. See Figure F11, p. 55, for further explanation.

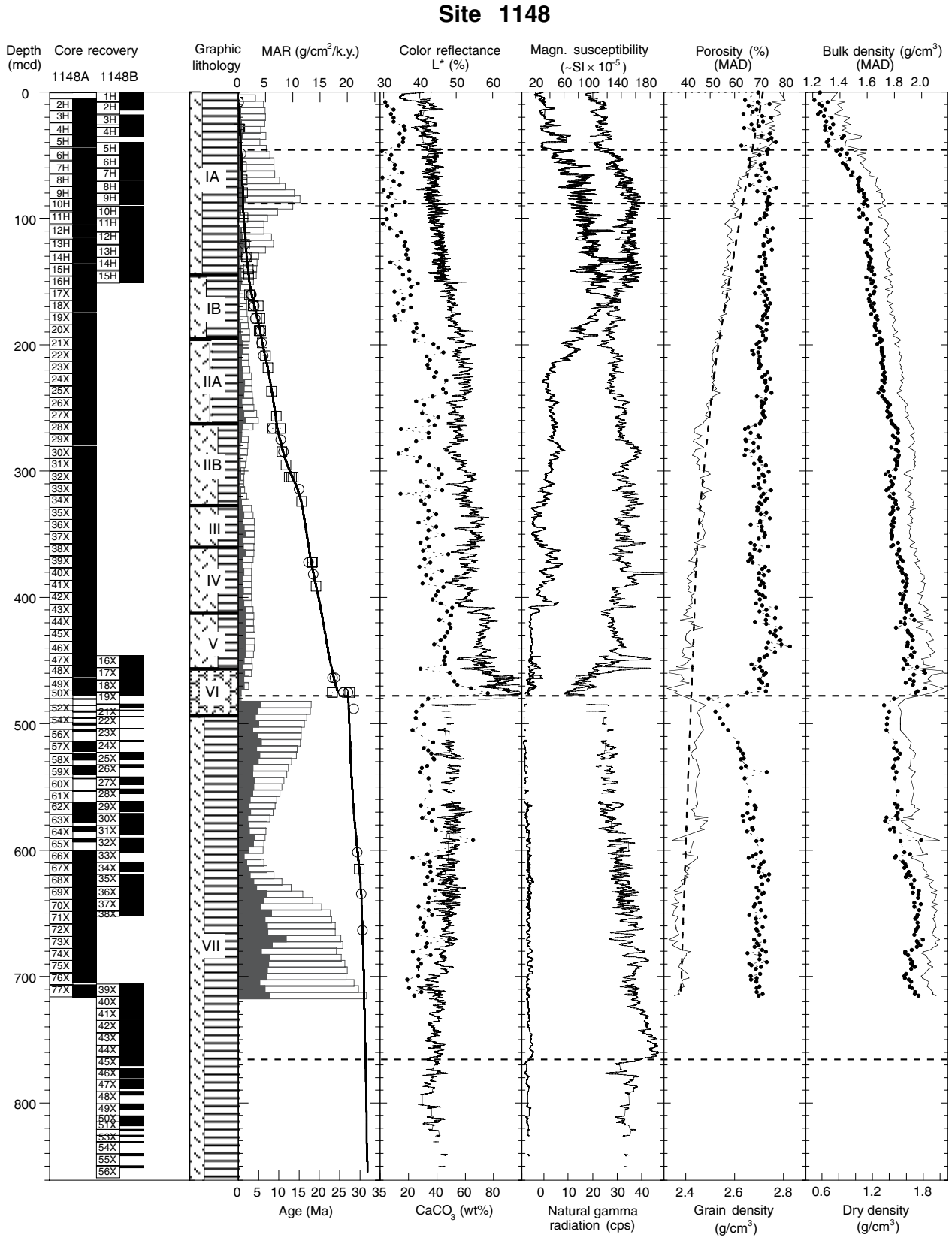

Figure F21. Coring penetration and lithologic units as a function of age in the Leg 184 drilling sites. Horizontal dashed pattern = clay, brick pattern = nannofossil ooze with foraminifers. Gray bands = the occurrence of frequent green clay layers.

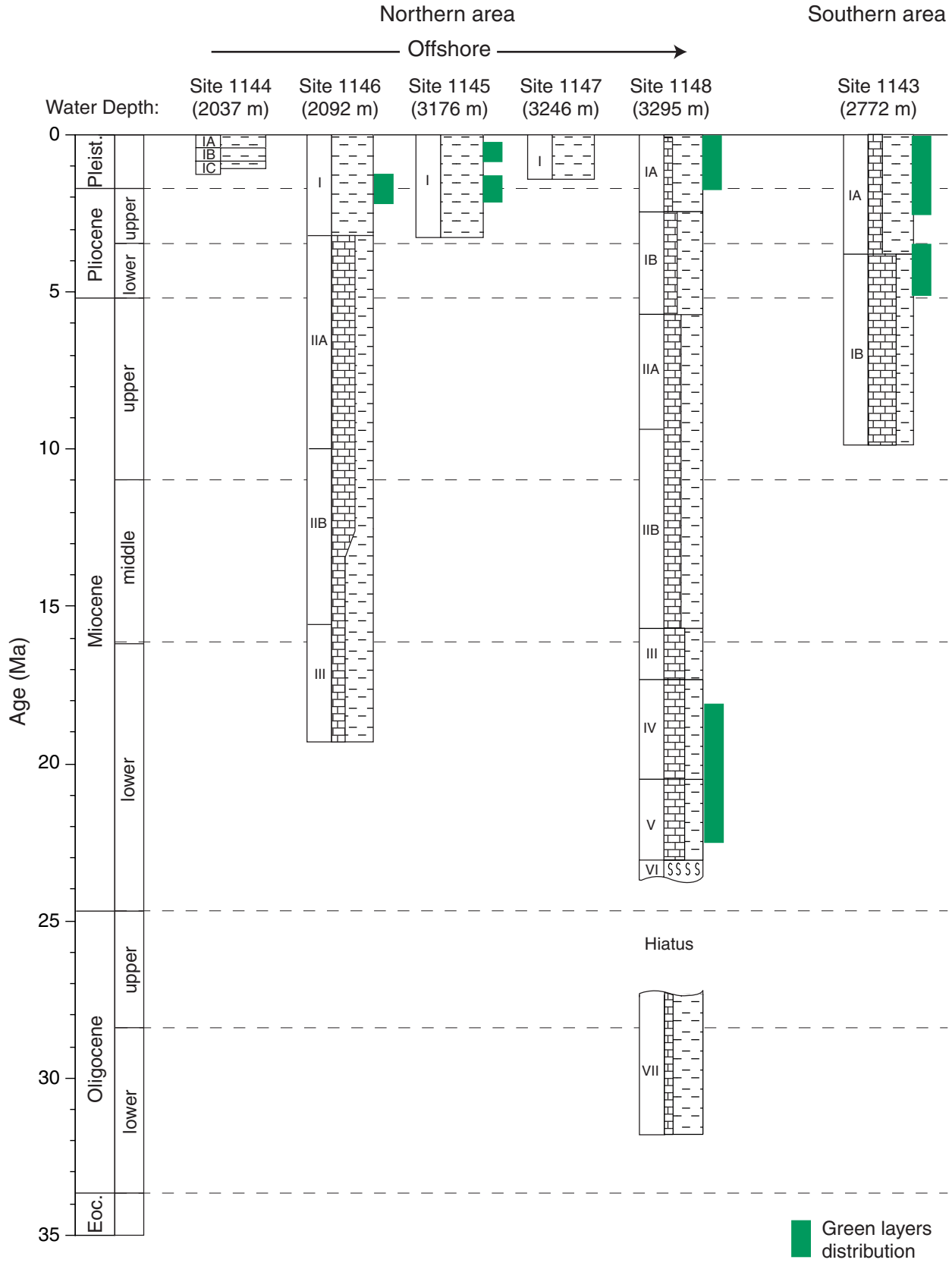

Figure F22. Summary of silica (H_4SiO_4) concentration trends in interstitial water from all Leg 184 sites (except Site 1148), plotted **(A)** vs. meters composite depth (mcd), **(B)** vs. age (Ma), and **(C)** vs. the last 3 m.y. (Ma).

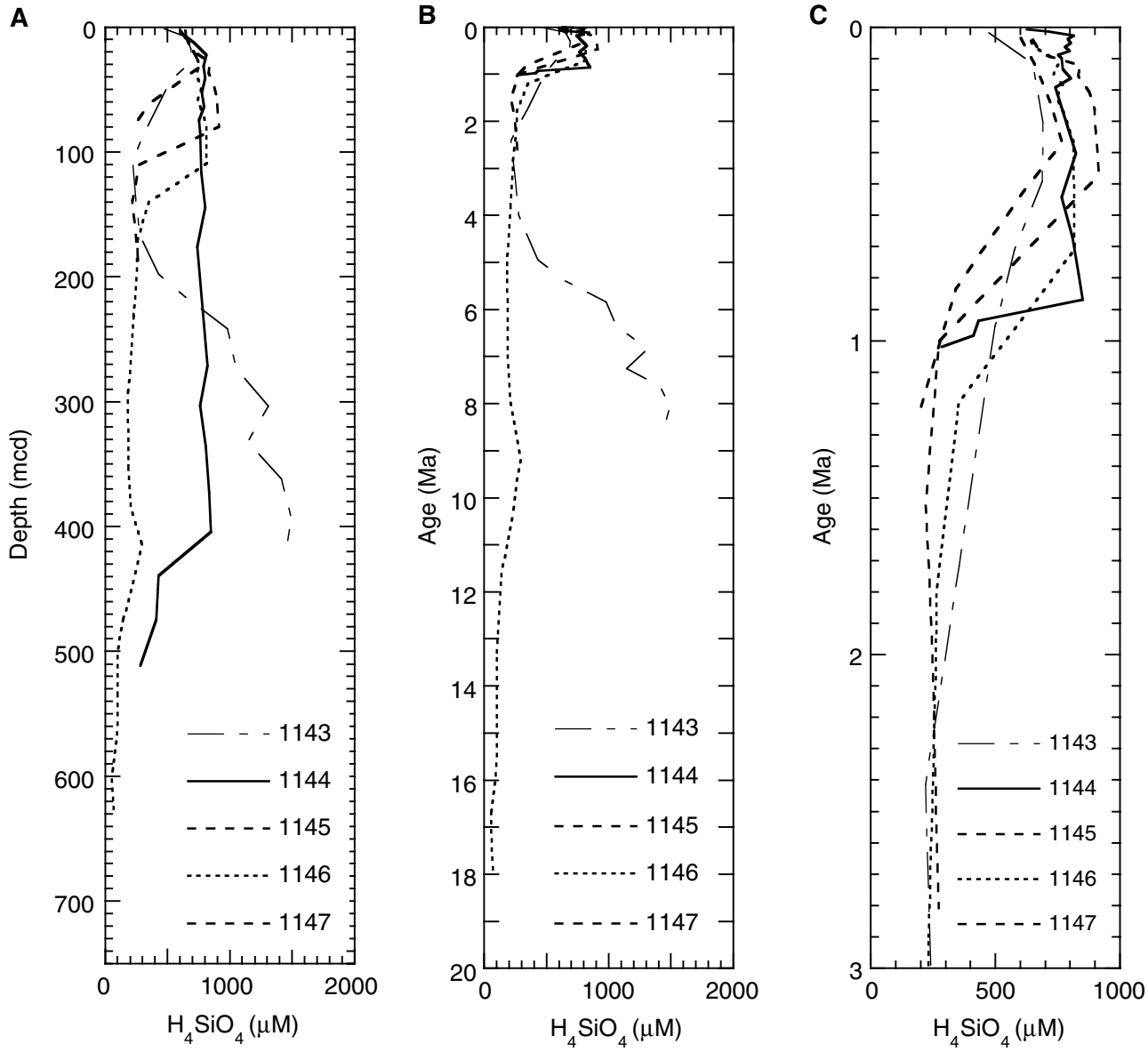

Figure F23. A. Downhole temperature gradients from Leg 184 sites (except Site 1147), presented as linear best fits to 4–5 measurements per site. **B.** Temperature gradients plotted as functions of the water depths for Leg 184 drill sites.

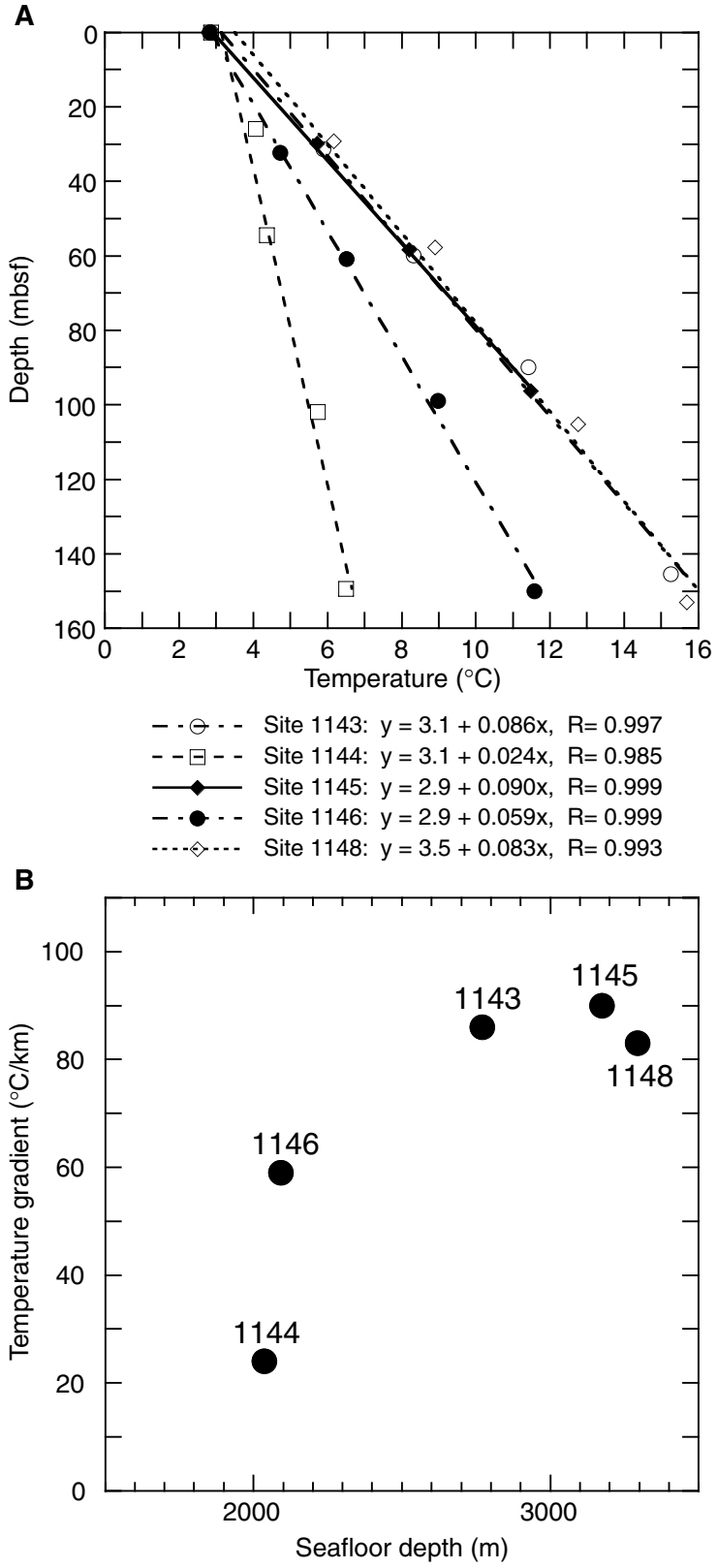

Figure F24. Summary of methane concentrations (headspace method) at the Leg 184 sites that showed significant amounts of gas.

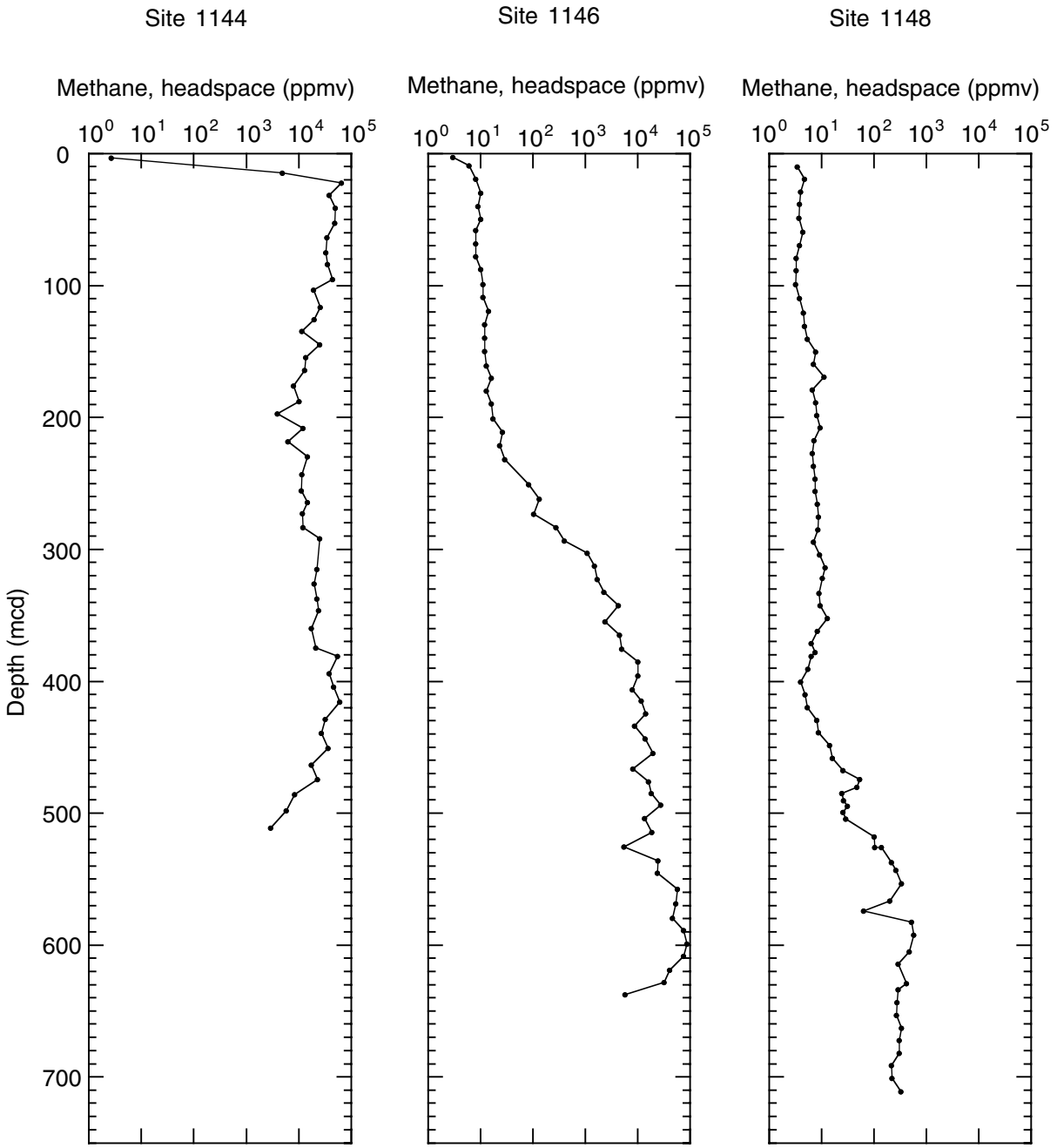

Figure F25. Age-depth relationships for Leg 184 sites. Solid lines = smoothed depth-age models, dots = the actual shipboard age calls from nannofossil and foraminifer biostratigraphy and from paleomagnetism. The thicker line highlights the different trend for the southern South China Sea Site 1143 as compared to the northern sites. The inset presents the past 3 m.y. at a greater resolution than the main diagram.

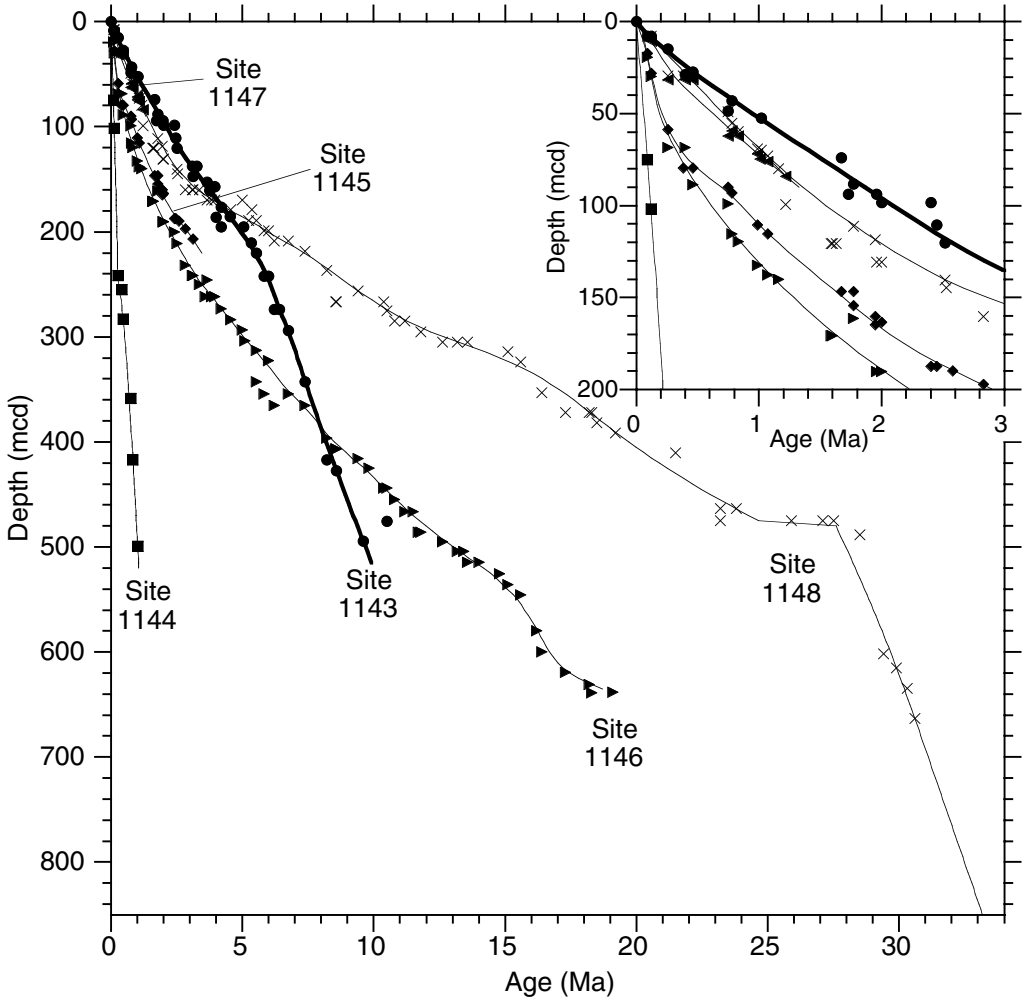

Figure F26. Summary of total (stippled histograms) and carbonate (solid histograms) mass accumulation rates (MARs) vs. age, and linear sedimentation rates (LSRs; solid line). **A.** The three longest records from Leg 184. (Continued on next page.)

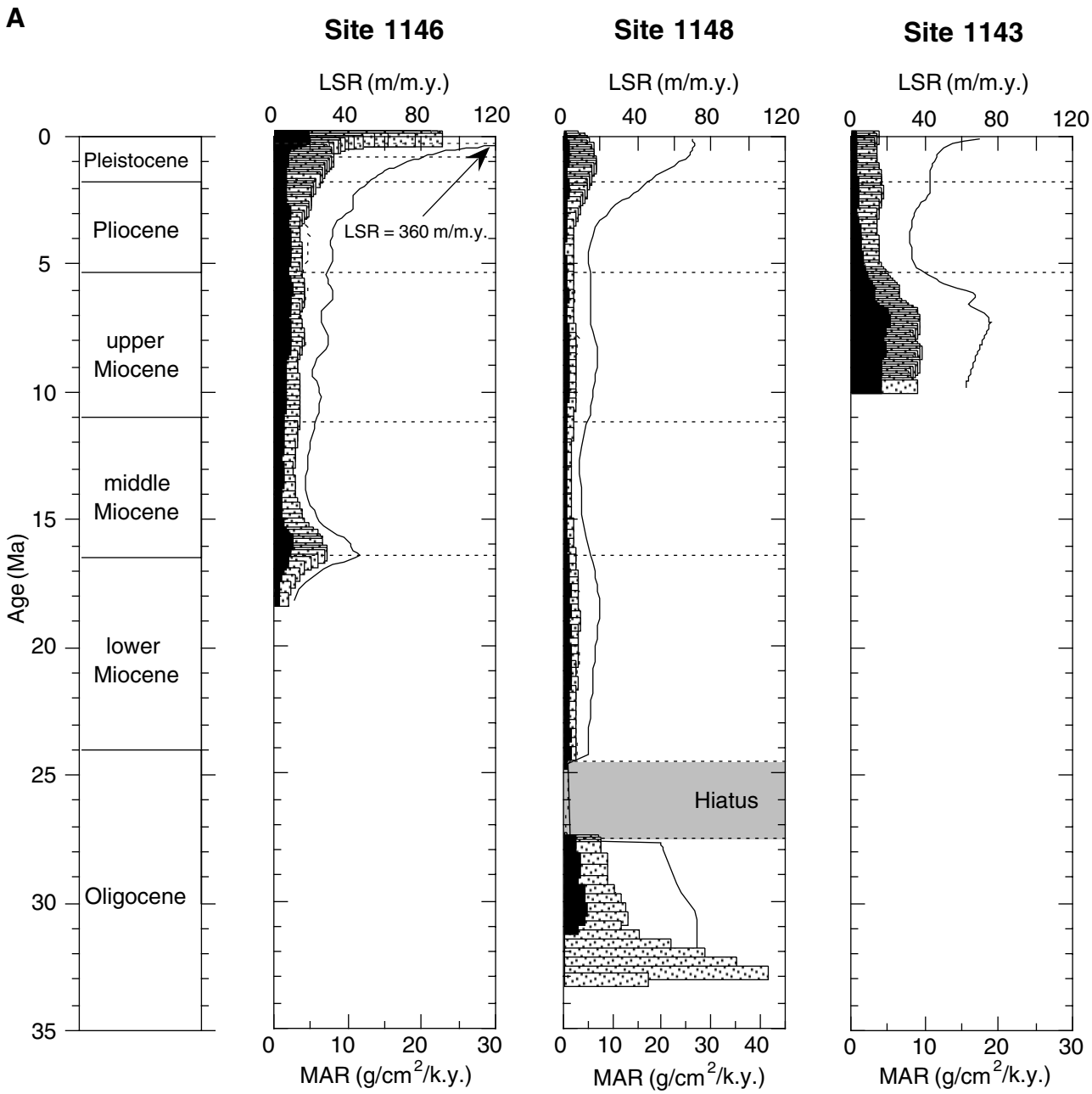

Figure F26 (continued). B. Close-up for the last 3 m.y. for all Leg 184 sites.

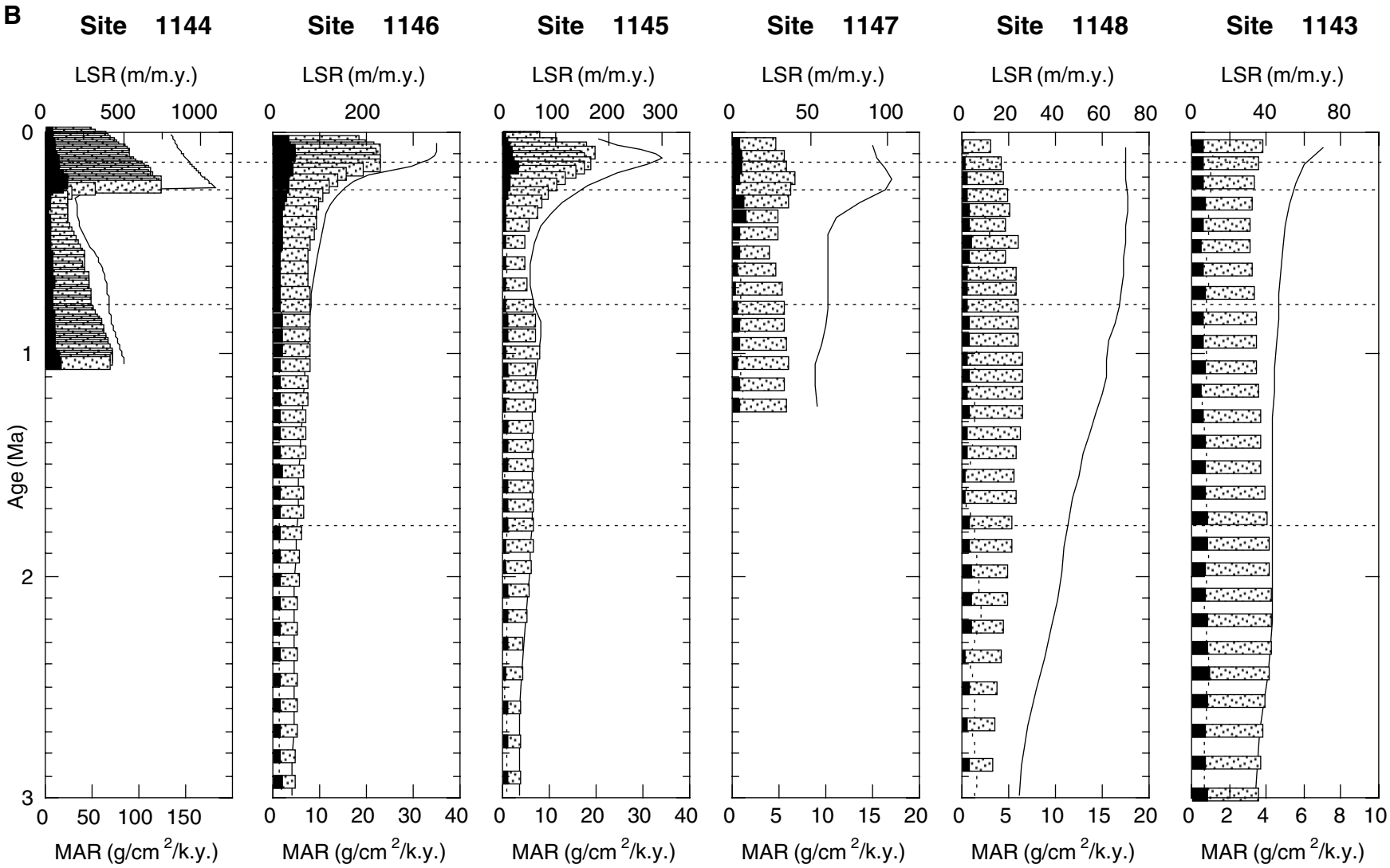

Figure F27. Summary of carbonate concentration vs. age for the three longest records obtained on Leg 184. Note the common pattern of high values in the upper Miocene that decline toward the present.

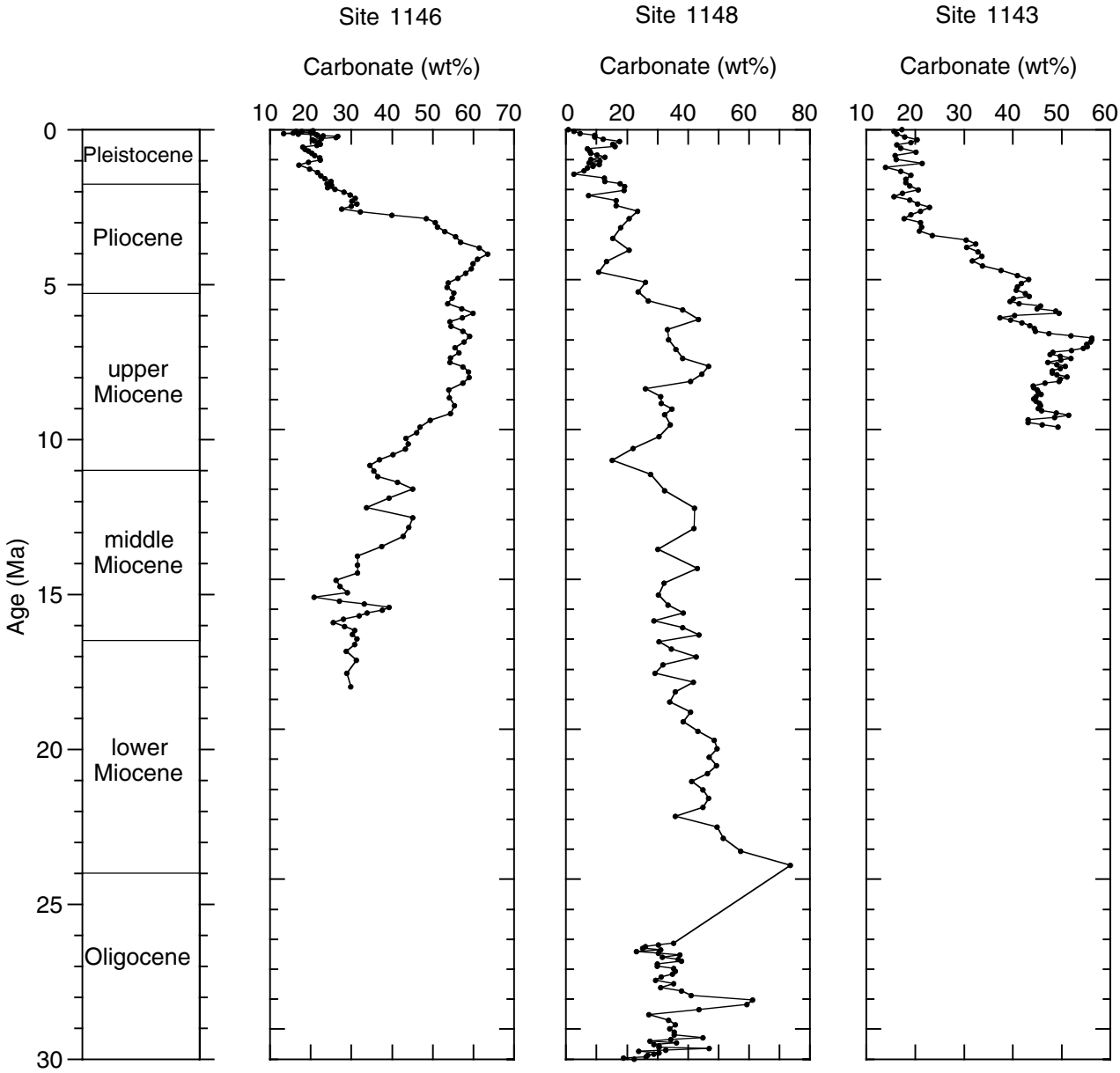

Figure F28. Downhole logs as a function of depth. **A.** Total gamma radiation (American Petroleum Institute [API] units) and *P*-wave velocity. (Continued on next page.)

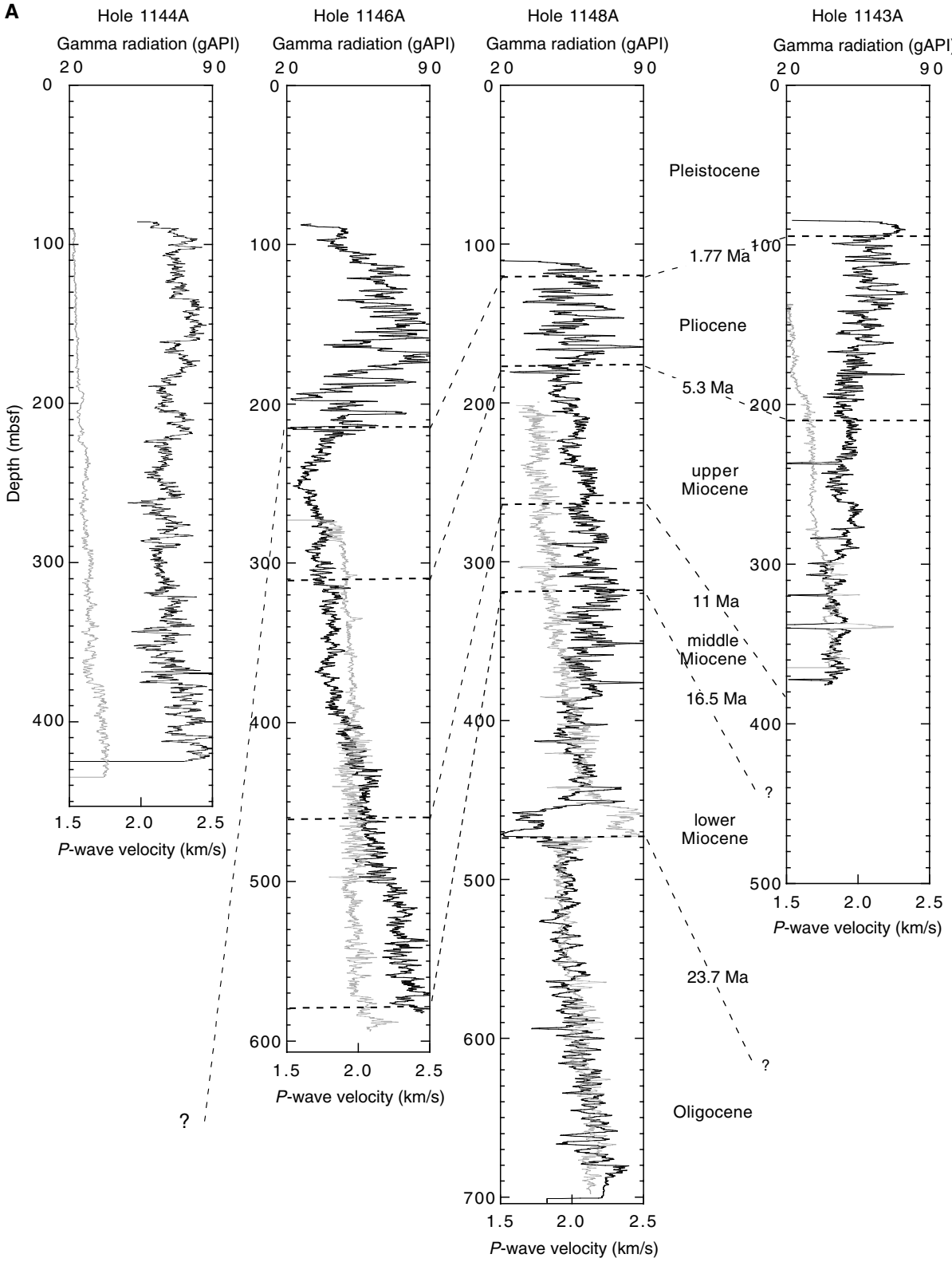

Figure F28 (continued). B. Magnetic susceptibility and photoelectric effect (PEF). Because the sedimentation rates differ greatly between the sites, epoch boundaries are shown to correlate with similar age intervals between the sites. IU = instrument units.

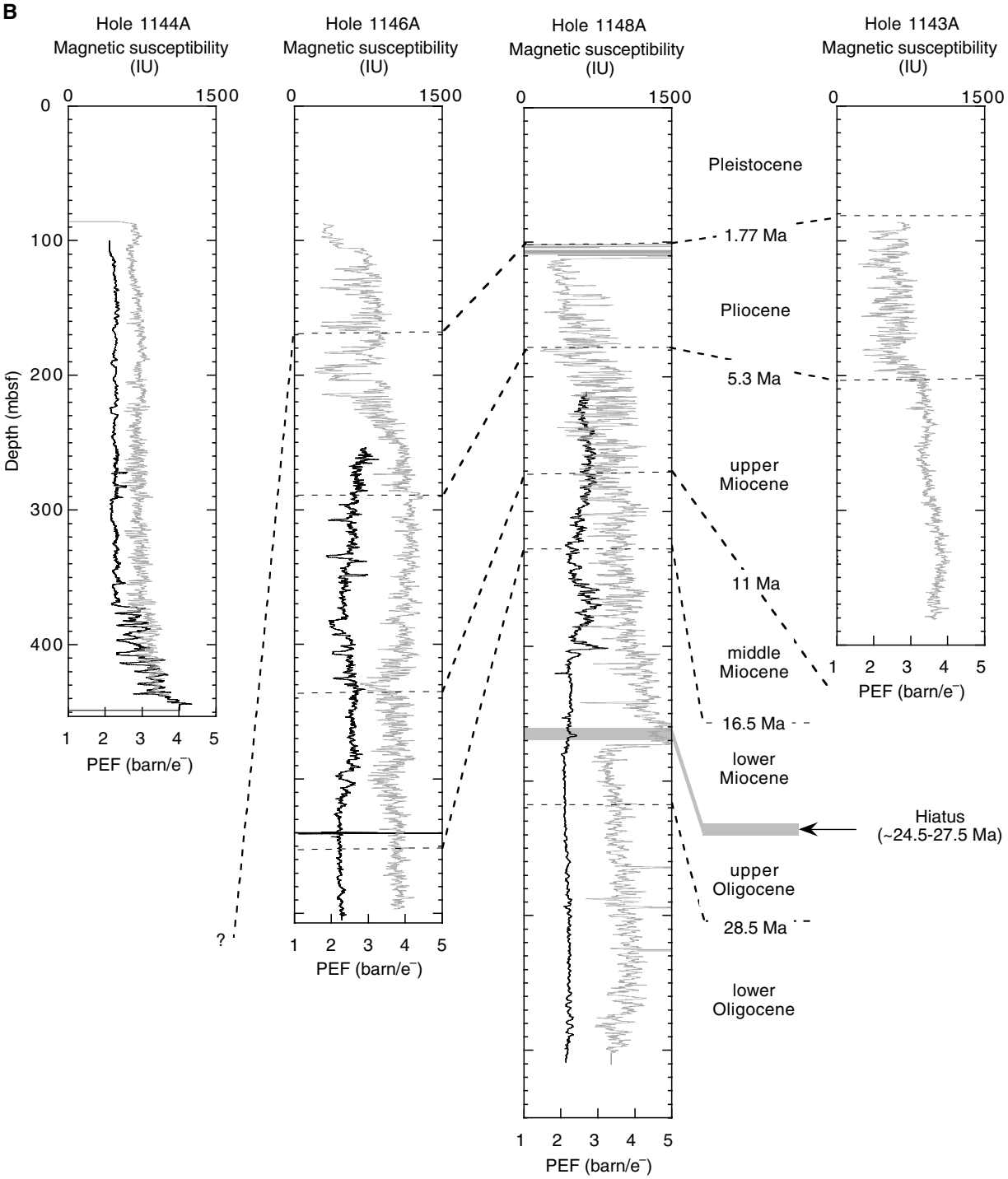

Table T1. Leg 184 operational summary. (Continued on next page.)

Site/Hole	Latitude	Longitude	Water depth (m)	Number of cores	Interval cored (m)	Core recovered (m)	Recovered (%)	Drilled (m)	Maximum penetration (m)
Leave Fremantle									
1143A	9°21.720′N	113°17.102′E	2771	44	400.0	377.88	94.6	0	400.0
1143B	9°21.717′N	113°17.104′E	2773	28	258.2	246.37	95.4	0	258.2
1143C	9°21.713′N	113°17.119′E	2774	54	500.0	477.54	95.5	0	500.0
Site 1143 summary	9°21.72′N	113°17.11′E	2772	126	1158.2	1101.79	95.2	0	1158.2
1144A	20°3.180′N	117°25.133′E	2036	48	452.8	468.88	103.6	0	452.8
1144B	20°3.180′N	117°25.143′E	2039	49	452.0	495.93	98.6	0	452.0
1144C	20°3.182′N	117°25.152′E	2037	21	198.7	198.17	99.7	5	203.7
Site 1144 summary	20°3.18′N	117°25.14′E	2037	118	1103.5	1112.98	100.9	5	1108.5
1145A	19°35.040′N	117°37.868′E	3176	22	200.0	186.14	93.3	0	200.0
1145B	19°35.042′N	117°37.858′E	3174	22	200.0	179.44	89.7	0	200.0
1145C	19°35.039′N	117°37.850′E	3176	21	198.1	189.15	95.5	0	198.1
Site 1145 summary	19°35.04′N	117°37.86′E	3175	65	598.1	554.73	92.8	0	598.1
1146A	19°27.402′N	116°16.363′E	2091	64	607.0	603.85	99.5	0	607.0
1146B	19°27.401′N	116°16.376′E	2092	26	245.1	241.71	98.6	0	245.1
1146C	19°27.403′N	116°16.385′E	2092	63	598.5	606.16	101.4	5	603.5
Site 1146 summary	19°27.40′N	116°16.37′E	2092	153	1450.6	1451.72	100.1	5	1455.6
1147A	18°50.108′N	116°33.271′E	3246	9	81.4	81.70	100.4	0	81.4
1147B	18°50.108′N	116°33.280′E	3245	9	85.5	85.50	100.0	0	85.5
1147C	18°50.109′N	116°33.280′E	3245	9	78.6	76.60	97.5	0	78.6
Site 1147 summary	18°50.11′N	116°33.28′E	3246	27	245.5	243.84	99.3	0	245.5
1148A	18°50.167′N	116°33.932′E	3297	77	704.0	632.10	89.8	0	704.0
1148B	18°50.170′N	116°33.946′E	3292	56	500.6	364.40	72.8	352.6	853.2
Site 1148 summary	18°50.17′N	116°33.94′E	3294	133	1204.6	996.50	82.7	352.6	1557.2
Arrival in Hong Kong									
Leg 184 totals:				622	5760.5	5461.56	Mean: 94.8	362.6	853.2

Table T1 (continued).

Site/Hole	Local arrival (1999)	Local departure (1999)	Time on hole (hr)	Time on hole (days)	Transit (days)	Number of APC cores	Number of XCB cores	Seafloor (mbrf)	Rig floor elevation (m)	Maximum penetration (mbrf)
Leave Fremantle		19 Feb 1730								
					11.94					
1143A	3 March 1600	6 March 2345	79.75	3.32		21	23	2782.0	11.0	3182.0
1143B	6 March 2345	8 March 0010	24.42	1.02		19	9	2783.5	11.0	3041.7
1143C	8 March 0010	10 March 0545	53.58	2.23		19	35	2784.5	11.0	3284.5
Site 1143 summary			157.75	6.57		59	67	2783.3	11.0	3169.4
					3.50					
1144A	13 March 1745	16 March 0655	61.17	2.55		25	23	2047.0	11.3	2499.8
1144B	16 March 0655	17 March 2115	38.33	1.60		22	27	2049.8	11.3	2501.8
1144C	17 March 2115	18 March 1645	19.50	0.81		21	8	2048.2	11.3	2251.9
Site 1144 summary			119.00	4.96		68	58	2048.3	11.3	2417.8
					0.13					
1145A	18 March 1945	20 March 0030	28.75	1.20		14	9	3187.1	11.5	3387.1
1145B	20 March 0030	20 March 1900	18.50	0.77		13	0	3185.9	11.5	3385.9
1145C	20 March 1900	21 March 1645	21.75	0.91		13	8	3187.9	11.5	3386.0
Site 1145 summary			69.00	2.88		40	17	3187.0	11.5	3386.3
					0.29					
1146A	21 March 2345	25 March 1350	86.08	3.59		21	43	2102.6	11.5	2709.6
1146B	25 March 1350	26 March 1415	24.42	1.02		23	3	2103.2	11.5	2348.3
1146C	26 March 1415	29 March 0615	64.00	2.67		17	46	2103.0	11.5	2706.7
Site 1146 summary			174.50	7.27		61	92	2102.9	11.5	2588.2
					0.18					
1147A	29 March 1030	30 March 0200	15.50	0.65		9	0	3257.5	11.6	3338.9
1147B	30 March 0200	30 March 1000	8.00	0.33		9	0	3257.0	11.6	3342.5
1147C	30 March 1000	30 March 1915	9.25	0.39		9	0	3256.9	11.6	3335.5
Site 1147 summary			32.75	1.36		27	0	3257.1	11.6	3339.0
					0.04					
1148A	30 March 2015	4 April 1600	115.75	4.82		16	61	3308.7	11.6	4012.7
1148B	4 April 1600	10 April 2215	150.25	6.26		15	41	3303.4	11.6	4156.6
Site 1148 summary			266.00	11.08		31	102	3306.0	11.6	4084.7
Arrival in Hong Kong	12 April 0830				1.43					
Leg 184 totals:			819.00	34.13	17.50	286	336	2749.9	Mean: 11.4	4156.6